Doctoral Dissertation

# Intense Terahertz Electromagnetic Source Using Laser-Plasma Interaction

Junghun Shin

April 2014

Graduate School of Engineering,
Osaka University

# Acknowledgement

I am grateful to everyone who provided assistance in various stages throughout this research.

First and foremost, I would like to express my deep and sincere gratitude to my supervisor, Professor Ryosuke Kodama at the Division of Electrical, Electronic and Information Engineering, Graduate School of Engineering, Osaka University (OU), Osaka, Japan for his continuous encouragements and financial supports. His wide knowledge and logical way of thinking have been great value for me. During my time in his laboratory of high energy density engineering, aka Kodama lab, I benefited from a wealth of opportunities and experiences.

I am indebted to Professors Kazuo A. Tanaka, Yoshio Ueda, Toshiyuki Iida at the Division of Electrical, Electronic and Information Engineering, Graduate School of Engineering, Osaka University, and Professors Mitsuo Nakai, Masakatsu Murakami and Hiroshi Azechi at the Institute of Laser Engineering (ILE), Osaka University.

Much thanks go to Assistant Professor Jin Zhan at Photon Pioneers Center, Graduate School of Engineering, Osaka University (PPC). He helped me develop the laboratory skills that would be used throughout my career with patient guidance.

My much appreciation goes to Professor Alexei Zhidkov (PPC). In addition to generously offering his particle-in-cell code, he has guided me with his endless patience, particularly on simulation works in this dissertation, with his deep understanding of physics in a broad area encompassing plasma physics, computational physics, nonlinear optics, and etc.

I thank Associate professor Tomonao Hosokai for his generous and helpful suggestions and financial support.

I would also like to thank Professor Noboru Yugami at Utsunomiya University for the useful discussions he had shared with the terahertz group in Kodama lab almost every month.

I am also grateful to Associate Professors Norimasa Ozaki (OU), Youichi Sakawa (ILE), Dr. Yoshitaka Mori (formerly OU, currently with the Graduate

School for the Creation of New Photonic Industries, Hamamatsu, Japan), Dr. Yuichi Inubushi (formerly OU, currently with RIKEN SPring-8 Center, Hyogo, Japan), Dr. Shinichi Masuda, Dr. Matsuoka Takeshi, Dr. Nobuhiko Nakanii, and Dr. Naveen Pathak (PPC) for useful discussions they kindly shared with me.

I also thank for past and present members of the Kodama group for their academic advice, practical supports and the fun times, especially Dr. Motoaki Nakatsutsumi, Dr. Hirotaka Nakamura, Dr. Kazunori Shibata, Dr. Akinori Nishida, Dr. Yoshio Mizuta, Dr. Tomoaki Kimura, Dr. Akira Kon, Dr. Kohei Miyanishi, Dr. Yuichiro Monden, Tomohiro Nakazawa, Makoto Nakagawa, Masahiro Kimura, Atsushi Wada, Yuji Nosaka, Keigo Makito, Tianju Zhang, and Tian Chao (Tsinghua University, China), Toshihiro Tanaka, Keigo Higashi, Takuya Michibata, Takashi Endo, Yudai Yoneoka, Syunsuke Morimoto, Tatsuya Jitsui, Hitoshi Ieuji, Taisuke Kumagai, Satoshi Soda, Shohei Kajino, Naoya Yokoyama, Hiroyuki Uranishi, Yuto Asaumi, Kazuki Nakatsuka, Tomohiro Kohara, Yoshihiko Kondo, Hiroki Nakahara, Keisuke Hayashi, Tsung-Han Yang, Mika Kita, Shotaro Iketani, Keita Iwasa, Tsuyoshi Ogawa, Yuya Sato, Isamu Jinno, Naoki Takeguchi, Toshiki Mushiake.

I also thank Yasuko Kimura for her technical support on fabrication of solid targets.

Special thanks go to the support of the computer room of ILE, especially Professor Hideo Nagatomo and Dr. Yuko Fukuda, Usami Masako, Marika Taniguchi, and the cybermedia center at Osaka University.

My thanks would not be complete if I did not mention Terumi Monno, Mami Kurisu, and Kumiko Mori (PPC) for their excellent administrative assistance. I would also like to thank Aiko Suda who provided administrative assistance for my activities supported by *ASian core program for High energy density science Using intense LAser photons* (ASHULA) program of Japan Society for the Promotion of Science (JSPS).

This dissertation concludes my ten years of stay in Japan, which had been initially supported by the *Japan-Korea Joint Government Scholarship Program for the Students in Science and Engineering Departments*. I express my deep gratitude to everyone who involved with the program, especially, Professors Norio Furushiro and Takako Muraoka.

Last, but not least, I thank my family, Booho Shin (申富浩), Heesoon Kim (金喜順), and Hyangsoo Shin (申香秀), for all their patience and support.

# Abstract


This dissertation describes numerical simulations, theoretical models, and experiments regarding generation of intense terahertz (THz) wave using laser-plasma interaction for development of terawatt (TW) THz radiation source, which has a strong demand for new studies and applications in a broad range of science and engineering research areas, especially high energy density physics (HEDP).

This dissertation comprised of five main chapters. In Chp. 1, conventional THz sources and those based on laser-plasma interaction is compared, and the possibility of the latter for an intense THz source is shown. Some of the missing gaps in the previous studies are listed, for which works in subsequent chapters tried to address.

In Chp. 2, THz generation models that are widely accepted in the research community is reviewed. In addition, a new model, called beat-wave model, for THz radiation is proposed that takes into account the formation of ionization front by intense incident laser pulse and the frequency upshift of it induced by the plasma. Those phenomena play important roles for THz generation as shown in Chp. 3, but have not been included in conventional models.

In Chp. 3, two-color laser scheme, the most effective method currently found in the literature, is studied by numerical method, namely, the particle-in-cell method, to reveal the dependence of characteristics of THz radiation, such as power and angular distribution, on pump laser intensity is studied by numerical method, namely, particle-in-cell simulation. It is the first study that examines the THz radiation numerically with the pump laser intensity over $10^{15}$ W/cm$^2$. The peak THz frequency predicted by the new beat-wave model showed a good match with the spectrum obtained in the simulation, partly validating the new model.

In Chp. 4, experiments performed to prove the amplification of THz radiation by laser-produced plasma is described. Using a diffraction method for low-density plasma diagnosis, the correlation between the plasma density profile and THz power is found for the first time. One order of increase in the THz power is observed when the plasma density profile on the laser propagation

axis is asymmetric. A model that takes into account amplification showed better match with the experiment results than the one that ignores amplification, suggesting the amplification of THz radiation by plasma.

In Chp. 5, waveguiding of THz wave by laser-produced plasma waveguide is studied for the first time with particle-in-cell simulation. With the plasma waveguide, the bandwidth is reduced to $\sim$ 20 THz from broadband generation, and the THz intensity increases by more than two orders compared to the case without the waveguide. It is found that, one TW THz source may be realized using a compact, ten TW femtosecond laser system.

The research achievements, specifically, new theoretical model, experimental indication of THz amplification, and demonstration of plasma waveguide, offer new insights and open the possibility for the development of compact TW THz electromagnetic source, expediting new researches and engineering applications in HEDP.

# 研究概要

本論文は，テラワット級のテラヘルツ光源の開発に向け，レーザー・プラズマ相互作用を用いた高強度テラヘルツ電磁波の発生に関して行った理論モデルの開発及びシミュレーションと実験の成果をまとめたものである．テラワット級のテラヘルツ光源の実現は，高エネルギー密度物理（high energy density physics, *HEDP*）をはじめとした理工学分野において幅広い応用が期待されている．

本論文は以下の五章で構成されている．第一章である序論では，既存のテラヘルツ光源とレーザープラズマ相互作用を用いた光源を比較し，高強度テラヘルツ光源としての後者の可能性を示した．また従来の研究における限界を指摘し，本論文でまとめた研究内容を明確に示した．

第二章では，既存のレーザー・プラズマ相互作用を用いたテラヘルツ発生モデルについて概説した．また，テラヘルツ光源の高強度を図るうえで必須になるが，従来のモデルでは考慮されていなかった，レーザーパルスによるイオン化フロントの生成と入射レーザーの周波数上昇を取り入れたビート波モデルを提案した．

第三章では，先行研究のなかで，入射レーザー光からテラヘルツ光へのエネルギー変換効率が最も高い方法である二色レーザー生成プラズマによるテラヘルツ電磁波生成を対象に，これまで研究がなされていなかった高いレーザー強度（$> 10^{15}\,\mathrm{W/cm^2}$）における，テラヘルツ電磁波放射の諸特性（放射角度分布，パワー）の入射レーザー強度への依存性を，二次元の粒子シミュレーションを用いて調べた．また，本研究で提案したビート波モデルで予測されるテラヘルツ電磁波のピーク周波数と数値実験で観測されたスペクトルを比較し，新しいモデルの妥当性を根拠づけた．

第四章では，レーザー生成プラズマによるテラヘルツ電磁波の増幅作用に関して行われた実験について述べた．レーザー伝搬軸上で非対称的なプラズマ密度分布が作られたことにより，テラヘルツ電磁波のパワーが一桁増加する現象が観測された．同結果は，増幅作用を取り入れたテラヘルツ生成モデルと比較され，レーザー生成プラズマによるテラヘルツ電磁波の増幅作用を示唆するものであると考えられる．また，テラヘルツ電磁波のパワー計測と同時に低密度プラズマの診断も行い，プラズマのレーザー伝搬軸上での密度分布とテラヘルツ電磁波のパワーを相関づけることに初めて成功した．

第五章では，レーザー生成プラズマをテラヘルツ電磁波の導波路として応用することを初めて粒子シミュレーションについて述べた．プラズマ導波路を用いることによって，テラヘルツ光の周波数帯域を20 THzまで狭帯域にするとともに，その強度を導波路なしの場合と比べ，二桁ほど増加させることに成功し，テラワット級のテラヘルツ電磁波発生が10テラワット級のフェムト秒レーザーを用いて実現できる可能性を示した．

本研究の研究成果は，新しい理論モデル，増幅及び導波路といった新機構によるテラヘルツ電磁波源の高強度化に関して新規の知見を与えるものであり，HEDP領域での新たな研究や応用開発を促進するものであると考えられる．

# Contents

# List of Figures

# List of Tables

# Chapter 1

# Introduction

This dissertation compiles my efforts to fill the gaps in theoretical, numerical, and experimental studies on the generation of intense terahertz (THz) radiation using laser-plasma interaction. There is a strong demand and necessity for an intense THz electromagnetic wave source, because its realization allows great new opportunities in a wide range of scientific research areas, especially in high energy density physics (HEDP), including ion acceleration and studies on warm dense matter [1].

For example, a numerical study with particle-in-cell simulations shows that a terawatt (0.3 GV/cm) THz pulse with its duration of 1.5 ps incident upon 300 mm-long, fully ionized hydrogen plasma can selectively accelerate ions more than MeV, while keeping electrons cool under 10 keV as shown in Fig. 1.1 [2].

The advantage of the low-frequency light (or long wavelength light) such

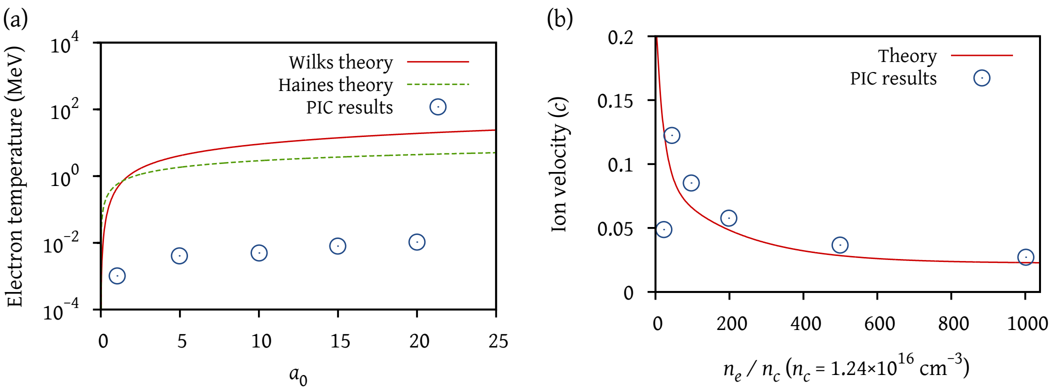


Figure 1.1: Selective ion acceleration by intense THz pulse. (a) Electron temperature against the normalized potential of THz intensity. (b) Ion velocity against the electron density.

as THz wave is clear since the normalized vector potential $a_0$ of electric field $E$, on which the relativistic factor $\gamma = \sqrt{1 + a_0^2}$ depend, is given by

$$a_0 = eE/m_0\omega c \tag{1.1}$$
$$= 8.5 \times 10^{-10} \lambda\,[\mu\mathrm{m}]\, I^{1/2}\,[\mathrm{W/cm^2}]\,, \tag{1.2}$$

where $e$ the elementary charge, $m$ the electron mass, and $\omega$ the laser frequency, $\lambda$ the wavelength, $I$ the focused intensity. The normalized vector potential is proportional to the wavelength.

Figure 1.2 shows the current state of THz source in terms of its THz electric field against the incident laser pulse energy. One of the strongest THz source is obtained using non-linear interaction of laser light with plasma. Plasma-based sources utilize the ionization of target as an essential process for THz generation. Contrarily, THz yield by sources using solid nonlinear crystals is limited by the damage threshold on incident laser intensity. For example, <100>-GaAs has a melting and ablation threshold at $10^{12}$ W/cm$^2$ and $1.75 \times 10^{12}$ W/cm$^2$, respectively[3]. Crystalline silicon is known to have an almost constant ablation threshold at 0.2J/cm$^2$ for the pulse duration between 5 fs and 400 fs[4], which ranges between 1.25 to $4 \times 10^{13}$ W/cm$^2$ in terms of intensity. ZnTe has a damage threshold of $\sim 1.5 \times 10^{13}$ W/cm$^2$ for 30 fs, 800 nm pulse[5].

Among the plasma-based sources, two-color scheme has been of special attention, in which non-relativistic femtosecond (fs) laser with a fundamental frequency $\omega$ and its second harmonic $2\omega$ is used to ionize gas targets, producing plasma that radiates intense THz wave. While this method can routinely generate THz pulses as intense as those obtained by a single-color ($\omega$-only) relativistic laser, just increasing the laser intensity does not directly lead to generation of stronger THz wave; it is experimentally shown that, over the laser intensity of $10^{15}$ W/cm$^2$, the THz yield would saturate up[9], and blue-shifts will occur to the THz wave[10,11].

For the development of stronger THz source, THz radiation mechanism at such a high laser intensity has to be made clear. Despite of numerous experimental works on the topic, there has been a lack of theoretical and numerical examination of THz radiation. Particle-in-cell simulation that self-consistently include plasma and atomic physics can give the detailed time evolution of femtosecond laser and plasma, which can be difficult to directly observe in experimental means[12].

Amplification of THz wave in the plasma is an intriguing topic, but strong enhancement of THz power has not been reported[13,14].

Also noticeably lacking in the current literature is the narrowband source of intense THz source using laser-plasma interaction. So far, all plasma-based sources radiates in a broad spectrum, sometimes over a range of 100 THz.

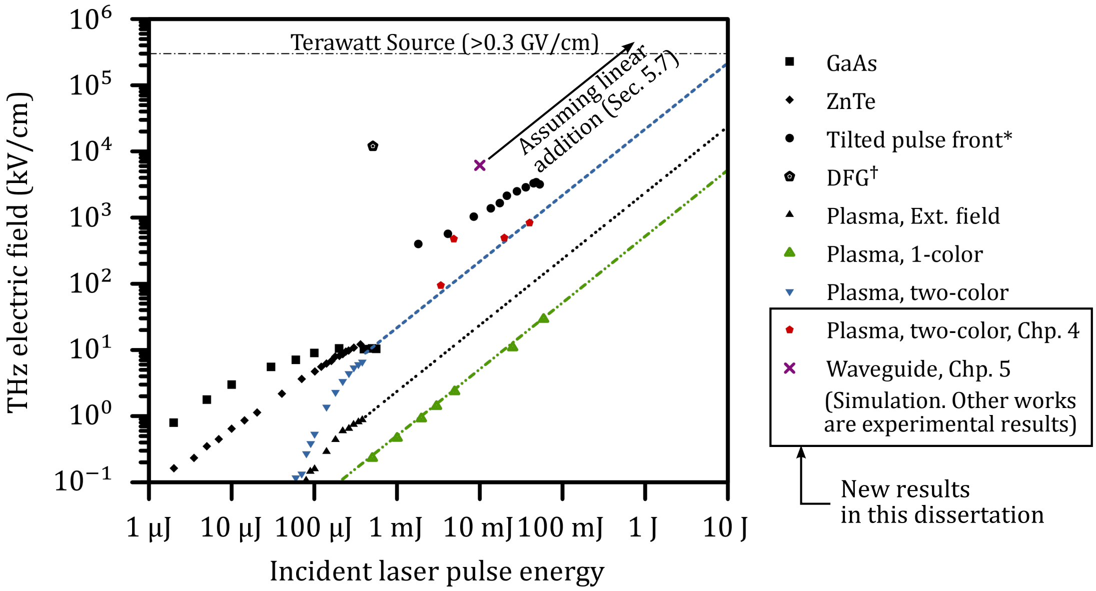


Figure 1.2: Current state of various THz sources. Fig. 4 in ref. 6 is adopted with more recent data for new generation schemes including those obtained in this dissertation.
*THz field obtained with tilted pulse front method is estimated assuming the focused diameter of 1 mm and pulse duration of 1 ps from data available at ref. 7.
†Type-I Difference frequency generation using GaAs with a thickness of 140 μm[8].

The realization of narrowband source would bring new interest in THz spectroscopy and applications involving resonant interaction between strong THz wave and material.

## 1.1 Organization of dissertation

This dissertation is organized as follows.

In Chp. 2, models for several THz generation mechanism using laser-plasma interaction are introduced, which will be referred in the subsequent chapters.

In Chp. 3, detailed view of the plasma and generated THz radiation using particle-in-cell simulation is presented for high laser intensity studied to date. Characteristics of THz radiation depending on the laser intensity and polarization are studied. Most importantly, the dependence of THz power on laser intensity has been studied for the first time for laser intensity higher than $10^{16}$

W/cm$^2$. The time evolution of the THz spectrum and frequency upshift of incident laser proofs the beat-wave model proposed in Sec. 2.4.

In Chp. 4, the possibility of THz amplification is suggested with experimental results. An order of magnitude increase in terahertz (THz) power is observed, and it is shown that such an enhancement may be attributed to formation of an asymmetric plasma profile in which the plasma density increases steeply in the head and decreases gradually in the tail. A one-dimensional model with and without accounting for amplification of THz wave has been derived, and a comparison of those two cases against the experimental results implies that the THz wave may have been amplified during its propagation in the plasma.

In Chp. 5, the possibility of a novel scheme for narrowband intense THz wave source using plasma waveguide is demonstrated with proof-of-principle particle-in-cell simulations. The waveguide makes the mixing time for THz generation longer, resulting in enhanced THz field amplitude by about two orders, compared to that without plasma waveguide. By the proposed scheme, generation of coherent TW THz radiation with quasi-monochromatic spectral distribution may be realized with a compact femtosecond laser.

Finally, the results are summarized in Chp. 6.

## References

[1] M. S. Sherwin, C. A. Schmuttenmaer, and P. H. Bucksbaum, eds., *Report of DOE-NSF-NIH Workshop on Opportunities in THz Science* (2004).

[2] H. Zhuo, "Personal communication," (2014).

[3] A. Cavalleri, K. Sokolowski-Tinten, J. Bialkowski, and D. von der Linde, "Femtosecond laser ablation of gallium arsenide investigated with time-of-flight mass spectroscopy," Applied Physics Letters **72**, 2385 (1998).

[4] J. Bonse, S. Baudach, J. Krüger, W. Kautek, and M. Lenzner, "Femtosecond laser ablation of silicon–modification thresholds and morphology," Applied Physics A **74**, 19 (2014).

[5] G. Berden, S. Jamison, A. MacLeod, W. Gillespie, B. Redlich, and A. van der Meer, "Electro-Optic Technique with Improved Time Resolution for Real-Time, Nondestructive, Single-Shot Measurements of Femtosecond Electron Bunch Profiles," Physical Review Letters **93**, 114802 (2004).

[6] T. Löffler, M. Kreß, M. Thomson, T. Hahn, N. Hasegawa, and H. G. Roskos, "Comparative performance of terahertz emitters in amplifier-

laser-based systems," Semiconductor Science and Technology **20**, S134 (2005).

[7] J. A. Fülöp, L. Pálfalvi, S. Klingebiel, G. Almási, F. Krausz, S. Karsch, and J. Hebling, "Generation of sub-mJ terahertz pulses by optical rectification." Optics Letters **37**, 557 (2012).

[8] F. Junginger, A. Sell, O. Schubert, B. Mayer, D. Brida, M. Marangoni, G. Cerullo, A. Leitenstorfer, and R. Huber, "Single-cycle multiterahertz transients with peak fields above 10 MV/cm." Optics Letters **35**, 2645 (2010).

[9] K. Y. Kim, A. J. Taylor, J. H. Glownia, and G. Rodriguez, "Coherent control of terahertz supercontinuum generation in ultrafast laser–gas interactions," Nature Photonics **2**, 605 (2008).

[10] T. Bartel, P. Gaal, K. Reimann, M. Woerner, and T. Elsaesser, "Generation of single-cycle THz transients with high electric-field amplitudes." Optics Letters **30**, 2805 (2005).

[11] X.-Y. Peng, C. Li, M. Chen, T. Toncian, R. Jung, O. Willi, Y.-T. Li, W.-M. Wang, S.-J. Wang, F. Liu, A. Pukhov, Z.-M. Sheng, and J. Zhang, "Strong terahertz radiation from air plasmas generated by an aperture-limited Gaussian pump laser beam," Applied Physics Letters **94**, 101502 (2009).

[12] C. K. Birdsall and A. B. Langdon, *Plasma Physics via Computer Simulation*, 1st ed. (Taylor & Francis, 2004).

[13] M.-K. Chen, J. H. Kim, C.-E. Yang, S. S. Yin, R. Hui, and P. Ruffin, "Terahertz generation in multiple laser-induced air plasmas," Applied Physics Letters **93**, 231102 (2008).

[14] J. Dai, X. Xie, and X.-C. Zhang, "Terahertz wave amplification in gases with the excitation of femtosecond laser pulses," Applied Physics Letters **91**, 211102 (2007).

# Chapter 2

# Mechanisms of THz Radiation in Plasma

## 2.1 Introduction

Finding a model that explains the THz radiation during the laser-plasma interaction is important not only for our understanding of the physical process, but also for predicting the dependence of THz intensity on the incident laser intensity. There are two successful model at present for THz generation by two-color laser scheme: four-wave mixing[1] (FWM) and photocurrent model[2].

FWM is briefly introduced in Sec. 2.2 with a new phase matcing condition. Photocurrent model is described along with several simulations in Sec. 2.3. They both agree well with experiments, but may give incorrect predictions as the laser intensity increases, because they ignore the effect of steep electron density ramp that emerges at higher pump lase intensity.

For higher laser intensity $\sim 10^{16}\,\mathrm{W/cm^2}$, as a possibly dominant THz generation mechanism, a beat-wave model that takes into account the ionization front is proposed for the first time Sec. 2.4.

Note that for even higher laser intensity, i.e., relativistic laser regime ($\sim 10^{19}\,\mathrm{W/cm^2}$), electron current driven by the ponderomotive force of the laser has been reported to be dominant[3]. It is, however, out of scope of this dissertation.

## 2.2 Four-wave mixing

Four wave mixing (FWM) has been proposed to explain the enhancement of terahertz radiation from the laser-produced plasma with the addition of second harmonic component to a single-color laser[1,4]. The third-order nonlinear process involves three incident waves, whose frequencies are added to nearly zero, which is the frequency of fourth wave, the terahertz wave. With the nonlinear susceptibility $\chi^{(3)}\left(\Omega : 2\omega + \Omega, -\omega', -\omega'\right)$ where $\Omega$ is the radiated THz frequency, the third-order polarization responsible for the THz emission is

$$P_i^{(3)}(t) = \chi_{ijkl}^{(3)} E_j^{2\omega}(t)\, E_k^{\omega'}(t)\, E_l^{\omega'}(t) \tag{2.1}$$

where $E_{2\omega}(t) = \frac{1}{2} E_{2\omega} \exp\left[i\left(2\omega t + \varphi\right)\right] + c.c.$, $E_{\omega}(t) = \frac{1}{2} E_{\omega} \exp\left[i\left(\omega t\right)\right] + c.c.$, and $\varphi$ is the phase difference between them[1]. The model predicts the amplitude of THz field as

$$E_{\mathrm{THz}} = \chi^{(3)} \sqrt{I_{2\omega}} I_{\omega} \cos\left(\varphi\right). \tag{2.2}$$

An efficient THz generation with FWM requires both the energy conservation,

$$\Omega = 2\omega - \omega' - \omega', \tag{2.3}$$

and the phase mathcing, or the momentum conservation

$$\sum_n \boldsymbol{k}_{\mathrm{n}} = \boldsymbol{k}_{\Omega} \tag{2.4}$$

where the summation on the left term is over the incident photons[5].

Wave vector of electromagnetic wave in cold plamsa with a plasma frequency $\omega_p$ is given by

$$c^2 k^2 = \omega^2 - \omega_p^2, \tag{2.5}$$

where $c$ is the speed of light, $\omega$ is the frequency of the light. Using the Maclaurin series of $\sqrt{1-x} = 1 - x/2 - x^2/8 - \cdots$, it can be approximated as

$$k = \frac{\omega}{c} - \frac{\omega_p^2}{2c\omega}, \tag{2.6}$$

given that $\omega \gg \omega_p$.

So far, however, the discussion on the FWM assumed that THz wave has a zero frequency and zero $k$-vector. It is a valid approximation because the frequency of pump wave for the most common case (0.8 μm wavelength) is 375 THz, more than two orders larger than THz wave. However, it means that only the phase matching conditions where all pump beams propagate collinearly have been considered.

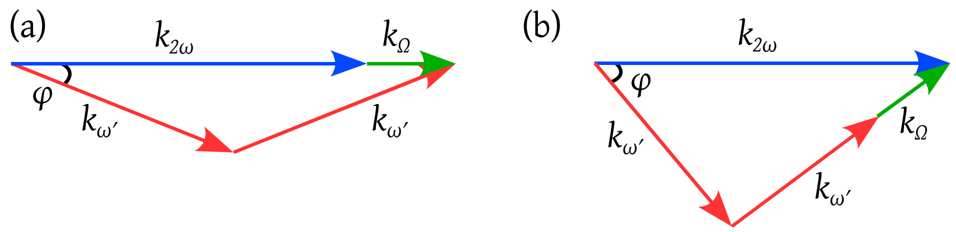


Figure 2.1: Phase-matching conditions for Four-Wave Mixing process

In most experiments, we focus laser beams to obtain laser intensity higher than ionization threshold. During the focusing, non-collinear components with considerable intensity emerges, and may contribute to THz wave generation via FWM.

Below, I derive phase-matching angles for those cases. If we assume that THz wave has a finite $k$-vector, it is easy to see that there are only two phase-matching conditions; one for forward propagating THz wave emission, and the other for tilted THz emission.

### 2.2.1 Phase matching for forward propagating THz

The orientation of propagation vectors are shown in Fig. 2.1(a). From the cosine formula,

$$\begin{aligned}(k_{2\omega}+k_\Omega)^2 &= k_{\omega'}^2 + k_{\omega'}^2 - 2k_{\omega'}^2\cos(\pi-2\varphi)\\ &= 2k_{\omega'}^2(1+\cos 2\varphi)\\ &= 4k_{\omega'}^2\cos^2\varphi\\ &= (2k_{\omega'}\cos\varphi)^2 . \end{aligned} \tag{2.7}$$

It can be resolved into factors as

$$(k_{2\omega}+k_\Omega+2k_{\omega'}\cos\varphi)(k_{2\omega}+k_\Omega-2k_{\omega'}\cos\varphi)=0. \tag{2.8}$$

Here, we substitute

$$k_{2\omega} = \frac{2\omega}{c} - \frac{\omega_{\mathrm{p}}^2}{2c \cdot 2\omega} \tag{2.9a}$$

$$k_{\omega'} = \frac{\omega'}{c} - \frac{\omega_{\mathrm{p}}^2}{2c \cdot \omega'} \tag{2.9b}$$

$$\begin{aligned} k_{\Omega} &= \frac{1}{c}\sqrt{\Omega^2 - \omega_p^2} \\ &\sim \frac{\Omega}{c} - \frac{\omega_{\mathrm{p}}^2}{2c \cdot \Omega} \end{aligned} \tag{2.9c}$$

to obtain

$$(2\omega + \Omega \pm 2\omega' \cos\varphi) - \frac{\omega_p^2}{2}\left(\frac{1}{2\omega} + \frac{1}{\Omega} \pm \frac{2}{\omega'}\cos\varphi\right) = 0. \tag{2.10}$$

Since $\Omega = 2\,(\omega' - \omega)$,

$$[2\omega + 2\,(\omega' - \omega) \pm 2\omega' \cos\varphi] - \frac{\omega_p^2}{2}\left[\frac{1}{2\omega} + \frac{1}{2\,(\omega' - \omega)} \pm \frac{2}{\omega}\cos\varphi\right] = 0. \tag{2.11}$$

For the sake of simplicity, we substitute $\omega'$ with $x$, $\omega$ with $y$, and $\omega_{\mathrm{p}}$ with $z$. We define $x' = x/z$, $y' = y/z$, and $z' = z/z = 1$ to make the equation simpler:

$$[2y + 2\,(x - y) \pm 2x \cos\varphi] - \frac{1}{2}\left[\frac{1}{2y} + \frac{1}{2\,(x - y)} \pm \frac{2}{x}\cos\varphi\right] = 0. \tag{2.12}$$

Arranging for the phase matching angle,

$$\pm\cos\varphi = \frac{x^2\,(8y^2 - 8xy + 1)}{4y\,(2x^2 - 1)\,(x - y)}. \tag{2.13}$$

The phase matching angle found by this equation is shown in the Fig. 2.2.

Note that the phase matching angle $\varphi$ determines the maximum $F$-number $N_{\max}$ of the focusing lens by

$$N_{\max} = \frac{f}{D} < \frac{1}{2\tan\varphi}, \tag{2.14}$$

where $f$ is the focal length and $D$ is the beam diameter on the lens. For example, optimal generation of 5 THz wave requires the maximum $F$-number of 14.3.

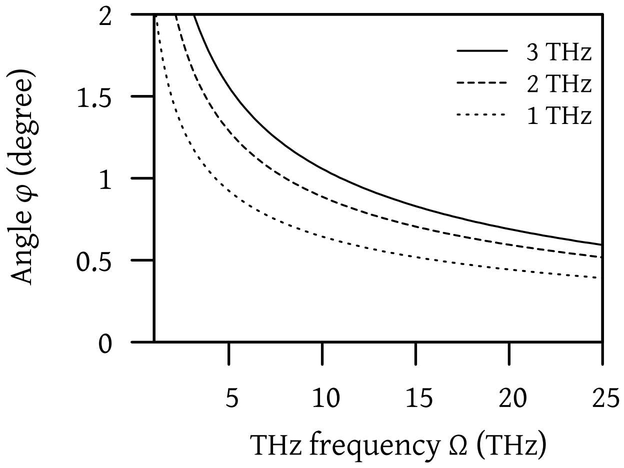


Figure 2.2: Phase matching angles for forward THz generation by FWM process in plasma with different plasma frequency $\omega_\mathrm{p}$ from 1 to 3 THz. The fundamental frequency of the incident pulse (800 nm, Ti:sapphire laser) is 375 THz.

We can see from Fig. 2.2 that the higher plasma frequency $\omega_p$, focusing with a higher $F$-number is necessary.

### 2.2.2 Phase matching for tilted propagating THz

Its orientation of propagation vectors are shown in Fig. 2.1(b). From the cosine formula,

$$\begin{aligned}(k_\omega + k_\Omega)^2 &= k_{\omega'}^2 + k_{2\omega}^2 - 2k_{\omega'}k_{2\omega}\cos\varphi \\ \Leftrightarrow k_\Omega^2 - k_{2\omega}^2 &= -2k_{\omega'}k_\Omega - 2k_{\omega'}k_{2\omega}\cos\varphi \\ &= -2k_{\omega'}\left(k_\Omega + k_{2\omega}\cos\varphi\right). \end{aligned} \tag{2.15}$$

Using Eq. (2.9), The left hand side can be written as

$$\frac{1}{c^2}\left(\Omega^2 - 4\omega^2\right) = -\frac{1}{c^2}\left(4\omega^2 - \Omega^2\right), \tag{2.16}$$

since $\omega > \Omega$. While the right hand side can be represented as

$$-\frac{2}{c^2}\left(\omega' - \frac{\omega_p^2}{2}\right)\left[\Omega - \frac{\omega_p^2}{2}\frac{1}{\Omega} + \left(2\omega - \frac{\omega_p^2}{2}\frac{1}{2\omega}\right)\cos\varphi\right]. \tag{2.17}$$

For the sake of simplicity, we substitute $\omega'$ with $x$, $\omega$ with $y$, and $\omega_\mathrm{p}$ with $z$.

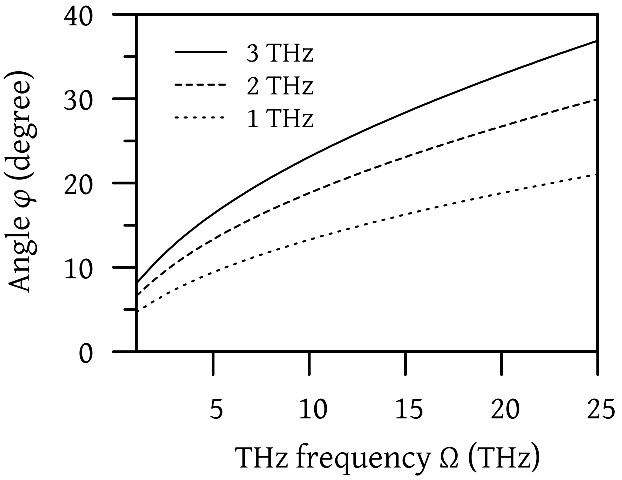


Figure 2.3: Phase matching angles for tilted THz generation by FWM process in plasma with different plasma frequency $\omega_\mathrm{p}$ from 1 to 3 THz. The fundamental frequency of the incident pulse (800 nm, Ti:sapphire laser) is 375 THz.

Also note that $\Omega$ becomes $2\,(x-y)$. Then defining $x' = x/z$, $y' = y/z$, and $z' = z/z = 1$ to make the equation simpler:

$$4x\,(2y-x) = 2\left(x - \frac{z^2}{2x}\right)\left[2\,(x-y) - \frac{z^2}{4\,(x-y)} + \left(2y - \frac{z^2}{4y}\right)\cos\varphi\right]. \tag{2.18}$$

Solving for the phase matching angle $\varphi$:

$$\cos\varphi = \frac{y\,(48x^2y^2 - 8y^2 - 80x^3y + 16xy + 32x^4 - 6x^2 - 1)}{(2x^2-1)\,(y-x)\,(8y^2-1)}. \tag{2.19}$$

The phase matching angle found by this equation is shown in the Fig. 2.3.

Since the phase matching angle is large ($> 5°$), the maximum $F$-number of the focusing lens is smaller ($< 5.7$) than that for the forward THz generation.

## 2.3 Photocurrent model

Photocurrent model is a microscopic model applying the well-known three-step model for high harmonic generation to THz radiation[6]. The laser field is represented as

$$E_L(t) = E_\omega \cos \omega t + E_{2\omega} \cos(2\omega t + \theta)$$

where $E_\omega$ and $E_{2\omega}$ are amplitudes of the red ($\omega$) and the blue ($2\omega$) electric fields, respectively, and $\theta$ is the phase difference between those two. Electric field whose intensity is higher than about $10^{14}\,\mathrm{W/cm^2}$ can induce tunnel ionization. Electrons generated by tunnel ionization are accelerated under the external laser field, resulting in a finite drift motion and electron current density in transverse direction. The far-field radiation is proportional to the time-derivate of electron current density:

$$E_c \propto \frac{\mathrm{d}J(t)}{\mathrm{d}t}. \tag{2.20}$$

The DC component of this electromagnetic field is regarded as the THz wave. It is shown in ref. 6 that the far-field terahertz field is proportional to

$$E_{\mathrm{THz}} \propto f\left(E_\omega\right) E_{2\omega} \sin\theta, \tag{2.21}$$

with the dependency on the electric field of the $\omega$ component is given by

$$f(E_\omega) = \sqrt{\frac{E_a}{E_\omega}} \exp\left(-\frac{2}{3}\frac{E_a}{E_\omega} - 3\frac{E_\omega}{E_a}\right), \tag{2.22}$$

where $E_a = 5.14 \times 10^9\,\mathrm{V/cm}$ is the atomic field on the ground state electron in a hydrogen atom.

Experiments to verify the Eq. (2.22) is performed as described in Sec. 4.3. Note that in the derivation, it has been assumed that $E_\omega \gg E_{2\omega}$ and the electron density $N_e$ is much lower than the initial gas density[7]. From Eq. (2.22), it is evident $f\left(E_\omega\right)$ is not a quadratic of $E_\omega$, indicating that the terahertz generation mechanism is not a third order nonlinear process. In addition, it shows that $E_{\mathrm{THz}}$ scales linearly $E_{2\omega}$. Another important notion of this model is that the terahertz radiation originates from ionization. If the laser field does not liberate any electrons from a gas or preformed plasma, no terahertz radiation is expected.

The model also predicts that the THz generation along the long plasma filament is sinusoidally modulated because 1) the THz generation efficiency of the two-color laser scheme depends on the phase between the frequency components in the incident wave ($\omega$ and $2\omega$), and 2) the refractive index of the plasma depends on the frequency of the propagating light. The phase change can be estimated by

$$\Delta\theta = \frac{3\pi}{4}\frac{d}{\lambda}\frac{N_e}{N_c} \tag{2.23}$$

where $d$ is the propagation distance in the plasma, $\lambda$ is the fundamental wavelength, $N_e$ is the plasma density, and $N_c$ is the critical density for the fundamental wave[6]. The distance $L_{\text{hp}}$ that the phase changes by $\pi/2$ is

$$L_{\text{hp}} = \frac{2}{3}\frac{N_c}{N_e}\lambda. \tag{2.24}$$

For example, $L_{\text{hp}}$ is 7.6 mm for 1 THz with the fundamental wavelength of 800 nm and the critical density for the 1 THz light, $1.24 \times 10^{16}\,\text{cm}^{-3}$ as the plasma electron density $N_e$. For higher THz frequency $\nu_p$, it decrease quadratically as $7.6/\nu_p^2$ [mm].

### 2.3.1 Simulations

A simulation code is written in C++ for calculation of the plasma current and THz radiation from an point particle that is initially electrically neutral.

Tunnel ionization by the intense electric field of the incident laser generates electrons*. The electric field of the incident laser then accelerates the liberated electrons. The $v \times B$ term in the Lorentz force is ignored since the laser intensity is non-relativistic. We can calculate the contribution to the current by accumulating the product between the liberated electron density and its acceleration. The electric field of the electromagnetic radiation by the time-varying current is calculated by Eq. (2.20). The electric field under 100 THz is then calculated by inverse Fourier transform with a low-pass filter applied to the spectrum of the radiated electric field.

Figure 2.4 to the Fig. 2.6 show the incident electric field of the laser, THz electric field, current and the evolution of the electron density for the peak

*The simulation calculates the ionization at a single point by field-ionization using the model of Ammosov, Delone, and Krainov[8,9] in which the ionization rate is given by

$$W = 1.61\omega_{\text{a.u.}}\frac{Z^2}{n_{\text{eff}}^{4.5}}\left(10.87\frac{Z^3}{n_{\text{eff}}^4}\frac{E_{\text{a.u.}}}{E}\right)^{2n_{\text{eff}}-1.5}\exp\left(-\frac{2}{3}\frac{Z^3}{n_{\text{eff}}^3}\frac{E_{\text{a.u.}}}{E}\right)$$

where $\omega_{\text{a.u.}}$ is the atomic unit of frequency ($= 4.1 \times 10^{16}\text{s}^{-1}$).

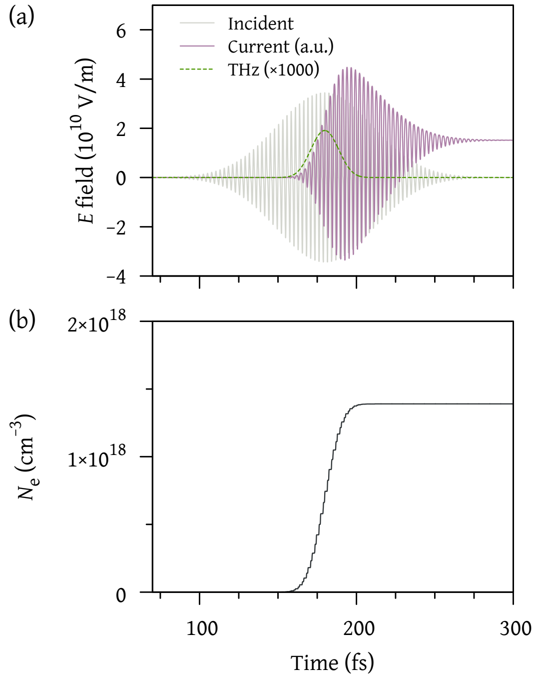


Figure 2.4: (a) Microscopic current and the THz radiation generated by a laser pulse with its peak intensity at $10^{14}$ W/cm$^2$. (b) Evolution of the electron density

laser intensity of the fundamental frequency at $10^{14}$, $10^{15}$, and $10^{16}$ W/cm$^2$.

Figure 2.7 compares the spectrum of the radiation generated from plasma current. Figure 2.8 shows the dependence of the amplitude of THz wave against that of the second harmonic with a linear fit by Eq. (2.21).

Note that in the photocurrent theory, the THz intensity has a complex dependency on the intensity of the fundamental wave, as represented by Eq. (2.22). Such a dependency has not been reported to date. It may be attributed to the fact that the model assumes a hydrogen-like atom, and the dimension is zero, i.e., the model considers a single point.

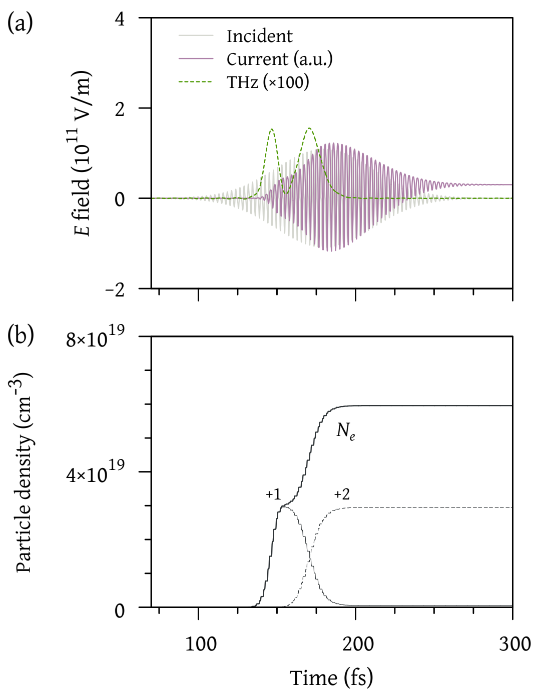


Figure 2.5: (a) Microscopic current and the THz radiation generated by a laser pulse with its peak intensity at $10^{15}\,W/cm^2$. (b) Evolution of the particle density, including the electron density and ion densities of different valence.

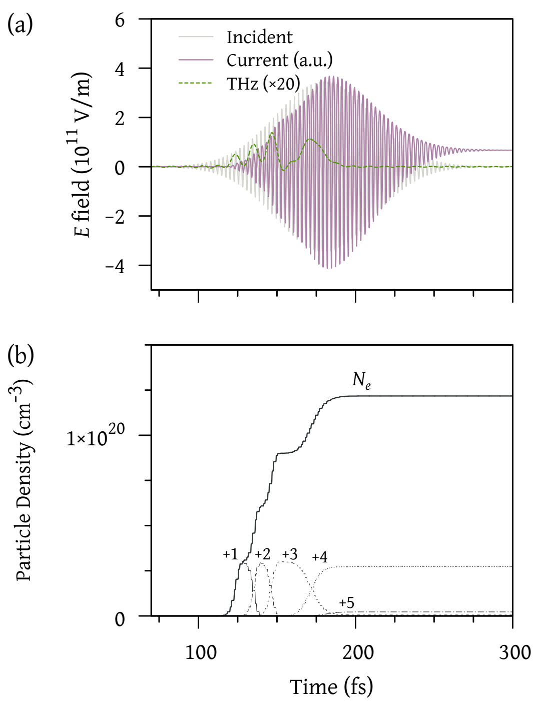


Figure 2.6: (a) Microscopic current and the THz radiation generated by a laser pulse with its peak intensity at $10^{16}\,W/cm^2$. (b) Evolution of the particle density, including the electron density and ion densities of different valence.

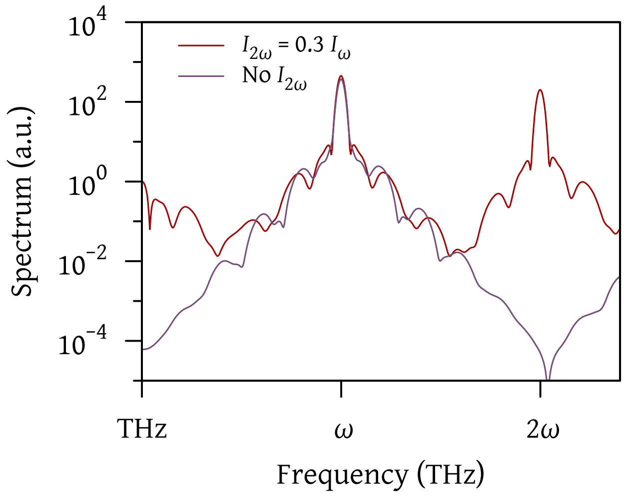


Figure 2.7: Spectrum of the electric field radiated from the plasma current for the incident laser intensity of $10^{16}\,\mathrm{W/cm^2}$.

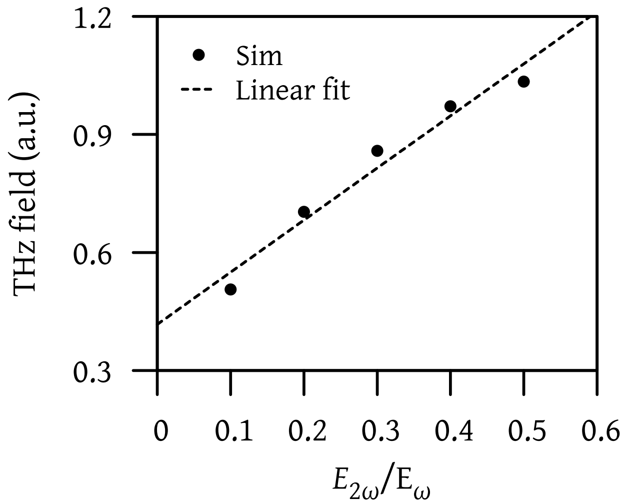


Figure 2.8: Change in the THz amplitude depending on the amplitude of 2$\omega$ component of incident laser.

## 2.4 Beat-wave model

Here I describe the THz radiation mechanism for laser intensities around $10^{16}\,\mathrm{W/cm^2}$. It will be later referred in the discussion of the particle-in-cell simulation in Chp. 3.

As in the photocurrent model, we inspect the origin of THz radiation in the motion of electrons. We assume plain wave with electric field linearly polarized along $y$ direction ($\boldsymbol{E} = E\boldsymbol{i}_y$, which in turn means magnetic field is along $z$ direction: $\boldsymbol{B} = B\boldsymbol{i}_z$) is propagating toward positive $x$ direction. See Fig. 2.9 for the rectangular coordinates.

Here we look into the motion of an electron under electromagnetic fields of two-color laser ($\omega_0, 2\omega_0$) and its frequency-shifted light ($\omega_0 + \omega_{\mathrm{shift}}$). The electric field can be expressed as

$$E = A_0 \cos\left[\left(\omega_0 + \omega_{\mathrm{shift}}\right) t\right] + A_1 \cos\left(\omega_0 t\right) + A_2 \cos\left(2\omega_0 t\right), \tag{2.25}$$

where $A_0$, $A_1$ and $A_2$ are the amplitude of the frequency-shifted, the fundamental and the second harmonic components. Amplitude of the frequency-shifted wave is far weaker than that of the original wave.

For simplicity in later development of expression, we normalize all frequencies by $\omega_{\mathrm{shift}}$ after substituting $\omega_0$ with $M\omega_{\mathrm{shift}}$, where $M$ is positive real.

$$E = A_0 \cos\left[\left(1 + M\right) t\right] + A_1 \cos\left(Mt\right) + A_2 \cos\left(2Mt\right), \tag{2.26}$$

We can use Lorentz's equation without relativistic correction to describe

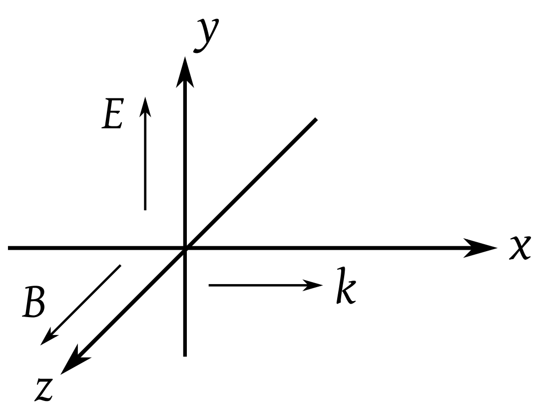


Figure 2.9: Cartesian coordinate system and the axis of electromagnetic wave

the motion of electron:

$$m\dot{v}_x = -\frac{e}{c}v_y B \tag{2.27a}$$

$$m\dot{v}_y = -eB + \frac{e}{c}v_x B \tag{2.27b}$$

The equation of motion is nonlinear, which can be linearized up to first degree by assuming that $v_x/c \ll 1$ and $v_y/c \ll 1$, and solving in the following procedure:

1. Solve $m\dot{v}_y^{(0)} = -eE$ for $v_y^{(0)}$, the zeroth order $y$-velocity.
2. Substitute the $v_y$ into $m\dot{v}_x^{(0)} = -e/c \cdot v_y^{(0)} B$ to obtain the first derivative of $v_x$ in zeroth degree.
3. Solve for the first degree of $y$-velocity by solving $m\dot{v}_y^{(1)} = e/c \cdot v_x^{(0)} B$.
4. The $y$-velocity, which aligns with the polarization of laser light is then $v_y = v_y^{(0)} + v_y^{(1)}$.

It is solved for two cases. Firstly, it is shown that without second harmonic component ($2\omega_0$) in the laser field, THz yield by beat-wave is theoretically zero. Secondly, it is shown that with a second harmonic components, THz wave at the frequency twice the up-shift frequency $\omega_{\text{shift}}$ appears. It matches well with the PIC simulation in Chp. 3.

### 2.4.1 Without second harmonic component

Without the second harmonic component, the electric field is given as

$$E = A_0 \cos\left[(1+M)\,t\right] + A_1 \cos(Mt) \tag{2.28}$$

The zeroth order $y$-velocity is

$$\begin{aligned} v_y^{(0)} &= -\frac{e}{m}\int E(t)\,\mathrm{d}t \\ &= -\frac{e}{m}\left\{\frac{A_0 \sin\left[(1+M)\,t\right]}{1+M} + \frac{A_1 \sin(Mt)}{M}\right\} \end{aligned} \tag{2.29}$$

The zeroth order $x$-velocity is

$$v_x^{(0)} = \frac{e^2}{2m^2 c}\left\{\frac{A_0 \sin\left[(1+M)\,t\right]}{1+M} + \frac{A_1 \sin(Mt)}{M}\right\}^2 \tag{2.30}$$

Finally, the first order $y$-velocity can be obtained and added to the zeroth order $y$-velocity to obtain the $y$-velocity as

$$v_y = \frac{e^3}{6m^3c^2}\left\{\frac{A_0 \sin\left[(1+M)\,t\right]}{1+M} + \frac{A_1 \sin(Mt)}{M}\right\}^3 \tag{2.31}$$

It does not have a low frequency components comparable to several harmonics of $\omega_{\text{shift}}$, thus no THz radiation from the motion of this electron is expected.

### 2.4.2 With second harmonic component, co-propagating with the fundamental one

The zeroth order $y$-velocity is

$$\begin{aligned} v_y^{(0)} &= -\frac{e}{m}\int E(t)\,\mathrm{d}t \\ &= -\frac{e}{m}\left\{\frac{A_0 \sin\left[(1+M)\,t\right]}{1+M} + \frac{A_1 \sin(Mt)}{M} + \frac{A_2 \sin(2Mt)}{2M}\right\} \\ &= -\frac{e}{m}\left\{\frac{A_0 \sin\left[(1+M)\,t\right]}{1+M} + \frac{\sin(Mt)\left[A_1 + A_2\cos(Mt)\right]}{M}\right\} \end{aligned} \tag{2.32}$$

The zeroth order $x$-velocity is

$$\begin{aligned} v_x^{(0)} &= -\frac{e}{mc}\int v_y^{(0)} B\,\mathrm{d}t \\ &= \frac{e^2}{cm^2}\left\{-\frac{A_0^2\cos\left[2(M+1)\,t\right]}{4(M+1)^2}\right. \\ &\qquad + \frac{A_0\left[A_1 + A_2\cos(Mt)\right]}{M(M+1)}\sin(Mt)\sin\left[(M+1)\,t\right] \\ &\qquad \left. - \frac{4A_1^2\cos(2Mt) - 8A_1A_2\sin(Mt)\sin(2Mt) + A_2^2\cos(4Mt)}{16M^2}\right\} + C \\ &\triangleq V_{Fx}(t) + C \end{aligned}$$

Note that due to the initial condition of $x$-velocity, the constant of integration is

$$\begin{aligned} C &= -V_{Fx}(0) \\ &= \frac{e^2}{cm^2}\left(\frac{A_0^2}{4(M+1)^2} + \frac{4A_1^2 + A_2^2}{16M^2}\right) \end{aligned} \tag{2.33}$$

The $x$-velocity can be simplified as

$$v_x^{(0)} = \frac{e^2}{2m^2cM^2(M+1)^2} \times \{A_0 M \sin[(M+1)t] + (1+M)[A_1 + A_2\cos(Mt)]\sin(Mt)\}^2 \tag{2.34}$$

In the similar fashion, the first order $y$-velocity can be obtained and added to the zeroth order $y$-velocity, resulting in the $y$-velocity as

$$v_y(t) = \frac{e^3}{6m^3c^2M^3(M+1)^3} \times \{A_0 M \sin[(M+1)t] + (1+M)[A_1 + A_2\cos(Mt)]\sin(Mt)\}^3 \tag{2.35}$$

Note that the change in the power in Eqs. (2.34) and (2.35). Expanding the Eqs. (2.35), we can find harmonics of the plasma frequency $\omega_{\text{shift}}$:

- Fundamental of $\omega_{\text{shift}}$

$$v_y(t;\omega_{\text{shift}}) = \frac{1}{8}\frac{e^3}{c^2m^3M^2(M+1)}A_0A_1A_2\sin(\omega_{\text{shift}}t) \tag{2.36}$$

- Second harmonic of $\omega_{\text{shift}}$

$$v_y(t;2\omega_{\text{shift}}) = \frac{1}{16}\frac{e^3}{c^2m^3M(M+1)^2}A_0^2A_2\sin(2\omega_{\text{shift}}t) \tag{2.37}$$

The ratio of the second harmonic and the first is

$$\frac{v_y(t;2\omega_{\text{shift}})}{v_y(t;\omega_{\text{shift}})} = \frac{1}{2}\frac{M}{M+1}\frac{A_0}{A_1} \simeq \frac{1}{2}\frac{A_0}{A_1} \tag{2.38}$$

Note that $A_0$ and $A_1$ are the amplitude of the frequency-shifted and the incident fundamental wave, respectively. Although the radiation at $2\omega_{\text{shift}}$ is weaker than $\omega_{\text{shift}}$ by an order, the latter may not be able to propagate in the plasma if it is overdense, i.e., $\omega_{\text{shift}} < \omega_{\text{p}}$ where $\omega_{\text{p}}$ is the plasma frequency given by $\omega_{\text{p}} = \sqrt{n_e e^2/m_e\epsilon_0}$ [Hz], where $n_e$ is the plasma electron density, $e$ the elementary charge, $m_e$ the electron mass, and $\epsilon_0$ the permittivity of vacuum.

## 2.5 Conclusion

In this chapter, I have introduced THz radiation mechanisms from laser-produced plasma for different laser intensities.

For the pump laser intensity around $10^{15}\,\mathrm{W/cm^2}$, models currently widely accepted in the literature of THz research, four wave mixing (FWM) and photocurrent model, give excellent agreement with experiments. In this dissertation, new phase matching conditions for THz radiation by FWM between oblique incident rays in a beam being focused. For the photocurrent model, a simulation code for a point source of THz radiation is written. It can be used for a rough estimation of THz generation efficiency. However, it ignores the effect of steep electron density ramp that emerges at higher pump lase intensity.

For higher intensity around $10^{16}\,\mathrm{W/cm^2}$, the beat-wave mechanism for THz wave generation is derived. It takes account of the the steep density ramp, where frequency-shift occurs and THz radiation at the harmonics of plasma frequency $\omega_\mathrm{p}$ can be generated by beat waves, arising between the frequency-shifted beam and incident two-color laser beams.

## References

[1] X. Xie, J. Dai, and X.-C. Zhang, "Coherent Control of THz Wave Generation in Ambient Air," Physical Review Letters **96**, 075005 (2006).

[2] K. Y. Kim, A. J. Taylor, J. H. Glownia, and G. Rodriguez, "Coherent control of terahertz supercontinuum generation in ultrafast laser–gas interactions," Nature Photonics **2**, 605 (2008).

[3] H. Hamster, A. Sullivan, S. Gordon, and R. Falcone, "Short-pulse terahertz radiation from high-intensity-laser-produced plasmas," Physical Review E **49**, 671 (1994).

[4] T. Bartel, P. Gaal, K. Reimann, M. Woerner, and T. Elsaesser, "Generation of single-cycle THz transients with high electric-field amplitudes." Optics Letters **30**, 2805 (2005).

[5] N. Bloembergen, "Conservation laws in nonlinear optics," Journal of the Optical Society of America **70**, 1429 (1980).

[6] K.-Y. Kim, J. H. Glownia, A. J. Taylor, and G. Rodriguez, "Terahertz emission from ultrafast ionizing air in symmetry-broken laser fields." Optics Express **15**, 4577 (2007).

[7] K.-Y. Kim, "Generation of coherent terahertz radiation in ultrafast laser-gas interactions," Physics of Plasmas **16**, 056706 (2009).

[8] B. Penetrante and J. Bardsley, "Residual energy in plasmas produced by intense subpicosecond lasers," Physical Review A **43**, 3100 (1991).

[9] M. V. Ammosov, N. B. Delone, and V. P. Krainov, "Tunnel ionization of complex atoms and of atomic ions in an alternating electromagnetic field," Sov Phys JETP **64**, 1191 (1986).

# Chapter 3

# Numerical Simulation on the Characteristics of THz wave from Plasma

## 3.1 Introduction

In this chapter, power, spectral characteristics, and angle distribution of terahertz radiation from air irradiated by a single ($\omega$) or two-color (fundamental $\omega$ and second harmonic $2\omega$) femtosecond laser pulses are analyzed for higher intensities, for which non-linear plasma effects on the propagation of laser and THz pulses become essential.

There are numerous physical processes that result in THz radiation and affect its propagation in the plasma during the laser pulse irradiation and afterward: frequency up-shift at the front of the pulse[1] and $k$-vector downshift in the rear, pulse modulation due to the refraction by the electron density[2,3], Doppler down-shifted light generation at steep ionization front[4–6], dispersion effects of plasma on THz radiation, etc.

It is found that THz radiation may be attributed to a beat wave generated at ionization front with $\omega$, $2\omega$ and frequency-upshifted $\omega$ components. THz power dependence on the laser intensity is found; at lower intensities, the THz power growth is much faster than the linear. Over $I > 10^{15}$ W/cm$^2$, the power increases slower than the linear. Along with the forward emission, strong power at around 30° occurs at high intensities. Ionization of air results in poor focusing of laser pulses and, therefore, THz emission efficiency becomes lower.

A two-dimensional PIC code, FPLaser2D[7,8] exploiting the moving window technique is used to study the characteristics of the THz radiation as linearly polarized laser pulses propagate in air under 0.6 atm. The simulation is simplified by including only neutral nitrogen atoms initially with a density at $3.0 \times 10^{19}\,\mathrm{cm}^{-3}$.* The variable particle weight method[8] were used to calculate field ionization up to the four-valent nitrogen ion. The dimension of the simulation window is 150 µm × 320 µm with a spatial resolution of $\lambda_{2\omega}/10$ (= 0.04 µm).

The laser pulse is spatiotemporally Gaussian with the pulse duration at 54 fs FWHM.** The beam waist $w_0$ of $\omega$ and $2\omega$ waves are assumed identical at 50 µm FWHM. The Rayleigh length, given by $Z_\mathrm{R} = \pi w_0^2/\lambda$ for a Gaussian beam where $\lambda$ is the wavelength, are 4.4 and 17.6 mm, for $\omega$ and $2\omega$ waves, respectively.

In the following sections, calculations are performed for both a single color case ($\lambda_\omega$ = 0.8 µm) and a two-color laser case (with its second harmonic $\lambda_{2\omega}$ = 0.4 µm). To observe the dependence of THz radiation characteristics on the laser intensity, the peak intensity of $\omega$ wave was varied from $10^{14}$ to $10^{16}\,\mathrm{W/cm^2}$. The total energy of $2\omega$ wave had been assumed 0.3 times that of the $\omega$ wave.

All results are given in the conventional units: density in the critical density ($6.1 \times 10^{21}\,\mathrm{cm}^{-3}$) for the second harmonics $\omega_{2\omega}$ and field strength in $mc\omega_{2\omega}/e$ units. Note that the laser pulse propagates from right to left side. Since a moving window technique is used, the left-most coordinate of figures, marked by XL, changes as $-v_w t$ where $v_w$ is the speed of moving window, which is identical to the speed of light in vacuum in present simulations, and $t$ is the simulation time.

## 3.2 Single-color case

Figure 3.1 shows the time-evolution of a single laser pulse in air with the peak intensity $I_\omega = 10^{16}\,\mathrm{W/cm^2}$ in the focus point. Figure 3.2(b-d) shows the electric field on the laser axis. Figure 3.2(a) shows the electric field along the transverse direction ($y$ axis). We can see modulations of the laser field strength both in longitudinal and transverse directions.

Particle densities including electrons and nitrogen ions are shown in Fig. 3.3. The maximal electron density in this case is $N_\mathrm{max} \approx 0.003 n_\mathrm{cr}$, which is about $2 \times 10^{19}\,\mathrm{cm}^{-3}$. Therefore, plasma is almost fully ionized. The

---

*If we assume that we can model the nitrogen gas $N_2$ with two nitrogen atoms, the density corresponding to 1 atm, 300 K nitrogen atom background is $4.9 \times 10^{19}\,\mathrm{cm}^{-3}$ using the ideal gas law.

**In the simulation code, incient electric field $E \propto \exp\left[-0.5\,(t/T)^2\right]$ where $T$ determines the intensity FWHM pulse duration as $2\sqrt{\ln 2}T$.

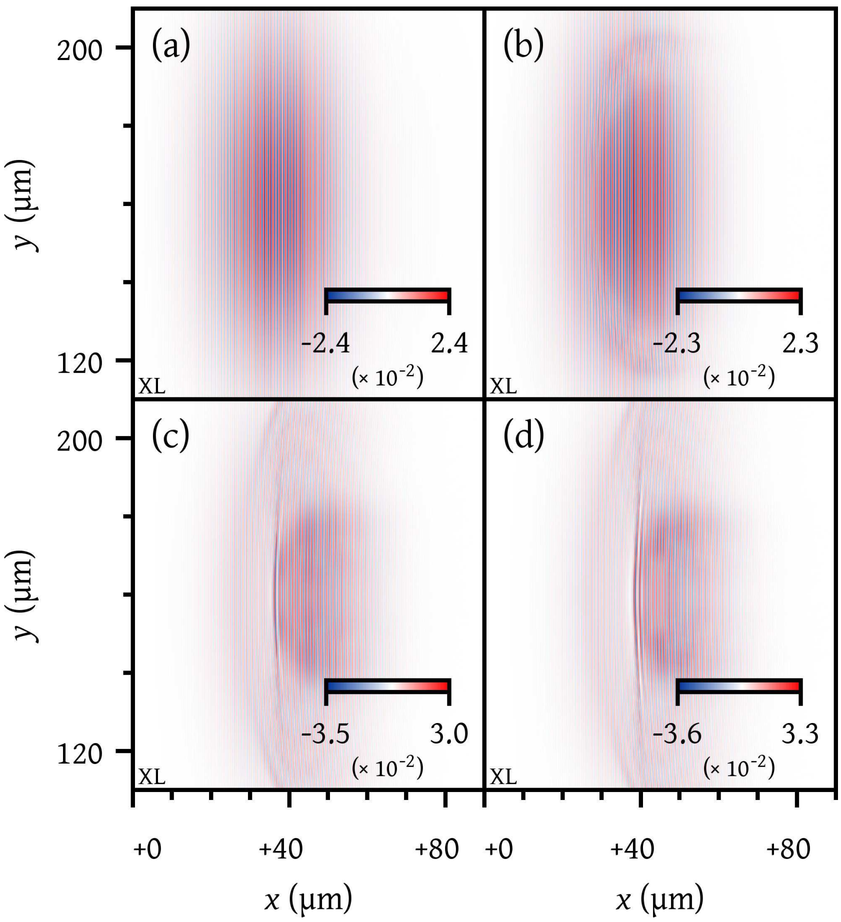


Figure 3.1: $p$-polarized electric field after the single-color laser pulse propagated from right to left (a) 0.1, (b) 1.1, (c) 1.8, and (d) 2.1 ps in the 0.6 atm air. The peak intensity is $I_\omega = 10^{16}\,\mathrm{W/cm^2}$.

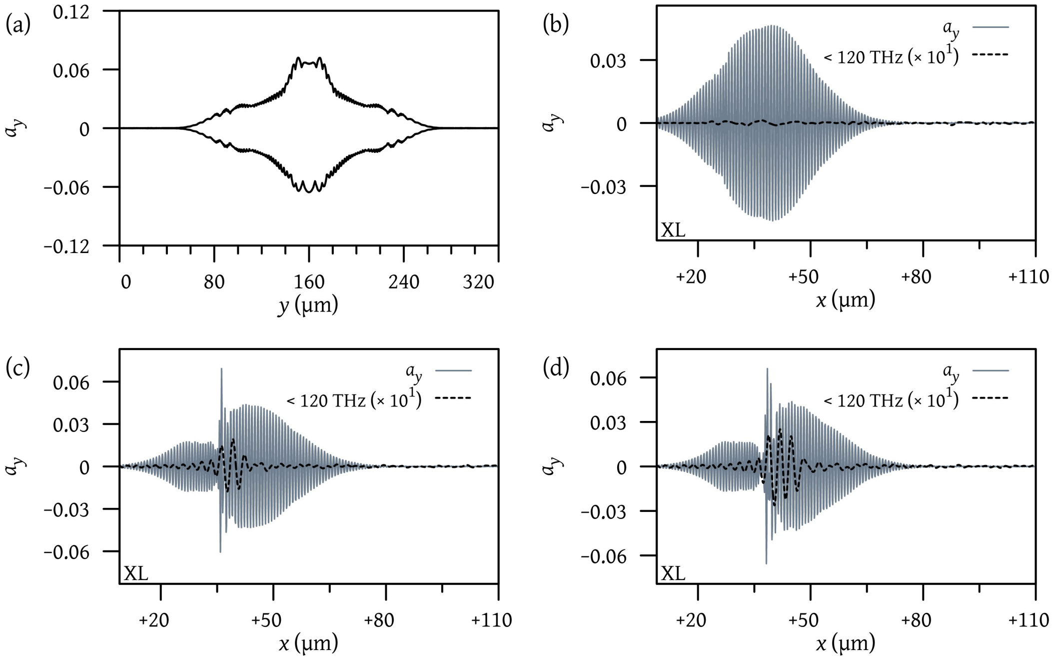


Figure 3.2: (a) transverse profile at 2.1 ps, and (b-d) profile along laser propagation axis $x$ corresponding to (b), (c) and (d) in Fig. 3.1.

maximal plasma frequency is $\omega_{\rm pl} \sim \omega/9$ or $\nu = \omega/2\pi \sim 40$ THz. We can see modulations of the laser field strength both in longitudinal and transverse directions, and weak electron and ion density modulations in the longitudinal direction. Higher Z ion's density is strongly modulated, being more sensitive to the field strength. The wavelength of this modulation is almost constant and is about 10 μm. Despite it is very close to the plasma wavelength (6.4 μm), the density modulation is attributed mostly to the process of pulse refraction on the plasma density gradient. The refraction of laser field results in the density decrease and, consequently weaker, but further refraction according to the eikonal equation:

$$\frac{\mathrm{d}\boldsymbol{n}}{\mathrm{d}l} = -\frac{1}{2}\nabla_{\perp}\left[N_e\left(\theta\right)/N_{cr}\right] \tag{3.1}$$

where $\boldsymbol{n}$ is the direction of light propagation along the curve $l$. The distance that the refraction become important can be estimated as $L \sim w_0 N_{cr}/N_{\rm e}$. In our case, it is close to the Rayleigh length; $L = 4.2$ mm and $Z_{\rm R} = 4.4$ mm.

The most powerful part of the THz radiation can be seen in Fig. 3.2(d) in the middle of the field. Its duration is about 70 fs which displays a broad spectrum of that long wavelength radiation. That agrees well with previous exper-

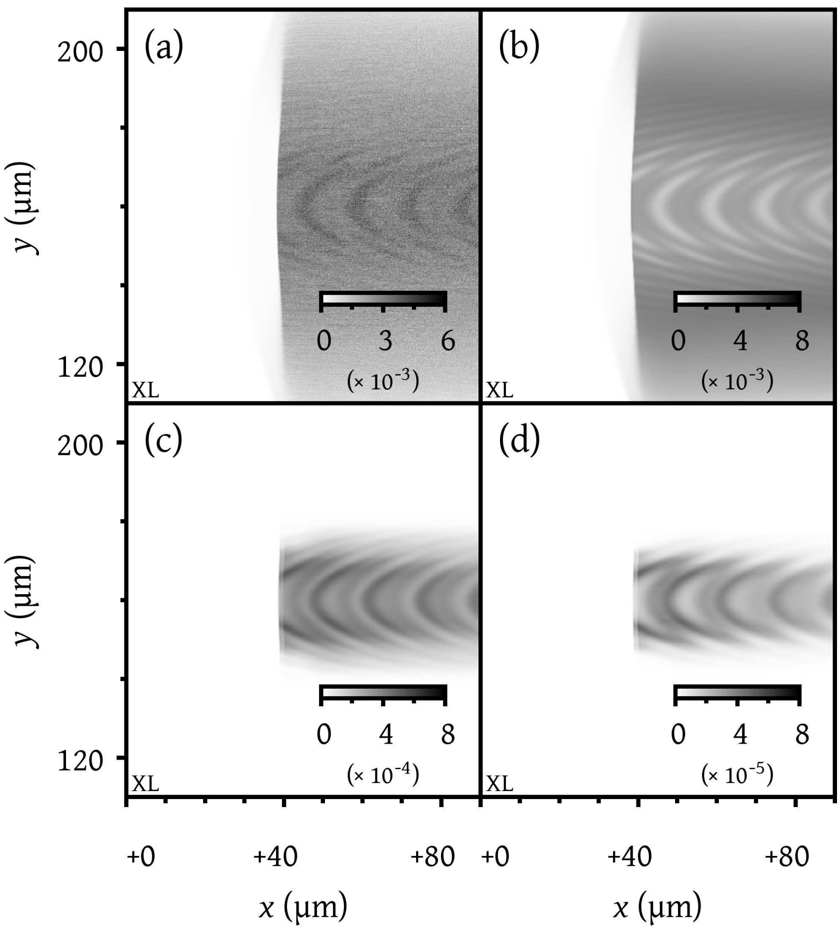


Figure 3.3: Electron and ion densities after a $p$-polarized single-color laser pulse propagated from right to left 2.1 ps in the 0.6 atm air. Peak intensity of $\omega$ is $I_{\omega} = 10^{16}\,\mathrm{W/cm^2}$. (a) electron density, (b-d) density of 1+, 2+ and 3+ nitrogen ion, respectively.

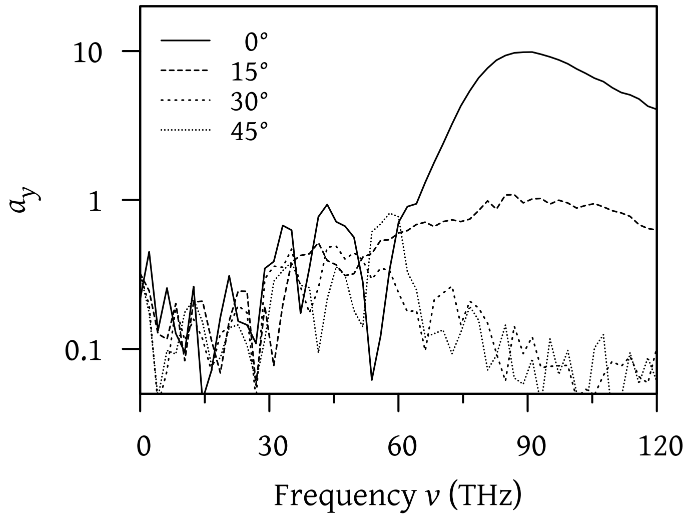


Figure 3.4: THz radiation spectrum along 0, 15, 30 and 45 degrees radiated from plasma produced by single-color laser pulse.

imental and theoretical works[9]. The THz pulse cuts the laser pulse into two parts: the front part, initially responsible for the optical ionization, is essentially depleted, while the second, rear part has almost intact Gaussian profile. Figure 3.4 shows the THz radiation spectrum obtained with the single-color laser pulse. We can see that the strongest radiation is emitted mostly at high frequency, over 80 THz, and propagates in the direction of laser pulse. The power of THz radiation in the frequency range below 30 THz is very weak.

### 3.2.1 Laser filament effect on beam waist

Before moving on to the two-color laser case, it may be appropriate to make a note on the effect of refraction by plasma generated by the incident laser as it propagates in the gas target.

Ionization of air by intense laser field usually begins before reaching the focal spot in the vacuum, and affects the focusing of laser pulse. To understand the effect of ionization on the pulse focus-ability, 3D simulation using FPLaser3D[10] is performed for a single laser pulse in atmosphere with its expected intensity in the focus point $I \sim 10^{16}\,\mathrm{W/cm^2}$. Figure 3.5 shows the dependence of maximal electric field of the pulse on the distance from the focus point. The result shows that the minimal size of its waist increases roughly by twice due to the refraction of the laser pulse by the plasma generated during the focusing of the laser in the air. This effect would reduce the resulting THz radiation.

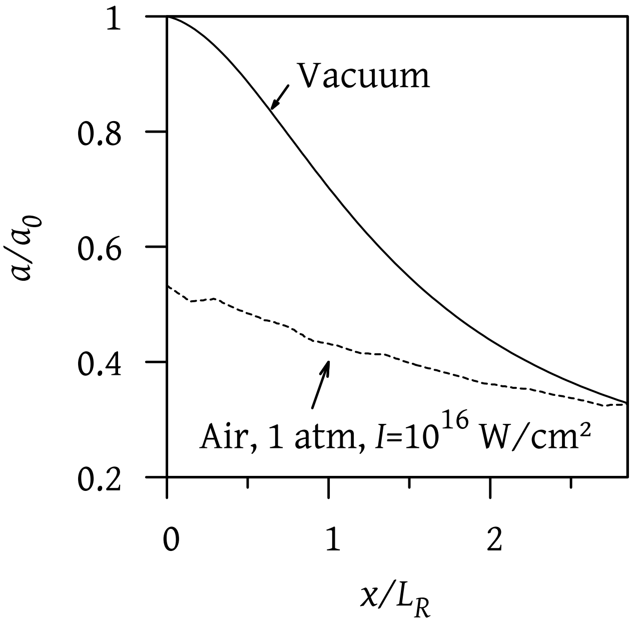


Figure 3.5: Focusability of 40 fs laser pulse with the maximal intensity $I_{max} = 10^{16}\,\mathrm{W/cm^2}$ in air according to 3D particle-in-cell simulation. ($L_R$: Rayleigh Length)

## 3.3 Two-color case

According to several experiments, the use of BBO crystal for the generation of second harmonics, that took ∼30 percent of the main pulse energy, drastically increased the output THz power[11–15]. Simulations for this case for two $p$-polarized laser pulses were performed.

Figure 3.6 show the laser field evolution. Compared to the single-color case (Fig. 3.1), field distribution is more complex due to the addition of $2\omega$ pulse; It has different dispersion, i.e., it moves faster than the $\omega$ wave. Also it has a different Rayleigh length at 17.6 mm, much longer than that of the $\omega$ wave (4.4 mm).

Figure 3.8 shows the electron density distribution and ion density. Compared to the single-color case (Fig. 3.3), The maximal electron density decreases slightly while the density modulation becomes more complicated, reflecting the nonlinear refraction process of two different frequency components.

The 2D spectrum of the radiation in plasma is shown in Fig. 3.9. We can see traces of various processes in ionized air: laser frequency up-shift, laser light scattering as the cylindrical waves, and THz radiation. Angular spectra can be obtained by post-processing the 2D spectrum. Figure 3.10 shows the angle dis-

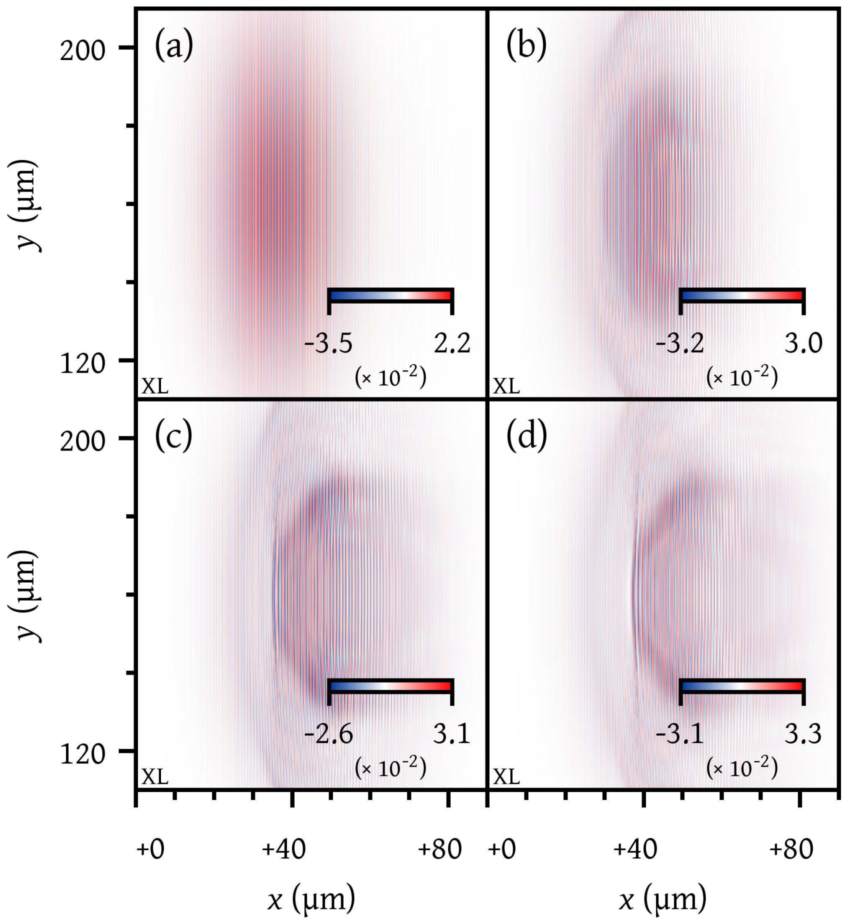


Figure 3.6: P-polarized electric fields over simulation area after 0.1, 1.1, 1.8, and 2.1 ps after propagation in the gas. The peak intensity of fundamental pulse is $I_\omega = 10^{16}\,\mathrm{W/cm^2}$, and $2\omega$ at $I_{2\omega} = 0.3 I_\omega$.

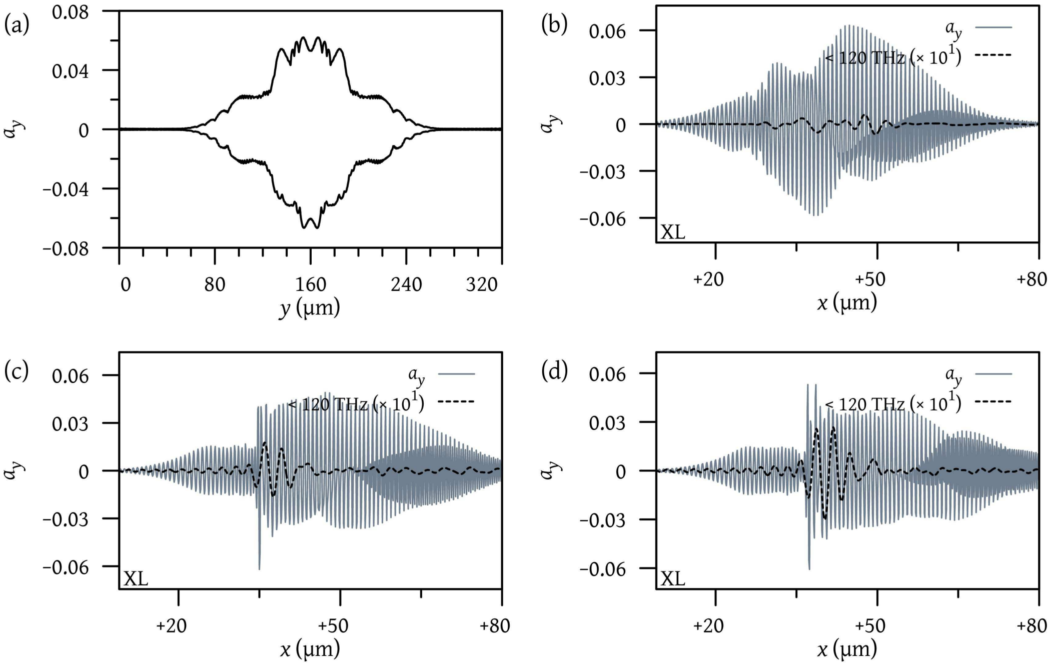


Figure 3.7: (a) transverse profile at 2.1 ps, and (b-d) profile along laser propagation axis x corresponding to (b), (c) and (d) in Fig. 3.6

tribution for representative THz frequencies is given. In addition to the strong forward emission, a strong radiation is observed at around 30°. Figure 3.11 shows the spectrum of THz radiation for several angles. A strong radiation power over 80 THz appears at 30 degree, compared to the single-color case (Fig. 3.4). In spite of almost same power for THz radiation at frequencies over 80 THz, the radiation power at lower frequencies is stronger than that of the single-color case. This also agrees with the experimental results[15].

### 3.3.1 Polarization dependence

Calculations that differ in the polarization of $\omega$ and $2\omega$ were performed. Figure 3.12 shows the angle distribution of THz power. THz generation efficiency is maximum when both the $\omega$ and $2\omega$ component have the same polarization that are *parallel* to that of the observing THz radiation (Fig. 3.12(d)). It is minimum when both the $\omega$ and $2\omega$ component have the same polarization that are *perpendicular* to that of the observing THz radiation (Fig. 3.12(b)). A relatively strong peak at 60° may be noteworthy, although further investigation is not done. For mixed polarizations (Fig. 3.12(a) and 3.12(c)), the efficiency is between those two cases. This polarization dependency of THz generation

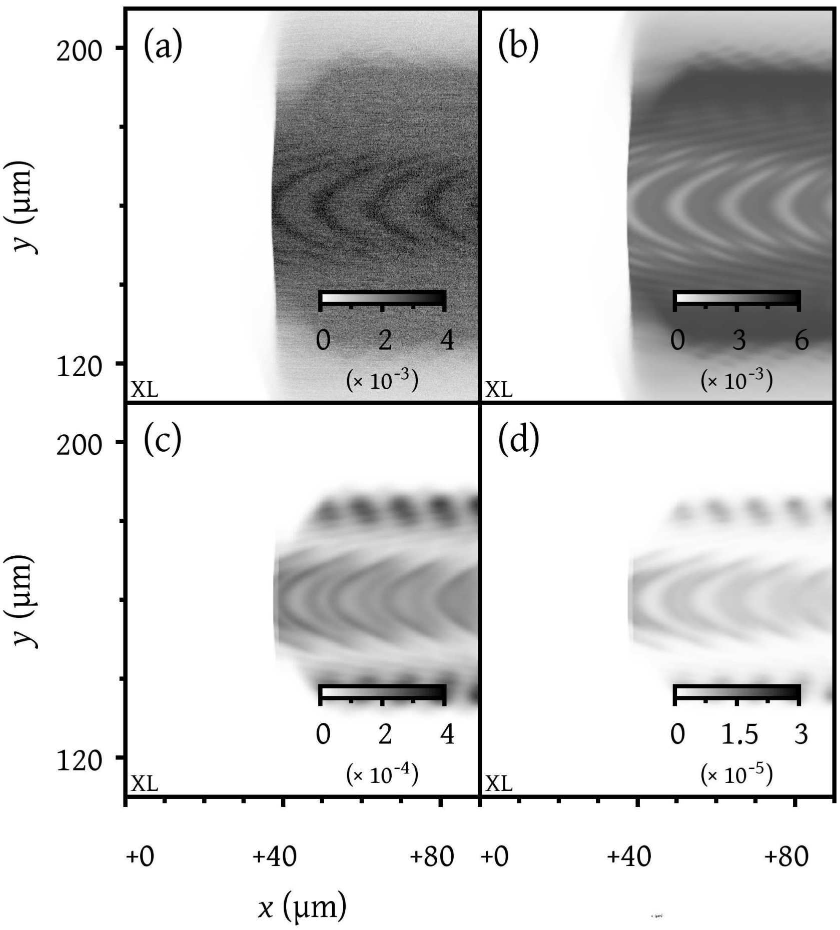


Figure 3.8: Electron and ion densities after a $p$-polarized two-color laser pulse propagated from right to left 2.1 ps in the 0.6 atm air. Peak intensity of $\omega$ is $I_{\omega} = 10^{16}\,\mathrm{W/cm^2}$ and $2\omega$ at $I_{2\omega} = 0.3 I_{\omega}$. (a) electron density, (b-d) density of 1+, 2+ and 3+ nitrogen ion, respectively.

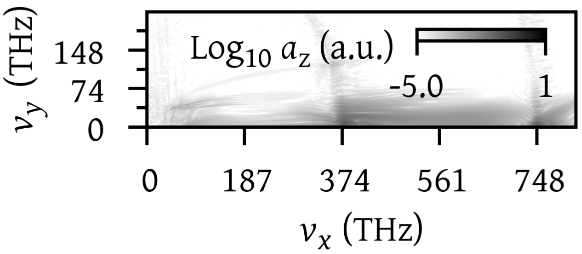


Figure 3.9: 2D spectrum of p-polarized radiation in plasma generated by the two-color laser pulse with the peak intensity of $\omega$ at $I_{\omega} = 10^{16}\,\mathrm{W/cm^2}$ and $2\omega$ at $I_{2\omega} = 0.3 I_{\omega}$.

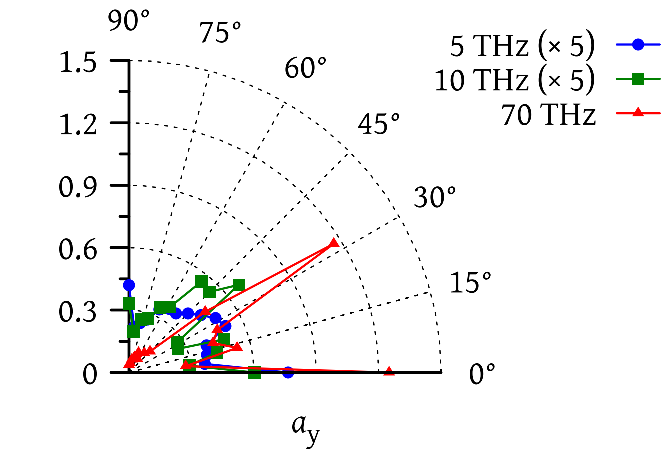


Figure 3.10: Angle distribution for radiation at 84 THz from plasma generated by the two-color laser pulse with the peak intensity of $\omega$ at $I_\omega = 10^{16}\,\mathrm{W/cm^2}$ and $2\omega$ at $I_{2\omega} = 0.3 I_\omega$.

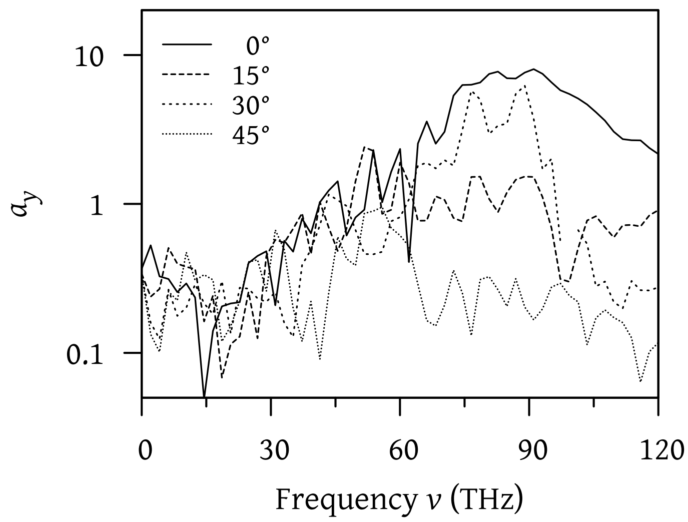


Figure 3.11: THz radiation spectrum along 0, 15, 30 and 45 degrees radiated from plasmas generated by the two-color laser pulse with the peak intensity of $\omega$ at $I_\omega = 10^{16}\,\mathrm{W/cm^2}$ and $2\omega$ at $I_{2\omega} = 0.3 I_\omega$.

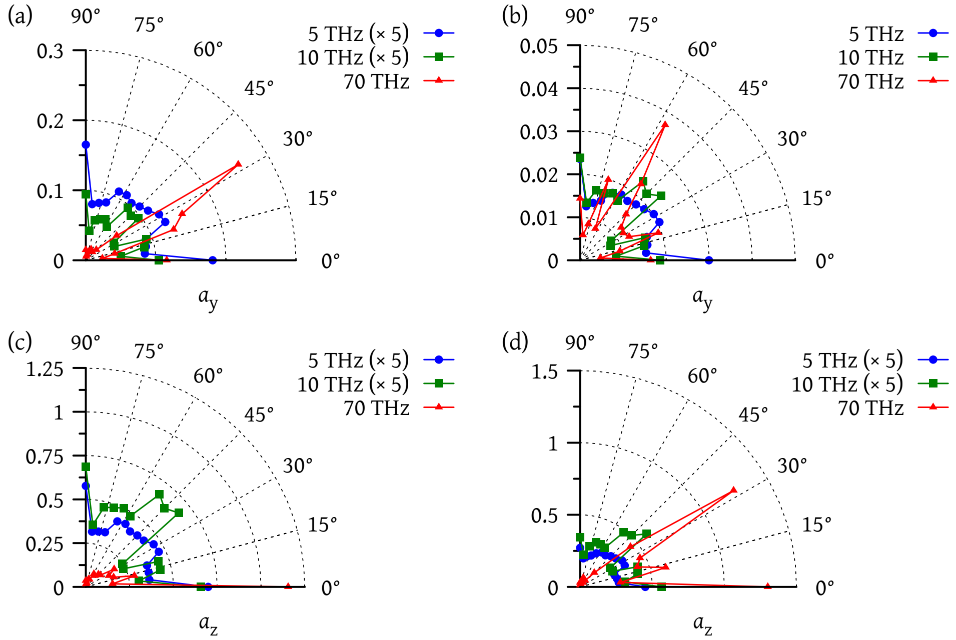


Figure 3.12: P-polarized THz power with (a) s-polarized $\omega$ and p-polarized $2\omega$ and (b) s-polarized $\omega$ and s-polarized $2\omega$. S-polarized THz power with (c) s-polarized $\omega$ and p-polarized $2\omega$ and (d) s-polarized $\omega$ and s-polarized $2\omega$. For all cases, the peak intensity of $\omega$ is $I_\omega = 10^{16}\,\mathrm{W/cm^2}$ and $2\omega$ at $I_{2\omega} = 0.3 I_\omega$

efficiency agrees well with ref. 13.

Also note that the strong THz radiation at 30° is observed only when the polarization of $2\omega$ is parallel to the observed THz radiation (Fig. 3.12(a) and 3.12(d)).

### 3.3.2 THz generation mechanism

To reveal the process of THz radiation formation, the temporal evolution of the laser field and THz radiation, plasma density and spectrum is compared in Fig. 3.13. The THz radiation is calculated by inverse Fourier transformation after applying short wavelength cut-off filter to the spectrum. We can see that THz radiation occur initially a little bit far from the ionization front. Then, the strong steepening of electron density is observed along with the THz power increase. Corresponding spectra exhibit the strong up-shift frequency components both for $\omega$ and $2\omega$ components. The peak THz frequency is found ~1.9 times the amount of frequency upshift at $\omega$ component. This correlation may prove that the beat-wave mechanism of THz radiation generation introduced in Sec. 2.4.

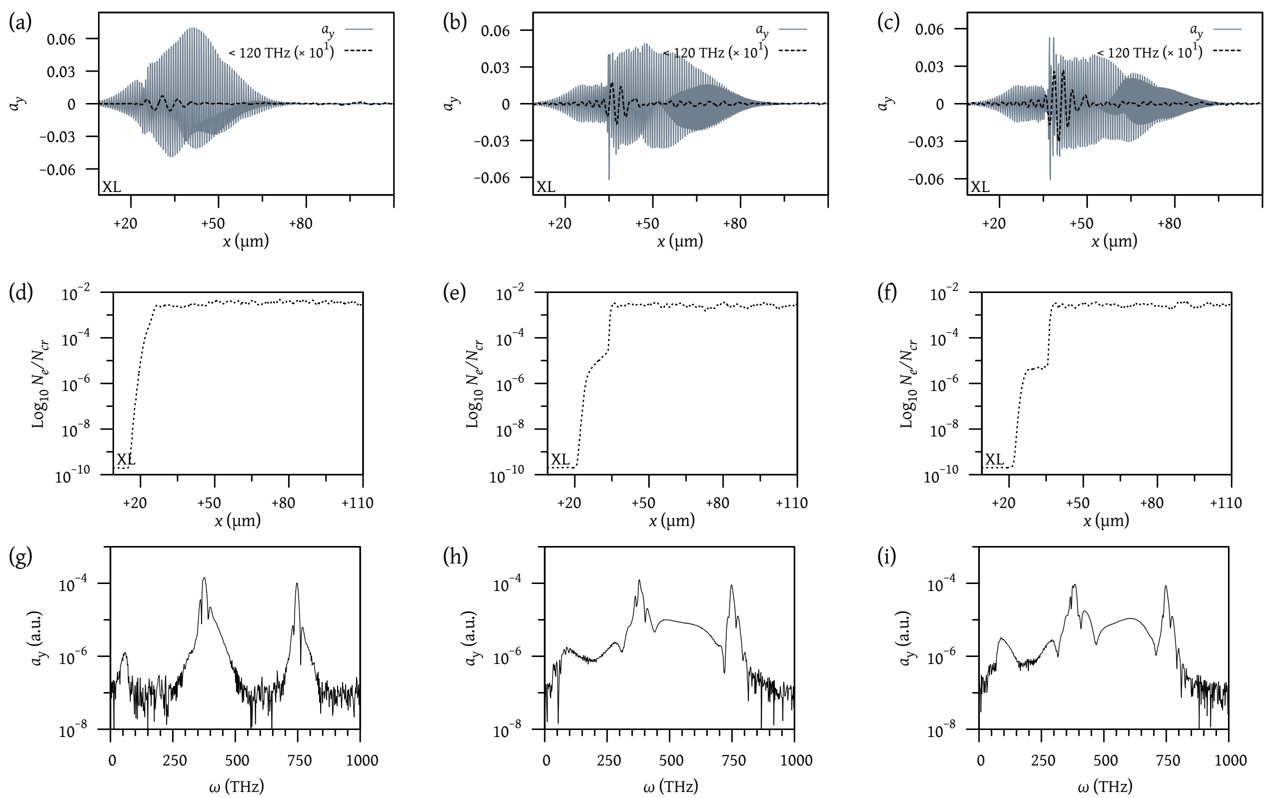


Figure 3.13: Temporal evolution of the (a-c) laser field and THz radiation, (d-f) the plasma density and (g-i) spectrum. The two-color laser pulse incident to the 0.6 atm air has the peak intensity of $\omega$ component at $I_\omega = 10^{16}\,\mathrm{W/cm^2}$ and $2\omega$ at $I_{2\omega} = 0.3 I_\omega$. Subfigures (a), (d), and (g) are taken at $t = 0.1$ ps. Subfigures (b), (e), and (h) are taken at $t = 1.1$ ps. Subfigures (c), (f), and (i) are taken at $t = 2.1$ ps.

### 3.3.3 THz power dependence on laser intensity

In order to find the THz power dependence on the laser intensity, calculation for two $p$-polarized pulses with lower intensities were performed. Note that all simulation in this section uses two-color laser pulse, and that the peak intensity of the $2\omega$ is $I_{2\omega} = 0.3 I_\omega$, if not written otherwise.

Figure 3.14 shows the density distribution in the 0.6 atm air after propagation of the two-color laser pulse with intensity $I_\omega = 10^{15}\,\mathrm{W/cm^2}$. The maximal density in this case is 20 times smaller than that of the run with the peak laser intensity of $I_\omega = 10^{16}\,\mathrm{W/cm^2}$. There are some density modulations; however, it is out of scope of calculation accuracy.

The spectrum of radiation for the laser intensity $I = 10^{14}$ and $I = 10^{15}\,\mathrm{W/cm^2}$ are shown in Fig. 3.15 and Fig. 3.16. For the former, we can see a weak THz emission in forward direction. The increase of the laser pulse intensity in the latter case results in much stronger power with a broad spectrum peaked at 10 THz. A strong emission centered around 40° occurs.

The dependence of power of THz radiation on the laser pulse intensity is presented in Fig. 3.17 and Fig. 3.18. According to Fig. 3.17, the angle distribution of THz power at lower frequencies, namely, 5 and 10 THz, becomes more uniform with increasing laser intensity. In Fig. 3.18, THz power is shown against the change in laser intensity for two propagation angle, namely, 0 and 30 degrees. In both cases, we can see two different slopes in the curves: up to the laser intensity $I \sim 10^{15}\,\mathrm{W/cm^2}$, the power growth is faster than linear, while beyond that intensity, the growth is slower than linear. An approximation function can be presented as following: $W \approx A\,(I/B)^\alpha\, e^{-B/I}$ with $\alpha \approx 0.7$, $A = 9 \times 10^{-3}$, and $B = (2-3) \times 10^{14}\,\mathrm{W/cm^2}$.

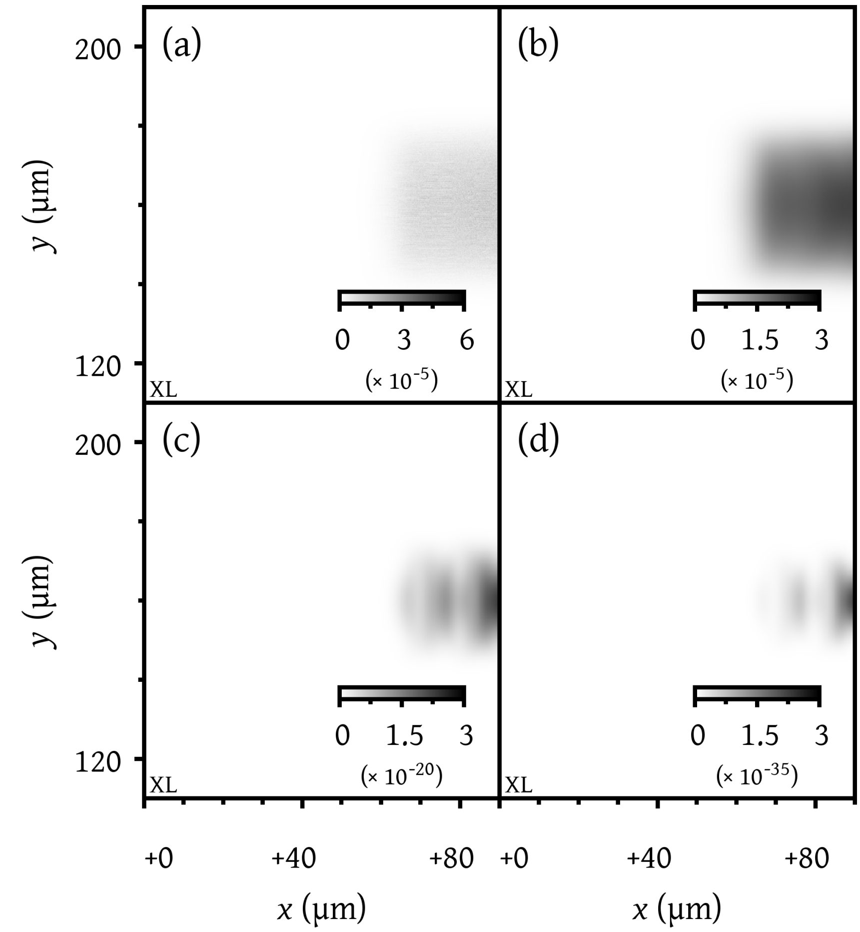


Figure 3.14: Electron and ion densities after propagation of a p-polarized two-color laser pulse in air with the peak intensity of $\omega$ at $I_\omega = 10^{15}\,\mathrm{W/cm^2}$ and $2\omega$ at $I_{2\omega} = 0.3 I_\omega$. (a) electron density, (b-d) density of 1+, 2+ and 3+ nitrogen ion, respectively.

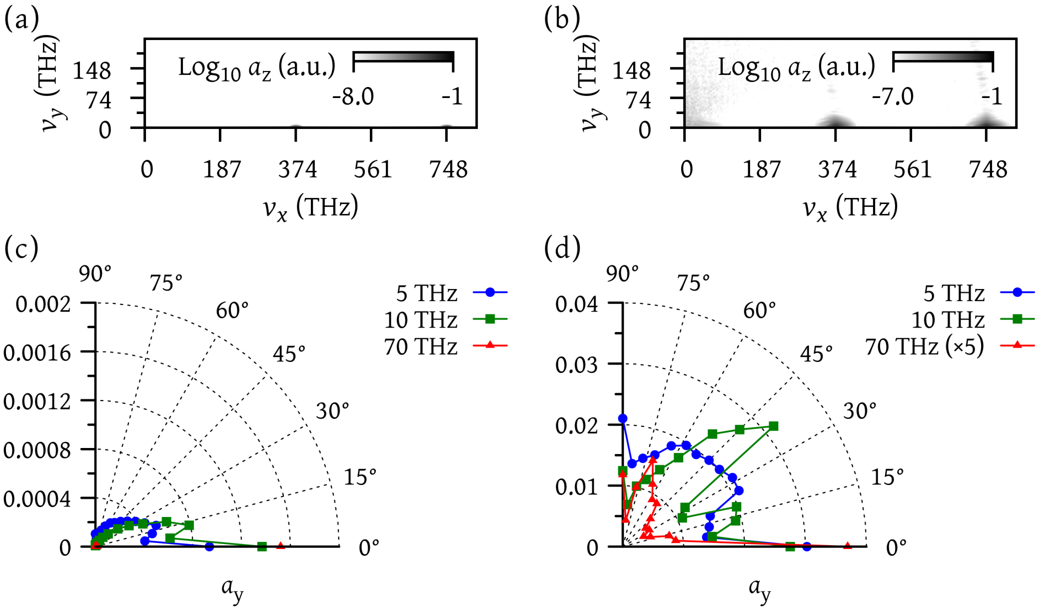


Figure 3.15: 2D spectrum of p-polarized radiation in plasma and its angular distribution peak laser intensity of $x$ at (a) and (c) $I_\omega = 10^{14}\,\mathrm{W/cm^2}$, and (b) and (d) $10^{15}\,\mathrm{W/cm^2}$ (right). The peak intensity of $2\omega$ is set to $0.3I_\omega$ for each case.

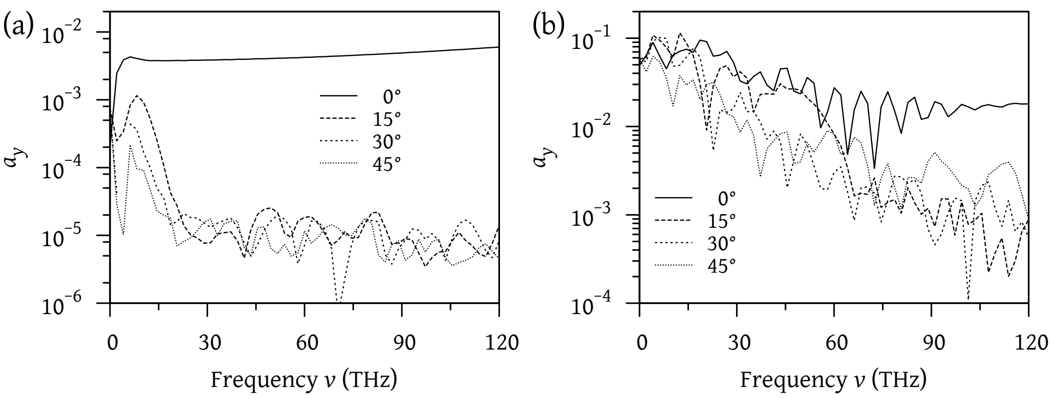


Figure 3.16: THz radiation spectrum along 0, 15, 30 and 45 degrees from plasma produced by a two-color laser pulse with the peak laser intensity of $\omega$ at (a) $I_\omega = 10^{14}\,\mathrm{W/cm^2}$ and (b) $10^{15}\,\mathrm{W/cm^2}$. The peak intensity of $2\omega$ is set to $0.3I_\omega$ for each case.

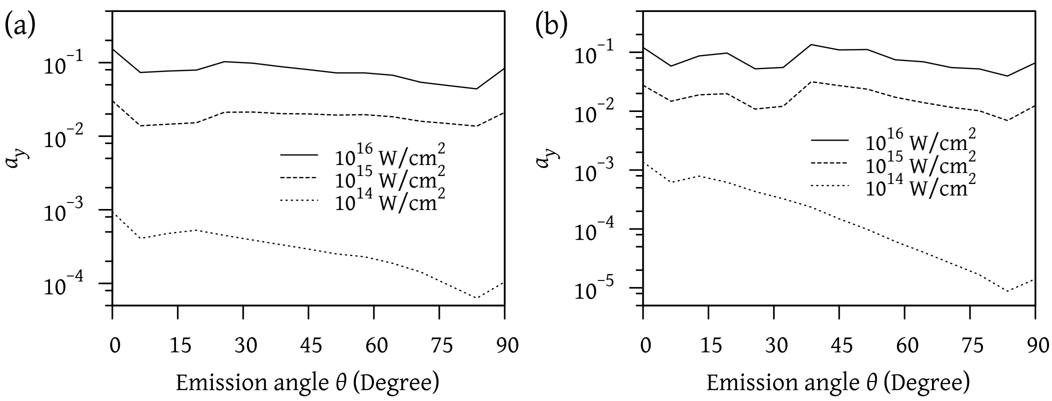


Figure 3.17: Dependence of power of THz radiation on the emission angle and laser pulse intensity at (a) 5 THz and (b) 10 THz.

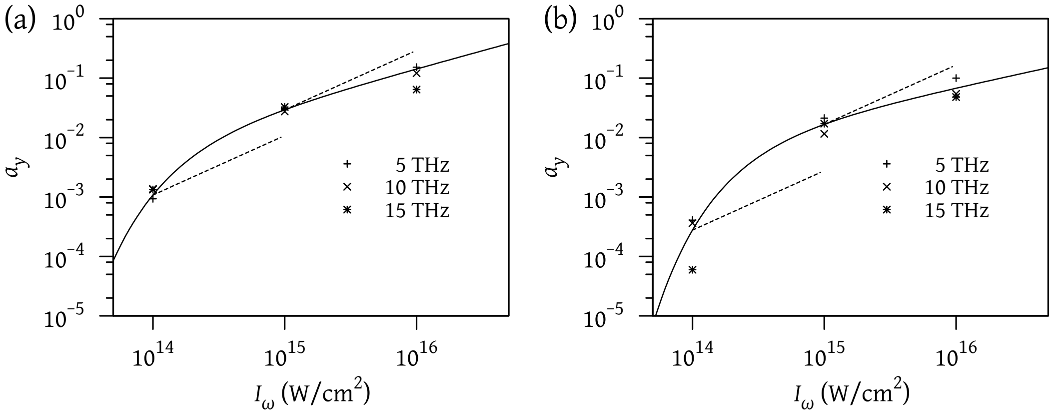


Figure 3.18: The dependence of power of THz radiation on the laser pulse intensity at the emission angles at (a) 0° and (b) 30°. Dashed lines indicate linear growth of THz power against the laser intensity.

## 3.4 Conclusion

In conclusion, the characteristics of THz radiation from air plasma induced by a single or two-color of femtosecond laser pulses have been studied numerically. In numerical simulations, a strong non-linear dependence of the THz power on the laser intensity is found. The power growth is faster than linear up to laser intensities on the order of $I \sim 10^{15}\,\mathrm{W/cm^2}$, then, the growth becomes slower than the linear; therefore, the conversion efficiency reaches its maximum at $I \sim 10^{15}\,\mathrm{W/cm^2}$.

The refraction has a strong effect on the THz radiation. The calculations have also revealed one of the main mechanisms of formation of THz radiation. The ionization current creates beat waves of which its characteristics depend on the ionization frequency up-shift. The beat wave arising between the incident two-color pulse and the up-shifted component is the sources of the current $\propto e^{i2[(\omega_+ - \omega_0)t]}$ responsible for the long wavelength radiation.

Strong ionization is found to modify the focus-ability of laser pulses. According to 3D simulation, refraction of laser pulses on the induced plasma increases the minimal pulse waist. The intensity of laser pulse with a maximum at $10^{16}\,\mathrm{W/cm^2}$ at the focus point has been reduced almost four times due to the plasma.

The angle distributions and spectra of THz radiation are also very sensitive to intensity of laser pulses. At the lowest laser intensity the straightforward emission is dominant; the plasma density is lower and THz radiation under 5 THz frequencies can propagate in pre-ionized air. As the laser intensity increases, the plasma density rises, resulting in stronger diffraction of THz radiation, and a strong emission at angle near 30°. At laser intensity $I \sim 10^{16}\,\mathrm{W/cm^2}$, the lower wavelength radiation, $< 10$ THz, is emitted almost uniformly. The maximum frequency of THz radiation follows the plasma frequency which increases with the laser intensity.

Note that the strong diffraction of THz radiation and its broadband spectrum were the motivation for the study of THz waveguide described in Chp. 5.

## References

[1] W. Wood, C. Siders, and M. Downer, "Femtosecond growth dynamics of an underdense ionization front measured by spectral blueshifting," IEEE Transactions on Plasma Science **21**, 20 (1993).

[2] E. Esarey, P. Sprangle, J. Krall, and A. Ting, "Self-focusing and guiding of

short laser pulses in ionizing gases and plasmas," IEEE Journal of Quantum Electronics **33**, 1879 (1997).

[3] C. S. Liu and V. K. Tripathi, "Laser frequency upshift, self-defocusing, and ring formation in tunnel ionizing gases and plasmas," Physics of Plasmas **7**, 4360 (2000).

[4] M. Lampe, E. Ott, and J. H. Walker, "Interaction of electromagnetic waves with a moving ionization front," Physics of Fluids **21**, 42 (1978).

[5] S. Wilks, J. Dawson, W. Mori, T. Katsouleas, and M. Jones, "Photon accelerator," Physical Review Letters **62**, 2600 (1989).

[6] W. B. Mori, "Generation of tunable radiation using an underdense ionization front," Physical Review A **44**, 5118 (1991).

[7] A. Zhidkov, T. Esirkepov, T. Fujii, K. Nemoto, J. Koga, and S. V. Bulanov, "Characteristics of Light Reflected from a Dense Ionization Wave with a Tunable Velocity," Physical Review Letters **103**, 215003 (2009).

[8] A. Zhidkov, J. Koga, T. Esirkepov, T. Hosokai, M. Uesaka, and T. Tajima, "Optical-field-ionization effects on the propagation of an ultraintense laser pulse in high- Z gas jets," Physical Review E **69**, 066408 (2004).

[9] I. Babushkin, W. Kuehn, C. Köhler, S. Skupin, L. Bergé, K. Reimann, M. Woerner, J. Herrmann, and T. Elsaesser, "Ultrafast Spatiotemporal Dynamics of Terahertz Generation by Ionizing Two-Color Femtosecond Pulses in Gases," Physical Review Letters **105**, 053903 (2010).

[10] A. Zhidkov, J. Koga, K. Kinoshita, and M. Uesaka, "Effect of self-injection on ultraintense laser wake-field acceleration," Physical Review E **69**, 035401 (2004).

[11] D. J. Cook and R. M. Hochstrasser, "Intense terahertz pulses by four-wave rectification in air." Optics letters **25**, 1210 (2000).

[12] T. Bartel, P. Gaal, K. Reimann, M. Woerner, and T. Elsaesser, "Generation of single-cycle THz transients with high electric-field amplitudes." Optics Letters **30**, 2805 (2005).

[13] X. Xie, J. Dai, and X.-C. Zhang, "Coherent Control of THz Wave Generation in Ambient Air," Physical Review Letters **96**, 075005 (2006).

[14] K.-Y. Kim, J. H. Glownia, A. J. Taylor, and G. Rodriguez, "Terahertz emission from ultrafast ionizing air in symmetry-broken laser fields." Optics Express **15**, 4577 (2007).

[15] K. Y. Kim, A. J. Taylor, J. H. Glownia, and G. Rodriguez, "Coherent control of terahertz supercontinuum generation in ultrafast laser–gas interactions," Nature Photonics **2**, 605 (2008).

# Chapter 4

# Amplification of THz wave in Plasma

## 4.1 Introduction

This chapter describes experimental works on the two-color laser scheme for THz generation. In addition to the examination of the photocurrent theory by experiments, preparatory experiments, such as plasma density measurement by longitudinal diffraction method, and the calibration of THz power detectors, are described. They are necessary for a precise estimation of THz source based on laser-plasma interaction.

With those methods established, an experimental result could be observed that may suggest the possibility of THz amplification in plasma whose length is changed by use of two beams of two-color laser pulse.

In the experiment, an order of enhancement in THz power is observed. Such an enhancement may be attributed to formation of an asymmetric plasma profile in which the plasma density increases steeply in the head and decreases gradually in the tail. A one-dimensional model has been solved with and without accounting for amplification. The former shows better match with the experimental results than the latter, which implies the possibility of the amplification of THz wave in the plasma.

The experiment presented in this section was performed with an original intention of finding the dependence of THz wave intensity on the spatial plasma profile, e.g., length, generated by two-color fs lasers. The topic has been of interest since the plasma itself is the source of THz wave. Current theories, including the photocurrent model (Sec. 2.3) and four-wave mixing model, predict oscillating THz yield with a period given by coherence length $L_{\mathrm{hp}}$ (page. 14).

The length of plasma generated by laser irradiation on air can be many times the Rayleigh length. This formation of plasma channel can be intuitively explained by the balance between self-focusing and diffraction by plasma [1,2].

So far, experimentally, the relation has been surveyed with a plasma channel fixed in length, by sliding a pin hole along the longitudinal axis of plasma filament, which blocks the THz wave while passing the laser pulse intact. This method can show the contribution from each part of the plasma filament.

For a plasma filament shorter than $L_{\mathrm{hp}}$, it is found that, with a laser intensity of $\omega$ at $2.8 \times 10^{14}$ W/cm$^2$ and a power of 2.9 GW, the entire plasma contributes positively to the THz generation [3]. In other words, the THz yield increases with the increase of plasma length. For a plasma filaments between $L_{\mathrm{hp}}$ and $2L_{\mathrm{hp}}$, negative contribution from the later half of the filament is observed [4].

It should be note that the longest plasma filament in the work presented in this dissertation was shorter than length $L_{\mathrm{hp}}$. It would be interesting to see any change in the exponential growth of THz power observed in the present work for longer plasma filament.

Also note that a similar experiment is reported in ref. 5, but the mechanism for the enhancement has not been discussed and the electron density measurement is lacking.

Before the experiment and the discussion, I would like to show some more traditional approach for the amplification of THz wave in the next section.

## 4.2 Previous research on amplification

There are several theoretical, and experimental studies regarding amplification of terahertz wave. However, to the author's knowledge, there is no experimental work in the literature so far that have proved an amplification model or showed an enhancement of THz field amplitude more than one order.

### 4.2.1 Rotational band excitement

Alignment of rotational band of the target gas has been studied theoretically and experimentally. However, there is a gap between those two approaches; the theoretical study supposed using hydrogen cyanide (HCN) gas which is a dipolar moculelar gas. In experimental studies, however, used non-polar gases such as $N_2$ or $O_2$. The different in the choice of gas may attributed to the difficulty in handling the toxic HCN gas, and to the fact that those experimental studies were performed in the frame of air-plasma experiments. It would be interesting to fill the gap between theory and experiment using non-toxic, dipolar mocular gas such as nitrous oxide ($N_2O$), a.k.a., laughing gas. The gap is, however, yet to be addressed, and is not addressed in this dissertation.

Theoretically, population inversion in rotational lines of HCN gas at the pressure lower than 0.02 atm and the temperature of 50 K or 310 K, driven by a single laser pulse of $1.5 \times 10^{13}$ W/cm$^2$, 100 fs, 800 nm, or a multiple train of them, is studied numerically for the amplification of THz wave in ref. 6. It is found that population inversion is more efficiently excited at lower temperature. Note that the ionization effect is ignored in the work. Still, if the ionization ratio is low enough such that the molecule density is much higher than the plasma density, the model may hold true.

Experimentally, the effect of molecular alignment of ionizing *air* at room temperature is experimentally studied in ref. 7 and 8. They do not, however, focus on the effect of amplification, but on the change in the refractive index that leads to the change in the nonlinearity $\chi^{(3)}$. The change in the THz amplitude were less than 20 percent.

### 4.2.2 Multiple stage THz generation

There are few experimental studies on the amplification of THz wave by multiple stage THz generation[9,10]. To explain this scheme, let us denote the number of THz generation stage by $N$. At the initial stage ($N = 1$), THz wave is generated by the usual two-color scheme. In the following stage, the THz wave generated in the preceding stage ($N - 1$, where $N = 2, 3, \ldots$) is superimposed to a two-color laser pulse to generate new plasma filament and $N$-th THz wave with enhanced efficiency. The $N$-th THz wave in turn is superimposed to another two-color laser pulse to enhance the generation of the ($N + 1$)-th THz wave.

In ref. 9, two-color laser pulse is focused three times by different off-axis parabolic mirrors. THz wave generated from different plasma filament is measured by electro-optic amplitude modulation method with a balanced detector pair. The THz wave generated from each plasma increase by 20 to 35 percent as it is being superimposed.

In another experiment, only the THz wave is selectively seeded into the second plasma, yielding about 65 percent of enhancement compared to the case without the second plasma[10]. Four-wave-mixing parametric processes involving $2\omega$ pulse have been attributed for the enhancement.

The small enhancement may be attributed to the low coupling efficiency between the THz wave and plasma filaments. It is difficult to focus the long-wavelength light such as THz wave tightly to the lateral dimension of the plasma. The diffraction limit* of conventional optics indicates that the beam waist is roughly on the order of wavelength of the light. For example, the waist of the THz seed pulse was 400 µm in the experiment in ref. 9. It is about three times the typical diameter of plasma filament in ambient air, which is around 150 µm, determined by the balance between Kerr focusing and plasma defocusing (See page 1662 at ref. 2).

In order to achieve high coupling between THz wave and plasma filament, measuring THz beam profile that includes its diameter and pointing center during the alignment of optics would be helpful. Current microbolometer technology may be used for that purpose**. If the THz pulse is sufficiently strong, the probe-beam-free THz detection method in Appx. B may be applied in the future after enhancement of detection sensitivity and their two dimensional integration.

## 4.3 Two-color laser scheme experiment

Experiments for verification of photocurrent model is performed with P-cube laser system at Osaka University. Fig. 4.1 shows the setup.

The laser system was adjusted to deliver pulses with energy of 20 to 50 mJ at 10 Hz pulse repetition rate. Its pulse duration inside vacuum chamber was estimated at 50 fs (FWHM) by an intensity autocorrelator assuming Gaussian pulse shape (note that $\Delta\tau_{\mathrm{AC}}^{\mathrm{FWHM}} = \sqrt{2}\Delta\tau_{\mathrm{pulse}}^{\mathrm{FWHM}}$). Since the experiment was performed in atmosphere, and group velocity dispersions in the air and mirrors

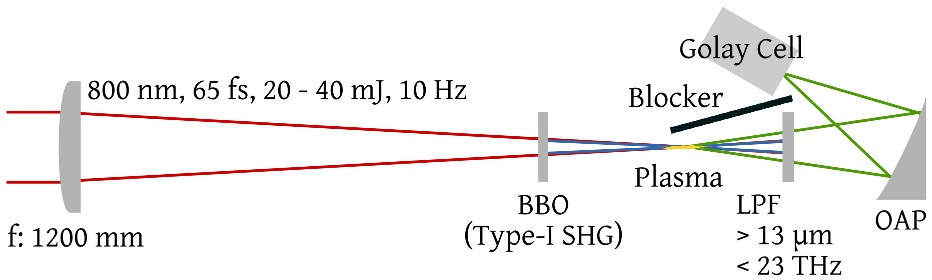


Figure 4.1: Experimental setup for terahertz generation by two-color laser pulse.

*It is well known that assuming a uniform beam profile incident on a focusing lens, the diameter of the first ring of the Airy disk, which contains 83.8 percent of beam power, is given by $2.44\lambda N$ where $\lambda$ is the wavelength, and $N = f/D$ is the F-number with $f$ the focal length and $D$ the aperture diameter[11].

**The author had tried a uncooled THz CCD manufactured by a Japanese company in 2013. At that time, external trigger was not equipped, making it useless for pulsed THz generation.

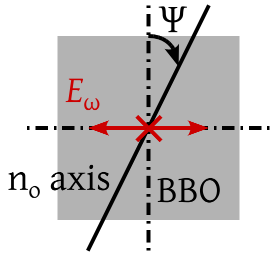


Figure 4.2: Rotation of the BBO crystal. The fundamental laser pulse is incident normal to the crystal. Ordinary axis is found by monitoring the angle at which blue generation becomes the strongest.

made the pulse duration longer to 65 fs. The diameter of pulse was 60 mm. A 4" plano-convex lens with a focal length of 1200 mm ($f/20$) was used for focusing instead of an off axis parabolic mirror (OAP). The focused diameter was not measured, but 120 µm is a reasonable guess from past experiences, leading to the range of focused intensity between $2.7 \times 10^{15}$ and $5.4 \times 10^{15}$ W/cm$^2$.

Incident $\omega$ pulses were partly frequency-converted to $2\omega$ during its propagating in the $\beta$-$BaB_2O_4$ (BBO) crystal. A low pass filter (LPF) behind the plasma filament blocks the residual laser pulses at $\omega$ and $2\omega$, while passing the THz pulse generated from the plasma. THz wave was focused by an OAP with a focal length of 150 mm to the Golay cell. It has a 2 mm diameter window and its output is a voltage signal proportional to the power of radiation incident on its window. Experimental results in this experiment is used for calibration of the detectors in Sec. 4.4.2.

### 4.3.1 Intensity and polarization of second harmonic generation

Second harmonic pulse at $2\omega$ (400 nm, blue) is obtained by type-$I$ second harmonic generation (SHG) since it is outside the tunable range of Titanium-doped sapphire (670-1200 nm)[12]. The BBO crystal is cut so that an angular phase matching is satisfied between the fundamental pulse $\omega$ and its second harmonic $2\omega$, with their polarization perpendicular to each other: the former $\omega$ on the ordinary axis of the crystal and the latter $2\omega$, on the extraordinary axis. As can be deduced from the analytical study in the previous Sec. 2.3, for efficient THz pulse generation, both $\omega$ and $2\omega$ laser electric field should have the identical polarization. Here, BBO crystal is simply rotated as shown in Fig. 4.2 so that part of the $2\omega$ light have the polarization identical to the $\omega$ light.

With the orientation of the crystal as shown in Fig. 4.2, the complex electric field of the $\omega$ light on the ordinary and extraordinary axis is given by

$$\begin{cases} F_{1,o} = F_1 \sin\Psi & (\mathrm{n_0\ axis}) \\ F_{1,e} = F_1 \cos\Psi & (\mathrm{n}_e\ \mathrm{axis}) \end{cases} \tag{4.1}$$

while those of the $2\omega$ light is expressed as

$$\begin{cases} F_{2,o} = 0 & (\mathrm{n_0\ axis}) \\ F_{2,e} = \dfrac{\omega d_{\mathrm{eff}}}{c n_2 \Delta k} (F_1 \sin\Psi)^2 \left(1 - e^{-i\Delta kL}\right) & (\mathrm{n}_e\ \mathrm{axis}) \end{cases} \tag{4.2}$$

Using the relation between the complex electric field and the intensity of a monochromatic electromagnetic wave,

$$I = \frac{n}{2\mu_0 c} |F|^2 \tag{4.3}$$

where $n$ is the refractive index, $\mu_0$ is the vacuum permeability, $c$ is the speed of light, and the definition of angular frequency $\omega = 2\pi c/\lambda$, the intensity of the second harmonic can be arranged to

$$I_{2,e} = \frac{2\pi^2 d_{\mathrm{eff}}^2}{\mu_0 c n_2} \left(\frac{L}{\lambda}\right)^2 F_1^2 \sin^2\Psi \,\mathrm{sinc}\left(\frac{\Delta kL}{2}\right) \tag{4.4}$$

and it is evident the second harmonic is proportional to the quadratic power of the sine of the rotation angle $\Psi$. It is necessary to decompose the complex field of the blue into $x$ and $y$ axis. The component whose polarization is parallel to the red is proportional to $\cos\Psi$. Therefore, the intensity of the blue that is directly relevant to the terahertz generation is proportional to

$$I_{2\omega,e,x} \propto \sin^2\Psi \cos\Psi \tag{4.5}$$

### 4.3.2 Relative phase between $\omega$ and $2\omega$

Relative phase between $\omega$ and $2\omega$ pulses can be adjusted by changing the propagation distance between them in the air. The dispersion relation (frequency dependent refractive index) of air under 25 °C, 1 atm, and humidity of 50 per-

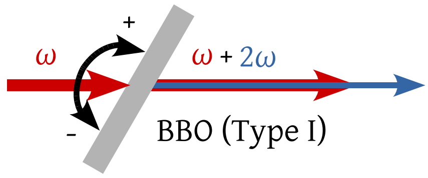


Figure 4.3: Adjustment of incident angle to dephase the phase matching condition for second harmonic generation, thus to reduce the intensity of blue pulse, without affecting its polarization.

cent is represented by[13]

$$n - 1 = \frac{C_2}{C_1 - \lambda^{-2}} + \frac{C_4}{C_3 - \lambda^{-2}} \tag{4.6}$$
$$C_1 = 238.02, \quad C_2 = 5.79 \times 10^{-2}$$
$$C_3 = 57.36, \quad C_4 = 1.68 \times 10^{-3}$$

Specifically, for fundamental ($\omega$) pulse with a wavelength of 800 nm, $n_\omega$ = 1.000275048, and its $2\omega$, $n_{2\omega}$ = 1.000282762. The distance for the relative phase between $\omega$ and $2\omega$ to change by $\pi/2$ is estimated at 13 mm from

$$\theta = 2\omega\,(n_\omega - n_{2\omega})\,d/c = 4\pi\frac{d}{\lambda}\,(n_\omega - n_{2\omega}) \tag{4.7}$$

where $c$ is the speed of light in vacuum, $d$ is the propagation distance, $\lambda$ the wavelength of fundamental wave.

### 4.3.3 Dependence on the intensity of second harmonic

When the incident angle of the fundamental pulse on the BBO surface is changed as in Fig. 4.3, the conversion efficiency from $\omega$ to $2\omega$ decreases, resulting in decrease in THz yield, as shown in Fig. 4.4. It is evident that THz intensity becomes strong as the intensity of $2\omega$ increases.

Figure 4.5 shows the THz intensity against the angle between the ordinary axis of BBO and the polarization of $\omega$ pulse. The orientation of the crystal is shown in Fig. 4.2. Since the phase matching for SHG can only be satisfied between incident wave on ordinary axis and second harmonic on extraordinary axis, the relation between $\Psi$ and THz intensity can be derived as Eq. (4.5) and it agrees well with the experiment results.

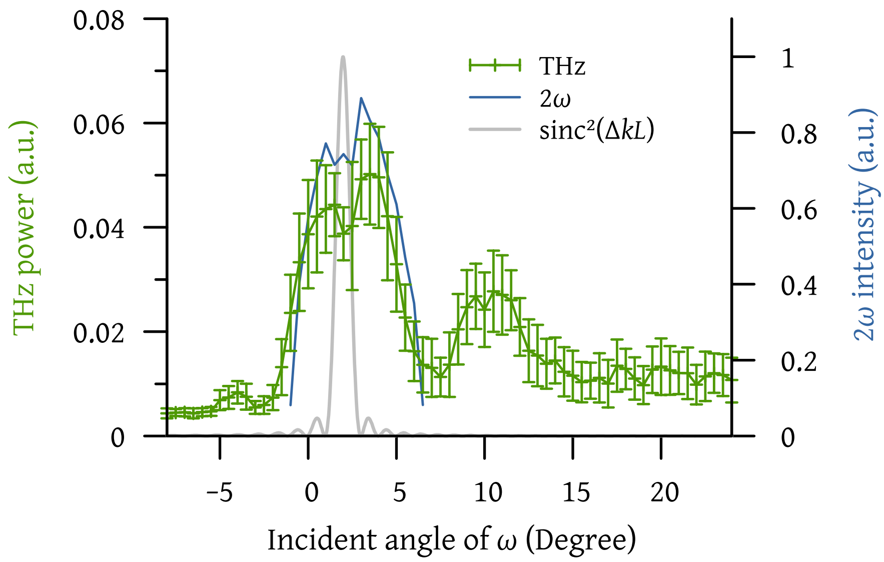


Figure 4.4: THz intensity as the incident angle of the fundamental laser pulse is dephased from the phase matching condition

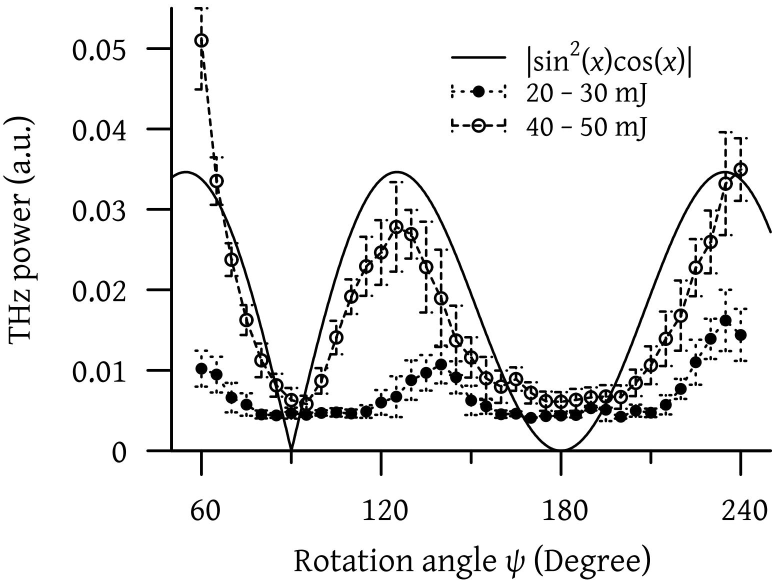


Figure 4.5: THz intensity measured as the angle between the ordinary axis of BBO crystal and the polarization of the fundamental laser pulse, changing the intensity and the polarization of the second harmonic simultaneously.

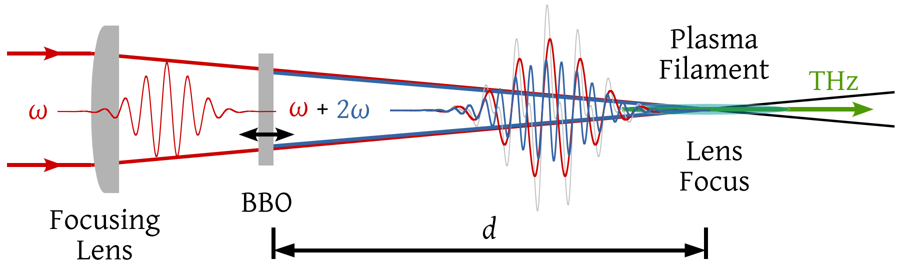


Figure 4.6: Distance from the rear surface of the BBO to the laser focal spot is changed to control the relative phase between the fundamental and the second harmonic electric field.

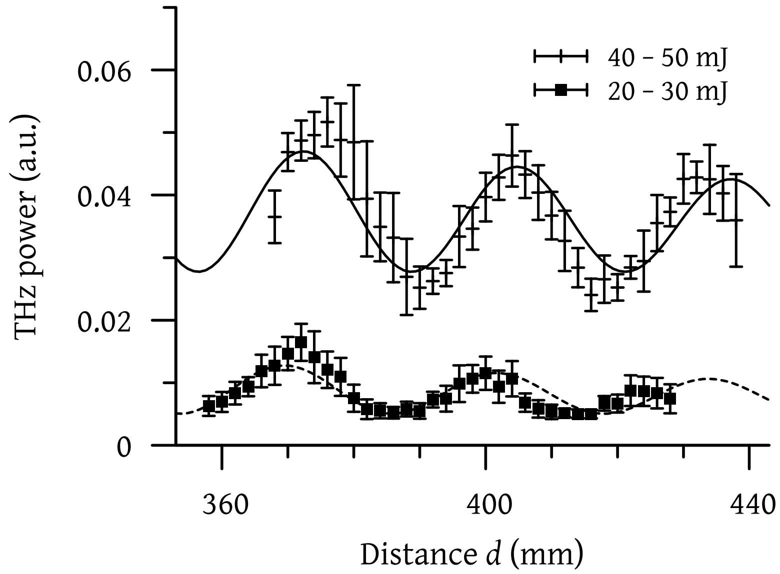


Figure 4.7: THz intensity vs the phase difference between red and pulse pulse.

### 4.3.4 On relative phase between $\omega$ and $2\omega$

As illustrated in the setup Fig. 4.6, THz intensity is measured while changing the distance from the surface of BBO crystal to the plasma which is assumed to be at the focal point of the focusing lens. Figure 4.7 shows the THz intensity against the distance $d$ which is proportional to the sine square of the relative phase $\theta$ between $\omega$ and $2\omega$, as predicted by Eq. (2.21). Its period also agrees well with the value predicted by Eq. (4.7). Solid line stands for numerical fitting of experiment results to $a + (bx)^{-c}$ by the mean-least-maximum method.

There is a shift toward the focusing lens in the position where the intensity of THz yield is maximum as the energy of the $\omega$ pulse increases. This shift can be attributed to the shift of the focus spot, as the threshold for ionization is reached earlier with higher laser energy, effectively changing the distance $d$.

## 4.4 Preparatory experiments

As a preparation for amplification experiment, the plasma density measurement experiment and calibration of THz power detector have been performed.

### 4.4.1 Density Measurement Method for Low Density Plasma

Measurement of electron density is usually performed with interferometry. For low electron density, however, the shift change is very small and alternative methods using diffraction has been proposed[14,15]. In this section, the method and the calibration used in this dissertation are described.

The method requires calibrating the diffraction of the probe beam with the electron density estimated by the fluorescence of the nitrogen molecule in the air. Figure 4.8 shows the schematic of the calibration. Figure 4.9 shows the actual setup. Note that the plasma dimension is measured only once and it is assumed that the plasma length does not change much depending on the shot-to-shot power variation of the laser. The opening diameter of the aperture $AP$ is changed to generate plasmas of different electron density by limiting the laser energy for the plasma generation.

Figure 4.10 shows the typical image of the CCDs taken with the setup in Fig. 4.9. From the diffracted probe beam profile, as shown in Fig. 4.10(a), we can obtain the electron density and the N fluorescence by finding the best fit for the measured diffraction pattern with the equation that has an electron density term inside:

$$I(r) = -A\exp\left(-b_0 r^2\right)\frac{J_1\left(2Kr_c r\right)}{2Kr_c r}\cos\left[b_1 r^2 - \frac{\phi(r)}{2}\right]\sin\left[\frac{\phi(r)}{2}\right] + Y_{offset} \tag{4.8}$$

with

$$\begin{cases} K &= \dfrac{\pi}{\lambda d_0} \\ b_0 &= \dfrac{K^2}{a^2+K^2} \approx a \\ b_1 &= \dfrac{K^3}{a^2+K^2} \approx K \\ \phi(r) &= \dfrac{\pi}{\lambda n_c}\displaystyle\int_0^L n_e(r,z)\,dz = 2\pi\frac{L}{\lambda}\frac{n_e}{n_c} \end{cases} \tag{4.9}$$

where $J_1(r)$ is the first-order Bessel function, $r_c$ radius of plasma filament, $L$ plasma length, $n_c$ plasma electron density, and $n_c$ the critical density for probe beam[15].

From the two-dimensional spectrum, of which typical profile is shown in Fig. 4.10(b), we obtain the fluorescence intensity corresponding to each aperture opening, as shown in Fig. 4.11. The specific wavelength used is 392 nm from the first negative band system of $N_2^+$ $(B^2\Sigma_u^+–X^2\Sigma_g^+)$[16].

The dependency of the fluorescence intensity on the electron density is summarized in Table 4.1. It is linear:

$$N_e\,[\mathrm{cm}^{-3}] = 6.96 \times 10^{15} I_{\mathrm{fl.}} - 6.65 \times 10^{13} \tag{4.10}$$

as shown in Fig. 4.12 along with measurements.

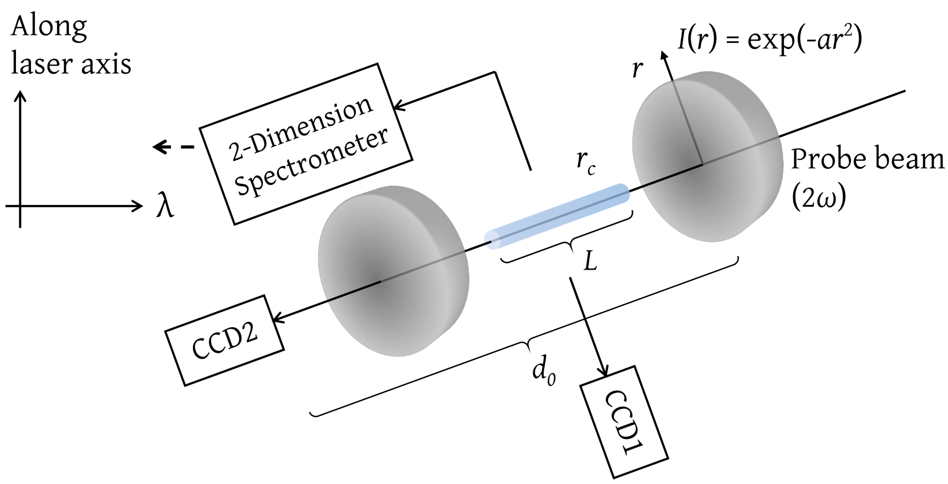


Figure 4.8: Setup for calibration of the longitudinal diffraction method. CCD1 measured the plasma dimension. CCD2 measures the diffraction pattern of the incident probe beam. The 2-dimension spectrometer measured the fluorescence of nitrogen molecule along the laser propagation axis which is identical to the plasma profile.

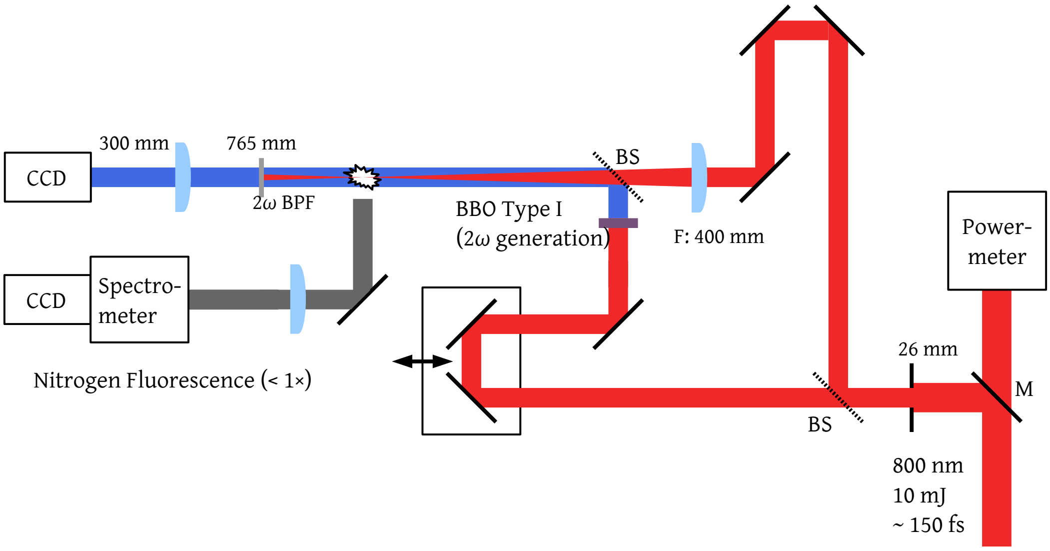


Figure 4.9: Experimental setup for calibration of the diffraction method

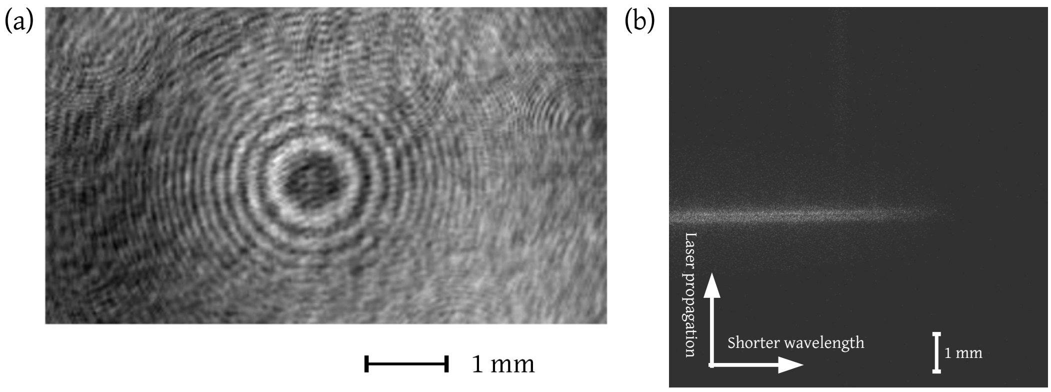


Figure 4.10: Typical CCD images taken with the aperture open at 26 mm. (a) Diffraction profile of the probe beam. (b) Two-dimensional spectrum covering the fluorescence spectrum of the Nitrogen molecule.

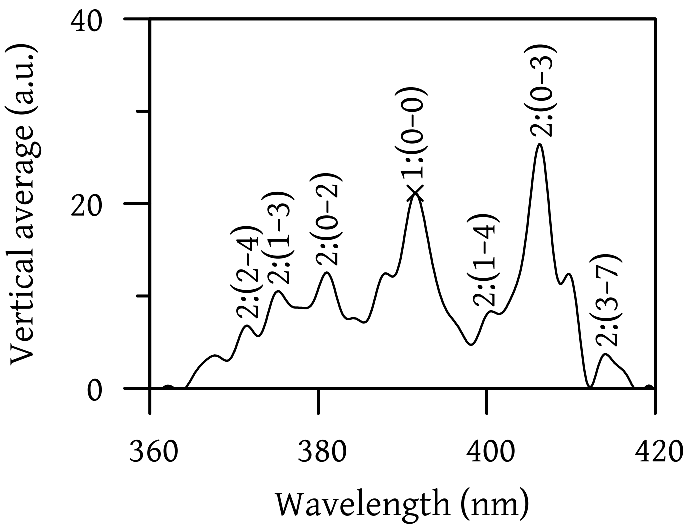


Figure 4.11: Fluorescence spectrum with the aperture open at 26 mm. The lines marked by 1 indicate the first negative band system of $N_2^+$ ($B^2\Sigma_u^+$–$X^2\Sigma_g^+$) and those marked by 2 indicate the second positive band system of $N_2^+$ ($C^3\Pi_u$–$B^3\Pi_g$) respectively. Transition from the upper vibrational level $\nu$ to lower one $\nu'$ is indicated by ($\nu$–$\nu'$)[16].

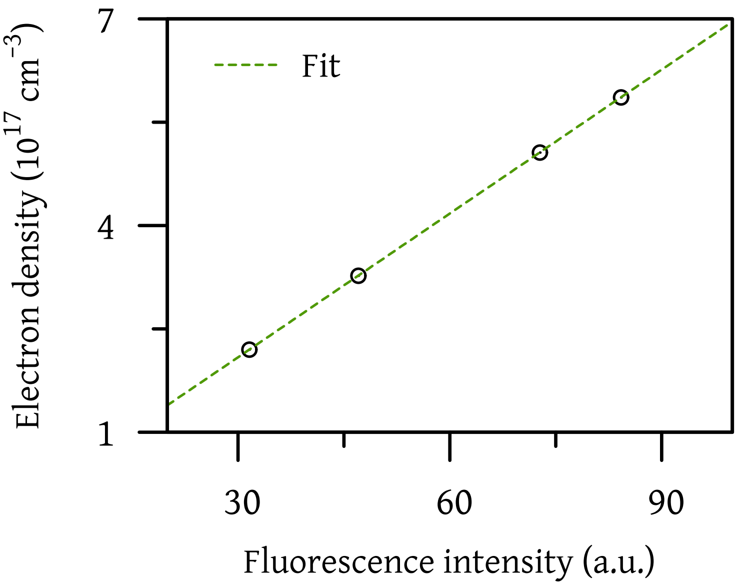


Figure 4.12: Linear relation between the fluorescence intensity and the electron density

Table 4.1: Electron density vs fluorescence intensity

| Aperture (mm) | Pump laser energy (mJ) | Fluorescence intensity (a.u.) | Electron density ($cm^{-3}$) |
|---|---|---|---|
| 15 | 1.6 | 31.61 | $2.20 \times 10^{17}$ |
| 20 | 2.4 | 47.07 | $3.27 \times 10^{17}$ |
| 26 | 3.6 | 72.74 | $5.06 \times 10^{17}$ |
| 30 | 4.8 | 84.26 | $5.86 \times 10^{17}$ |

Using the relation, we can obtain the average electron density by measuring the fluorescence intensity.

### 4.4.2 Calibration of THz detectors

While relative intensity of THz radiation is sufficient for most discussions regarding THz generation, estimation of absolute power is necessary for the specification of THz source.

Calibration of detectors for *pulsed* THz radiation is an elusive topic. It is anticipated that the calibration factor depends on the pulse duration, spectrum, and presumably on incident angle and polarization of THz wave. Due to the lack of well-defined pulsed THz source that is universally available, it is for continuous wave that the manufactures can provide the calibration factor, usually given as an output voltage signal per unit power of incident wave.

Therefore, making public the method of calibration for power measurements of pulsed THz radiation is necessary for discussions that attempt any comparison of THz yields from experiments performed in different researches.

Here, calibration methods for pyrometer and bolometer are described in detail. Note that Golay cell has also been used in this research, but calibration has not been performed for a technical reason. It is known, however, that both golay cell and pyrometer has a very similar, flat frequency response [17]. Therefore, it is assumed they have the same response.

#### 4.4.2.1 Calibration of pyrometer

The pyrometer used in this research is *SPH-62 THz*, manufactured by *Spectrum Detector Inc*. For the calibration of the pyrometer, the laser pulse energy is measured by pyrometer as shown in Fig. 4.13. Here, the incident pulse had the

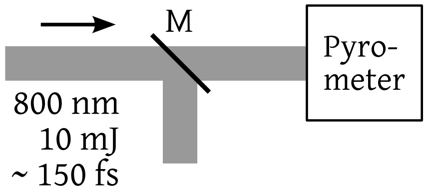


Figure 4.13: Setup for calibration of the pyrometer. Leakage of the incident laser light to the mirror M is measured by the pyrometer.

pulse duration of 150 fs and its energy was 10 mJ. The laser passes through a mirror (model No. TML1-800-45P-4050, an 800 nm-centered narrowband laser mirror manufactured by *CVI Laser Optics*) whose transmission is about 1 percent. The average voltage signal of the pyrometer was 0.34 V in response to the incident laser with energy of 100 μJ. Thus the response of the pyrometer is:

$$r_{\text{pyrometer}} = 34\ \mu\text{J/V} \tag{4.11}$$

#### 4.4.2.2 Note on Golay cell

Calibration of Golay cell with optical laser pulse has not been carried out since its window is made of high-density polyethylene (HDPE) which blocks most laser light. Golay cell has a gas cell inside and a built-in optics-to-voltage converter. It is basically a power meter that works in room temperature which can be used to detect THz radiation without the aid of cooling, unlike bolometers. Energy incident on the window leads to the gas cell to increase in volume, which is translated to voltage signal by the converter by emitting light from LED and monitoring the reflection. Since the conversion depends on the mechanical change in volume of the gas cell, Golay cell should be kept away from external vibration for precise detection. The transmission or absorption characteristics of filters (*TydexBlack* manufactured by *Tydex*, Russia) and Golay cell's window[18] determine the spectrum range of the Golay cell. Note that for continuous THz wave, ref. 19 gives a response of 0.59 μW/V after calibration with a free electron laser.

#### 4.4.2.3 Calibration of Bolometer

The response of the bolometer is estimated by comparing the bolometer's output signal in the experiment described in Chp. 4 (Exp. *b* hereinafter), with the absolute power estimated by a power rule, which is derived from the experiment described in Sec. 4.3 (Exp. $g$ hereinafter). In this section, for brevity, values related to the experiments using bolometer is denoted with a subscript $b$, whereas that using Golay cell is denoted by subscript $g$.

In Exp. $g$, where THz wave was generated using a laser pulse of 20 mJ, 70 fs, $f\#/20$, the maximum output signal from Golay cell was 0.02. See the Fig. 4.5 (page 54). The maximum energy of THz pulse in the blue curve is then $0.02 \times 34 = 0.68$ μJ.

Also note that when the laser energy increased by twice (from 20 mJ to 40 mJ), the THz energy increased by three times (from 0.02 to 0.06). the power law can be estimated as

$$\begin{cases} I_T = \alpha I^x \\ 3I_T = \alpha (2I)^x \end{cases}$$

$$x = \frac{\ln 3}{\ln 2} = 1.584963$$

where $\alpha$ is a constant unknown.

Let us find the ratio of laser intensity between Exp. $b$ and Exp. $g$. In Exp. $b$,

$$I_{F2} \propto \frac{2.5\text{ mJ}}{(15)^2} \cdot \frac{1}{70\text{ fs}}$$

, while in the Exp. $g$,

$$I_{F1} \propto \frac{20\text{ mJ}}{(20)^2} \cdot \frac{1}{70\text{ fs}}.$$

The ratio of intensity is

$$\frac{I_{F2}}{I_{F1}} = \frac{2.5}{40}\left(\frac{20}{15}\right)^2 = 0.111\cdots$$

We find the ratio of THz yield as

$$\frac{I_{T2}}{I_{T1}} = (0.111\cdots)^{\ln 3/\ln 2} = 0.03073$$

resulting in the THz yield in Exp. $b$ at $0.68$ μJ $\times\ 0.03073 = 0.020896$ μJ.

In Exp. $b$, the weakest THz yield was 0.1952, which corresponds to the THz energy of 0.021 μJ. Thus, the response of our bolometer is

$$r_{\text{bolometer}} = 0.108\,\mu\text{J/V}\,(\text{with G}_{\text{bolometer}} = 200)\,. \tag{4.12}$$

Note that the response should be divided by five if the bolometer gain is 1,000. With the FWHM pulse duration of 0.2 ps estimated by auto-correlation using carrier excitation at a silicon wafer, the response in term of power is given as:

$$r_{\text{bolometer,power}} = 0.54\text{MW/V} \tag{4.13}$$

If we assume that we could focus the THz wave to a diameter of 1 mm, the focused intensity response is:

$$r_{\text{bolometer,intensity}} = 68.75\text{MW/cm}^2 \tag{4.14}$$

In terms of electric field, by using $I = E^2/(2Z_0)$ where the impedance of vacuum $Z_0$ is about $120\pi$,

$$r_{\text{bolometer,field}} = 0.23\text{MV/cm} \tag{4.15}$$

## 4.5 Possibility of amplification

After establishing the THz generation by a two-color laser pulse and diagnostic techniques for plasma density and calibration of THz detectors, experiments to find the relation between plasma profile and THz power is performed. Figure 4.14 shows the setup of experiments performed using the P-cube laser system at Osaka University, an amplified Ti:sapphire laser system that delivered 10 mJ, 70 fs pulses with a central wavelength of 800 nm at a repetition rate of 10 Hz.

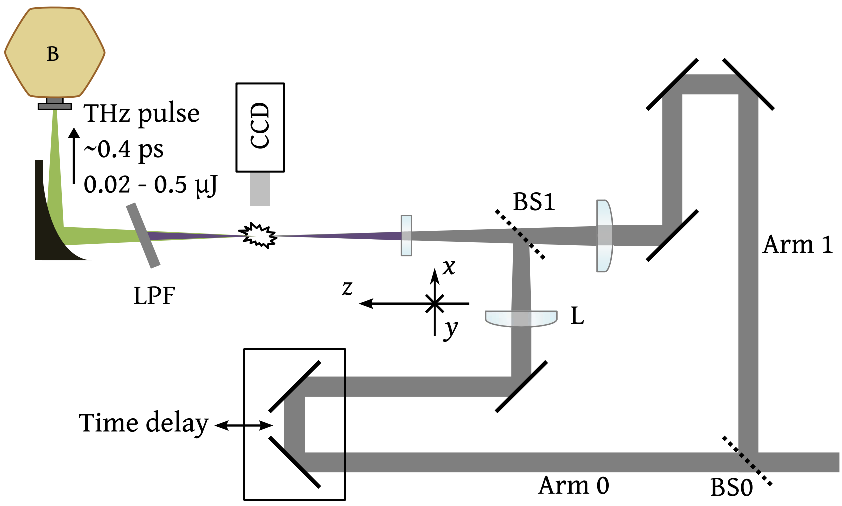


Figure 4.14: Experimental setup for THz wave generation with two-color scheme using two beams. BS: beam-splitter; L: focusing lens (focal length: 400 mm); BBO: 100- μm-thick type-I $\beta$-$BaB_2O_4$ (second harmonic generation); LPF: long pass filter with a cut-off frequency $\nu_{\mathrm{LPF,\,cut\text{-}off}} = 2.5$ THz ($\lambda = 120$ μm); OAP: off-axis parabolic mirror (focal length: 150 mm);

Two identical plano-convex lenses with a focal length of 400 mm were inserted in a Mach-Zehnder interferometer. The beam diameter was 26 mm. The diffraction limited beam diameter is 16 μm and the Rayleigh length is 1.0 mm. The lens in the one side of arm (hereafter, arm 0) was mounted on a two-dimensional linear stage to adjust the focus position of the laser beam. The lens on the other arm (hereafter, arm 1) was fixed throughout the experiments.

An energy of 5 mJ was supplied to each arm. We use $J$ to denote half of this energy after the last beam-splitter. The powers of the beams in each arm were identical (36 GW). After the beam-splitter *BS2*, the focal spot sizes of arms 0 and 1 were 25 and 50 µm, respectively, as shown in Figure 4.15. The difference in the beam diameter may be due to the changed beam quality by the thick beam splitter (BS1).

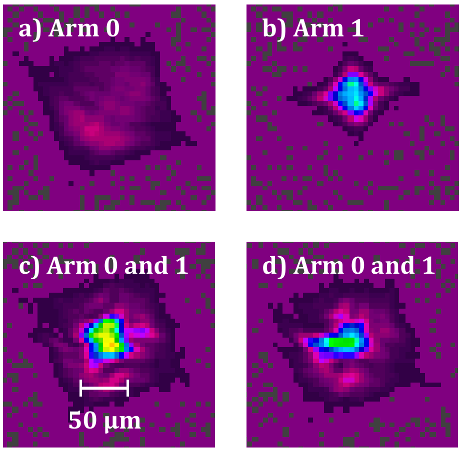


Figure 4.15: Focus image of beams from a) arm 0, b) arm 1, and c) and d) both the arm 0 and 1 to confirm the stableness of the overlap between two beams

A second-harmonic pulse was generated by a 100 µm-thick, type-I $\beta$-$BaB_2O_4$ (BBO) crystal. This crystal was mounted on a linear stage that can be translated along the laser beam axis to optimize the power of the THz wave from the two-color scheme as in Sec. 4.3. The generated $2\omega$ pulses were focused together with the $\omega$ pulses, ionizing the atmospheric gas at the foci of the lenses. A long-pass filter (LPF) with a 47-mm clear-aperture and a cut-off frequency at 2.5 THz is used to block laser pulses after the plasma. It limits the spectral range of our THz measurement. An off-axis parabolic mirror (focal length: 150 mm) focuses the generated THz pulses into a liquid He-cooled bolometer. Its calibration factor is estimated at 0.11 µJ/V [See Eq. (4.12)] by comparing its signal with a pyrometer.

The lenses of both arms were aligned so that the pulses from them were temporally synchronized, spatially overlapped in the transverse direction (in the $x$–$y$ plane) and focused at the same position. The spatiotemporal overlap is checked with the fringe pattern as shown in Fig. 4.16. A good spatial overlap results in a large wavelength, decreasing the number of fringes in the fringe pattern.

Figure 4.17 shows the white light emission of plasma filaments taken by CCD (resolution: 97 µm) for a set of combination of arm and energy. From the white light emission profile, the plasma electron density profile is estimated by calibrating its maximum intensity with the maximum electron density measured by a longitudinal diffraction method described in Sec. 4.4.1. Measurement of electron density profile of plasma filament is important, because the total power and the spectrum of THz wave would depend on it.

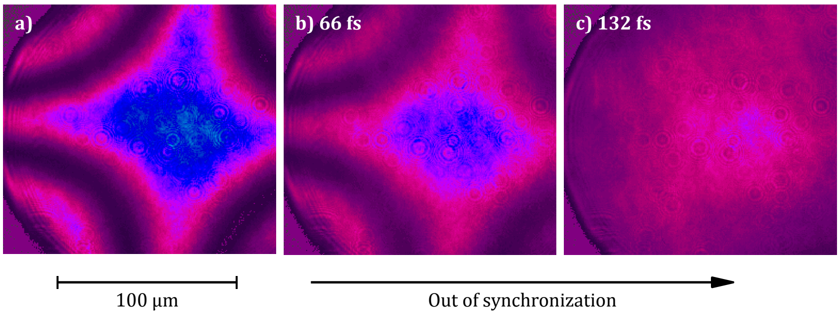


Figure 4.16: Fringe pattern between beams from arm 0 and 1. From left to right, time difference between two beams changes from a) 0, b) 66 fs, to c) 132 fs.

Figure 4.18 shows the plasma profile. Beam of energy $J$ or $2J$ on arm 1 generated symmetric plasma profiles as shown in line $D$ or line $B$, respectively. With the pulse on arm 0, the profile became asymmetric as in line $A$ and $C$; the density increased steeply at the head of the plasma and decreased gradually after the peak. The THz power measured for each plasma profile is shown as filled circle in Fig. 4.19.

The filled area in Fig. 4.18 shows the portion of plasma that can contribute to the THz power measured by the bolometer. Noting that the THz wave is generated at the plasma frequency ($\omega_p = \sqrt{n_e e^2/m_e\epsilon_0}$ [Hz], where $n_e$ is the plasma electron density, $e$ the elementary charge, $m_e$ the electron mass, and $\epsilon_0$ the permittivity of vacuum) at each point in the plasma profile[20], this area is chosen by two criteria: plasma is underdense to the THz wave, i.e., $\omega_p < \Omega$ and the plasma frequency $\omega_p$ is lower than the transmission cut-off of the LPF. Hereinafter, we refer to the length of those filled area as the plasma length.

Note that, as can be seen from Fig. 4.19, a beam with energy $J$ from either

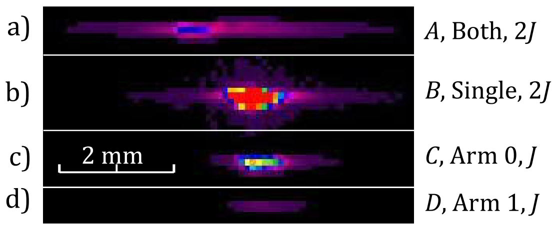


Figure 4.17: CCD images of white light emission from plasma generated by a) both arm 0 and 1 with combined energy of $2J$, b) arm 1 with energy of $2J$, c) arm 0 with energy of $j$, and d) arm 1 with energy of $j$.

arm 1 (point $D$) or 0 (point $C$) generates lower THz powers compared to the combined beam with a total energy of $2J$ (point $A$). However, a single beam with an energy of $2J$, obtained by removing the final beam-splitter, generated a THz power (point $B$) comparable to those obtained by a single beam with energy $J$ (points $C$ and $D$).

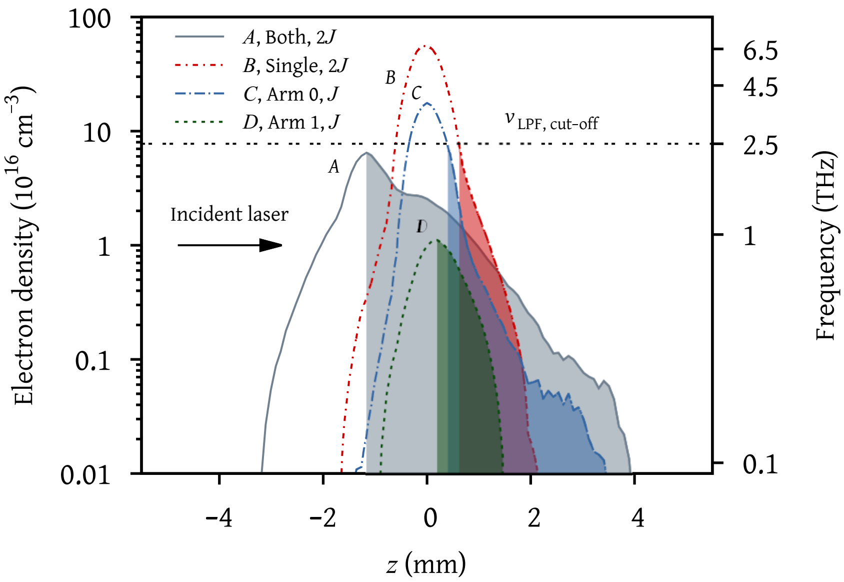


Figure 4.18: Electron density profile depending on different optical setups; either arm 1 (green dotted line) or arm 0 (blue dash-dotted line), both (gray solid line), and without splitting (red short dash-dotted line). Filled area indicates the portion of the plasma that contributes to the THz power measured by the bolometer (B), which is determined by considering the absorption of the THz wave by the plasma and the frequency cut-off of the LPF. Each profile is given an alphabetic label for reference.

## 4.6 Discussion

The fact that different plasma profiles generated by an identical total laser energy give THz yields different by an order of magnitude can be understood with the conventional model in which the THz intensity over one-dimensional plasma is given by[21]:

$$I_{\mathrm{THz}}(\Omega) \propto \left| \int_0^{L_p} \exp\left[\alpha\left(L_p - z\right)\right] \exp\left[i\phi\left(z\right)\right] dz \right|^2 \quad (4.16)$$

where $L_p$ is the plasma length, $\phi(z) = (\pi/L_c + k) / (L_p - z)$ is the phase of the THz wave at the end of the plasma, and $L_c = (4\pi/3)(\omega/\omega_p)^2 (c/\omega)$ is the coherence length* at which the phase of the generated THz wave changes[22].

The non-amplification case ($\alpha = 0$) had been solved previously[21]. In the portion of the plasma where the electron density decreases gradually, the THz wave has an infinite absorption length because the refractive index of the plasma is purely real in this region. In such a case, the integration can be simplified as a quadratic function of length:

$$I_{\mathrm{THz},\alpha=0} \propto 1 - \cos\left[\left(\frac{\pi}{L_c} + \frac{\Omega}{c}\right) L_p\right] \approx L_p^2 \tag{4.17}$$

For the amplification case ($\alpha > 0$), Eq. (4.16) with a finite amplification gain $\alpha$, which is similar to the expression for amplified spontaneous emission[23], can be solved as

$$I_{\mathrm{THz},\alpha>0} \propto 1 + \mathrm{e}^{2\alpha L_p} - 2\mathrm{e}^{\alpha L_p} \cos\left[\left(\frac{\pi}{L_c} + \frac{\Omega}{c}\right) L_p\right] \approx \mathrm{e}^{2\alpha L_p} \tag{4.18}$$

The second term becomes dominant as $\alpha L_p$, which represents the amplification, becomes larger than the upper bound of the third term, namely, $\alpha L_p > \ln(2) \approx 0.7$.

Figure 4.19 shows the measured THz power against the plasma length as well as the fit lines using the Eqs. (4.17) and (4.18). I used the Levenberg–Marquardt algorithm for nonlinear fitting with a tolerance of $10^{-4}$. The degree that the model fits the data well is represented by the coefficient of determination $R^2$. It is the square of the correlation between measured data and the fitted value. It ranges from zero to unity. The interpretation is that the percentage represented by the $R^2$ value in the dependant variable, i.e., measured data, is *explained* by a specific model with its independent variables, i.e., the amplification factor $\alpha$ and the plasma length $L_p$. For more detailed information, see page 7–10 in ref. 24.

It is readily seen that the exponential curve of Eq. (4.18) with the amplification factor $\alpha$ at 4.8/cm fits the measured THz power better (coefficient of determination $R^2 = 0.99$) than the quadratic fit using Eq. (4.17), whose $R^2$ is 0.89. It may suggest the possibility of THz amplification by laser-produced plasma. Still, the present evidence for THz amplification is rather limited. Current data is insufficient to rule out the possibility that the observed enhancement is due to increased THz generation efficiency, or better collection of the generated THz wave. Especially, experiments should

*Identical to the one defined in Sec. 2.3 (page. 14).

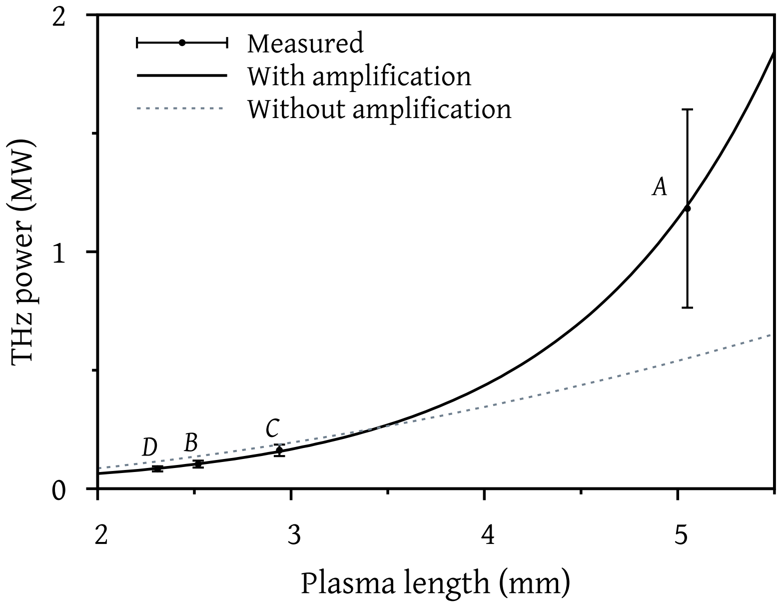


Figure 4.19: Dependence of the THz power on the adjusted plasma length with nonlinear fit lines obtained by considering amplification of the THz wave in the plasma (solid black line) and not considering amplification (gray dashed line). Each experimental data is given the identical label as in Fig. 4.18.

be performed with plasma length longer than the coherence length. The different focus diameter from arm 0 and arm 1 may need to be fixed by using a thin pellicle at the place of BS1.

## 4.7 Conclusion

In conclusion, it is shown that the nonlinear increase in the THz power may be attributed to an amplification of THz wave in the tail of the asymmetric plasma filament.

Using a model that considers amplification, the nonlinear growth of THz power is shown to be exponential rather than quadratic and that it depends on the length of plasma tail where the electron density decreases gradually after its peak.

# References

[1] A. Couairon and A. Mysyrowicz, "Femtosecond filamentation in transparent media," Physics Reports **441**, 47 (2007).

[2] L. Bergé, S. Skupin, R. Nuter, J. Kasparian, and J.-P. Wolf, "Ultrashort filaments of light in weakly ionized, optically transparent media," Reports on Progress in Physics **70**, 1633 (2007).

[3] H. Zhong, N. Karpowicz, and X.-C. Zhang, "Terahertz emission profile from laser-induced air plasma," Applied Physics Letters **88**, 261103 (2006).

[4] Y. Liu, a. Houard, M. Durand, B. Prade, and a. Mysyrowicz, "Maker fringes in the Terahertz radiation produced by a 2-color laser field in air." Optics express **17**, 11480 (2009).

[5] J.-M. Manceau, M. Massaouti, and S. Tzortzakis, "Strong terahertz emission enhancement via femtosecond laser filament concatenation in air," Optics letters **35**, 2424 (2010).

[6] A. G. York and H. M. Milchberg, "Broadband terahertz lasing in aligned molecules." Optics express **16**, 10557 (2008).

[7] T.-J. Wang, S. Yuan, Z.-D. Sun, C. Marceau, Y. Chen, F. Théberge, M. Châteauneuf, J. Dubois, and S. Chin, "Molecular alignment control of terahertz emission from a two-color filament in air," Laser Physics Letters **8**, 295 (2011).

[8] Y. S. You, T. I. Oh, a. B. Fallahkhair, and K. Y. Kim, "Alignment-dependent terahertz radiation in two-color photoionization of molecules," Physical Review A **87**, 035401 (2013).

[9] M.-K. Chen, J. H. Kim, C.-E. Yang, S. S. Yin, R. Hui, and P. Ruffin, "Terahertz generation in multiple laser-induced air plasmas," Applied Physics Letters **93**, 231102 (2008).

[10] J. Dai, X. Xie, and X.-C. Zhang, "Terahertz wave amplification in gases with the excitation of femtosecond laser pulses," Applied Physics Letters **91**, 211102 (2007).

[11] M. Born and E. Wolf, "Principles of Optics," (Cambridge University Press, Cambridge, 1999) 7th ed., Chap. 8.5.2.

[12] J. Yao and Y. Wang, "Nonlinear Optics and Solid-State Lasers," (Springer Berlin Heidelberg, Berlin, Heidelberg, 2012) Chap. 9.

[13] P. E. Ciddor, "Refractive index of air: new equations for the visible and near infrared." Applied optics **35**, 1566 (1996).

[14] J. Liu, Z. Duan, Z. Zeng, X. Xie, Y. Deng, R. Li, Z. Xu, and S. Chin, "Time-resolved investigation of low-density plasma channels produced by a kilohertz femtosecond laser in air," Physical Review E **72**, 026412 (2005).

[15] Z. Zhang, X. Lu, T.-T. Xi, W.-X. Liang, Z.-Q. Hao, Y. Zhang, M.-L. Zhou, Z.-H. Wang, and J. Zhang, "Long distance filamentation of 400 nm femtosecond laser pulses in air," Applied Physics B **97**, 207 (2009).

[16] A. Talebpour, S. Petit, and S. Chin, "Re-focusing during the propagation of a focused femtosecond Ti:Sapphire laser pulse in air," Optics Communications **171**, 285 (1999).

[17] A. Rogalski, "Infrared detectors: status and trends," Progress in Quantum Electronics **27**, 59 (2003).

[18] Tydex J. S. Co., "THz materials and components," (2010).

[19] E. Chiadroni, "Report on the visit at FELIX, FOM Rijnhuizen," (2005).

[20] M. Chen, A. Pukhov, X.-Y. Peng, and O. Willi, "Theoretical analysis and simulations of strong terahertz radiation from the interaction of ultrashort laser pulses with gases," Physical Review E **78**, 046406 (2008).

[21] E. Constant, D. Garzella, P. Breger, E. Mével, C. Dorrer, C. Le Blanc, F. Salin, and P. Agostini, "Optimizing High Harmonic Generation in Absorbing Gases: Model and Experiment," Physical Review Letters **82**, 1668 (1999).

[22] K. Y. Kim, A. J. Taylor, J. H. Glownia, and G. Rodriguez, "Coherent control of terahertz supercontinuum generation in ultrafast laser–gas interactions," Nature Photonics **2**, 605 (2008).

[23] R. C. Elton, *X-Ray Lasers* (Academic Press, New York, 1990).

[24] J. O. Rawlings, S. G. Pantula, and D. A. Dickey, *Applied Regression Analysis: A Research Tool*, 2nd ed. (Springer, 1998).

# Chapter 5

# Spectrum-Narrowing of Intense THz Radiation

## 5.1 Introduction

To date, experimental and theoretical studies of the THz radiation during the interaction of femtosecond laser pulses and plasma have focused on uniform targets, which are easier to realize in experiments [1–8]. The resulting THz radiation has a broad spectral distribution, which diminishes the field of application for such sources.

To produce quasi-monochromatic THz signals attractive for spectroscopy as well as for studies of nonlinear properties and nonequilibrium states of matter [9], a metallic hollow waveguide filled with a bulk gas has been proposed for THz and pump lasers with numerical demonstrations [10].

A femtosecond laser pulse propagating in a gas target also produce a plasma channel that can be a mode-selective waveguide for THz radiation. Radiation components whose frequencies are lower than that of a wall plasma frequency would be guided by the refraction. For much lower-frequency components, the diffraction loss increases owing to the finite size of the plasma skin layer. Moreover, some of the components with frequencies lower than the plasma frequency cannot propagate in the plasma.

There are several clear ways to produce nonuniform gaseous targets: strong acoustic waves in the 1–10 MHz range [11,12], recombined channels generated by nanosecond laser pre-pulses [13–16], and density modulated gas jets [17–19]. All these methods produce density ripples in gas targets.

In this section, narrowband and intense THz wave generation is demonstrated in particle-in-cell simulations with plasma waveguide which is generated through optical field ionization of a nonuniform gas target. Since the THz radiation is limited within the lateral dimension of waveguide, manipulation of THz wave generated in this method is easier than the one generated from a uniform gas (Chp. 3). For example, we may design TW THz radiation source with a waveguide array as described in Chp. 5.7.

## 5.2 Formation of plasma waveguide

To perform a numerical investigation of generation and propagation of THz radiation by a femtosecond laser pulse in a density rippled air target, the initial gas density is sinusoidally modulated as shown in Fig. 5.1, thus called the density ripple, in the form

$$N_{\text{gas}} = N_0 \left[1 - A\cos\left(2\pi y/p\right)\right], \tag{5.1}$$

where $N_0$ is the atmosphere pressure, $A$ is a modulation parameter that sets the contrast of the initial gas density $r = (1 + A) / (1 - A)$, and $p$ is a period, set as another parameter in this study. The $s$-polarized laser pulse with FWHM duration $\tau = 28$ fs and wavelength $\lambda = 0.8$ μm is focused at an intensity $I \leq 10^{16}$ W/cm$^2$ with a waist $w_0 = 10.6$ μm centered at the valley of the density ripple.

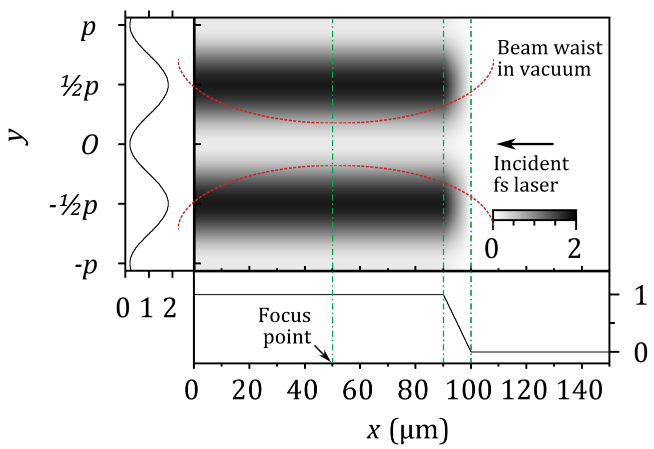


Figure 5.1: Initial gas density of the nonuniform gas target. The transverse profile is shown on the left, which is sinusoidally modulated with a period $p$. A single-color Gaussian fs laser pulse is focused 50 μm inside the target as marked by green dash-dot line. The red dashed line illustrates the beam diameter.

The same particle-in-cell simulation code used in Chp. 3, including the optical field ionization[20] is used. Note that the laser pulse propagates from right to left side. The moving window method is used with a simulation area of $150 \times 320\ \mu m^2$ and a spatial resolution $\Delta x = \Delta y = \lambda/20$.

The evolution of the laser pulse in the density ripple of a gaseous target is shown in Fig. 5.2. One can see two dominant processes in the pulse propagation: strong diffraction of the pulse front and essential self-focusing of the pulse rear. The diffracted part of the pulse then forms a periodic structure, as seen in Fig. 5.2(b)–(c), reflecting the interaction of that part of the pulse

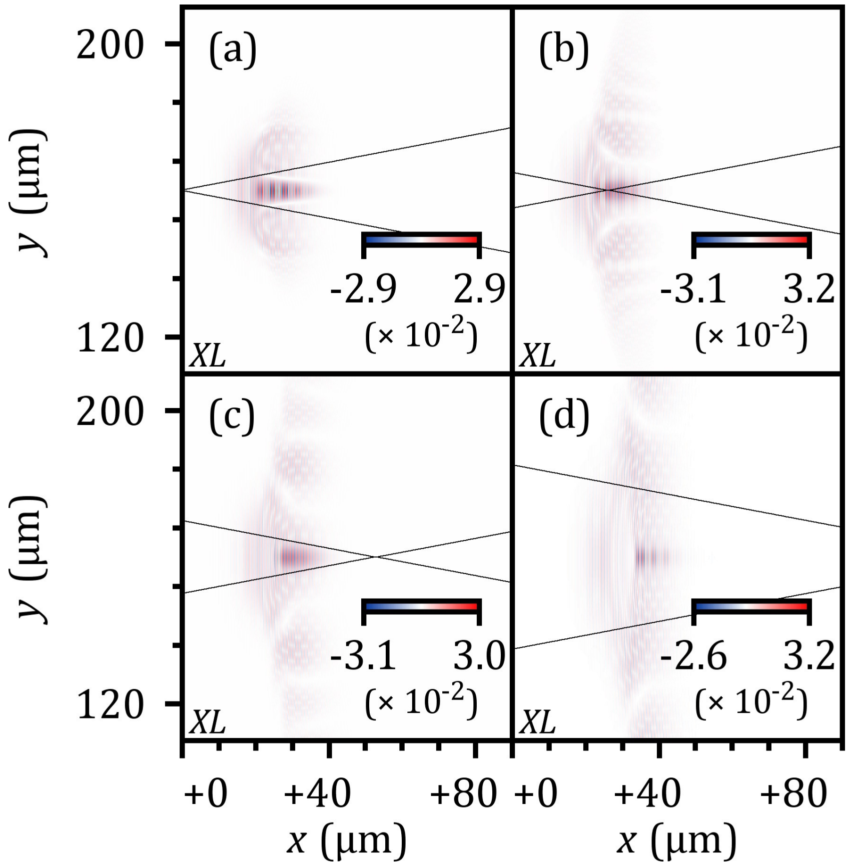


Figure 5.2: $S$-polarized electric fields in the simulation domain after propagation from right to left for (a) 0.35, (b) 0.7, (c) 1.05, and (d) 2.1 ps in the density-modulated gas; leftmost coordinate of the moving window, $XL$ is $-105$, $-210$, $-315$, and $-630$ μm, respectively. The black lines show the $1/e$-beam diameter of the incident Gaussian beam in vacuum. Modulation parameters are $r = 10$ and $p = 18.8$ μm.

with the closest density ripples. The intensity of the focused part gradually decreases but not significantly. Self-focusing effect may be observed clearer in Fig. 5.3 where the electric field over the simulation area and the corresponding one dimensional profile along the laser axis are shown for vacuum, uniform air, and the rippled target.

Figure 5.4 shows the low-frequency portion ($<$ 75 THz) of the field extracted by applying a low-pass filter.

Initially, the spectrum is quite broad; different widths of the field oscillation are clearly seen. However, in Fig. 5.4(d), the structure of the THz radiation is very regular and monochromatic. The same dynamics is observed in the electron density, as shown in Fig. 5.5, in which the maximum electron density is about $N_e \sim 2 \times 10^{19}\text{cm}^{-3}$. A comparison of the corresponding panels in Fig. 5.2 and Fig. 5.5 reveals that strong diffraction of the radiation occurs initially as the main density ripple is strongly modulated in the transverse direction. However, shortly afterward, the density structure becomes regular with a clear ionization modulation [Fig. 5.5(b)].

Figure 5.6 shows the evolution of the electric field, density, and spectrum along the laser axis, in order to clarify the time dependencies. The electric field $E$ is normalized as $a_z = eE_z/mc\omega$, where $e$ is the electron charge, $m$ is the electron mass, and $\omega$ is the laser frequency. Figure 5.6(a) and (b) show steepening of the laser pulse, which is typical in the formation of THz radiation, as has been studied in ref. 21. We can attribute this formation to a beat-wave intersection. The peak amplitude of the THz signal increases as its spectrum becoming monochromatic. This is also confirmed by the spectra shown in Fig. 5.6(c–d). Near the laser radiation, we can see a very strong modulation produced by nonlinear focusing of the beat-wave, as described in Eq. (5.4). As the modulation progresses, the THz signal increases, and its bandwidth becomes narrower. The two-dimensional spectra shown in Figure 5.6(e) and (f) confirm that the THz signal has a strong monochromatic distribution in both the $x$ and $y$ directions.

The role of diffraction in the formation of the mode can be seen by comparing Fig. 5.5 and Fig. 5.6(c) and (d). The diffraction loss is initially very strong because of strong optical field ionization at the periphery of the ripple; it lessens after mode formation.

## 5.3 Tunability

The tunability of the scheme can be seen in Fig. 5.7 which shows the different spectra for various ripple parameter settings as well as those corresponding to uniform air for comparison. Note also that the THz radiation intensity exceeds

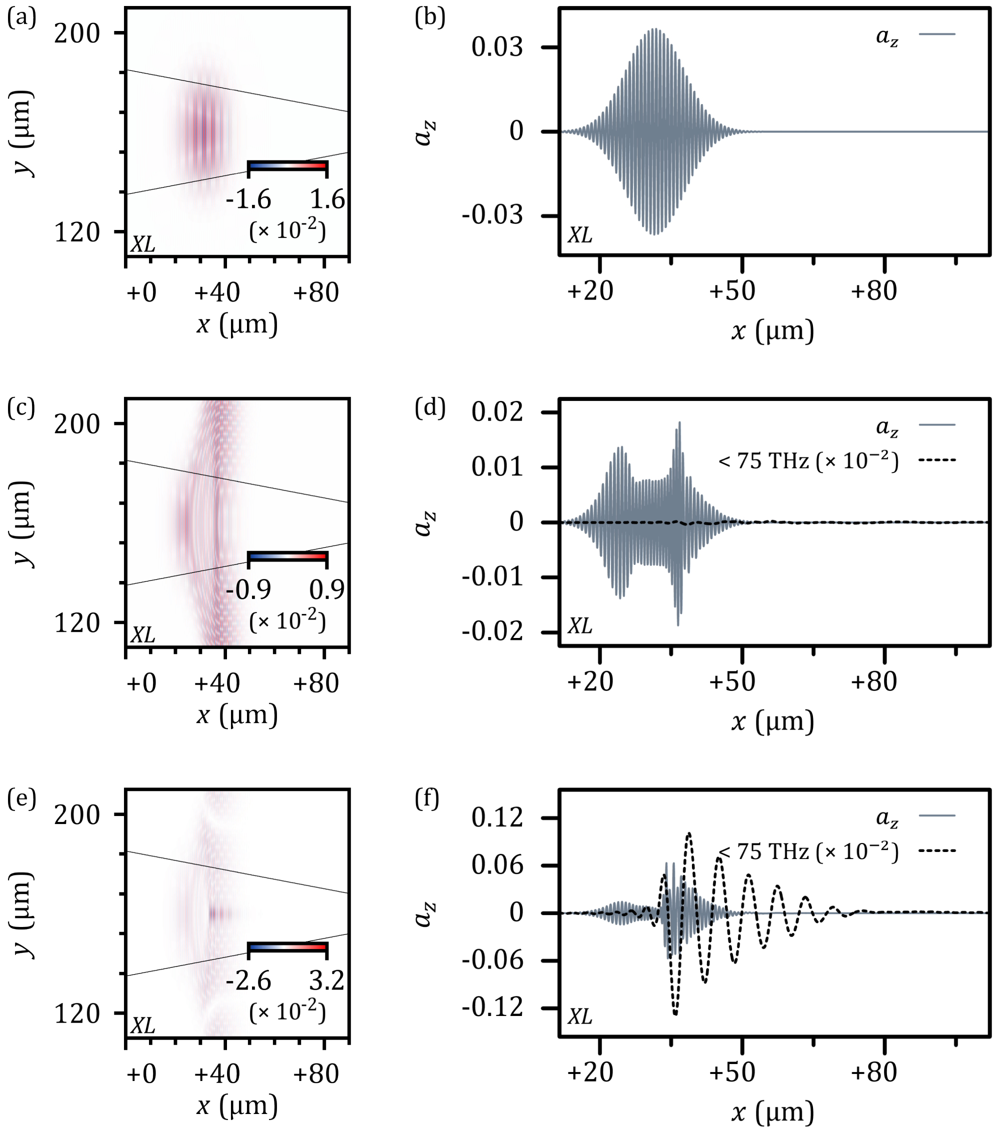


Figure 5.3: Electric field and the one dimensional profile along the laser axis, respectively, for air [(a) and (b)], uniform air [(c) and (d)], and the rippled air target [(e) and (f)] after 2.1 ps. The black lines in (a), (c) and (e) show the $1/e$-beam diameter of the incident Gaussian beam in vacuum. The leftmost coordinate of the moving window, *XL* is −630 µm. The density for the uniform air is identical to the average density of the rippled target at $3 \times 10^{19}\,\mathrm{cm}^{-3}$. Modulation parameters for the rippled air target are $r = 10$ and $p = 18.8$ µm.

the intensity generated from the uniform gas by two orders of magnitude. Peak

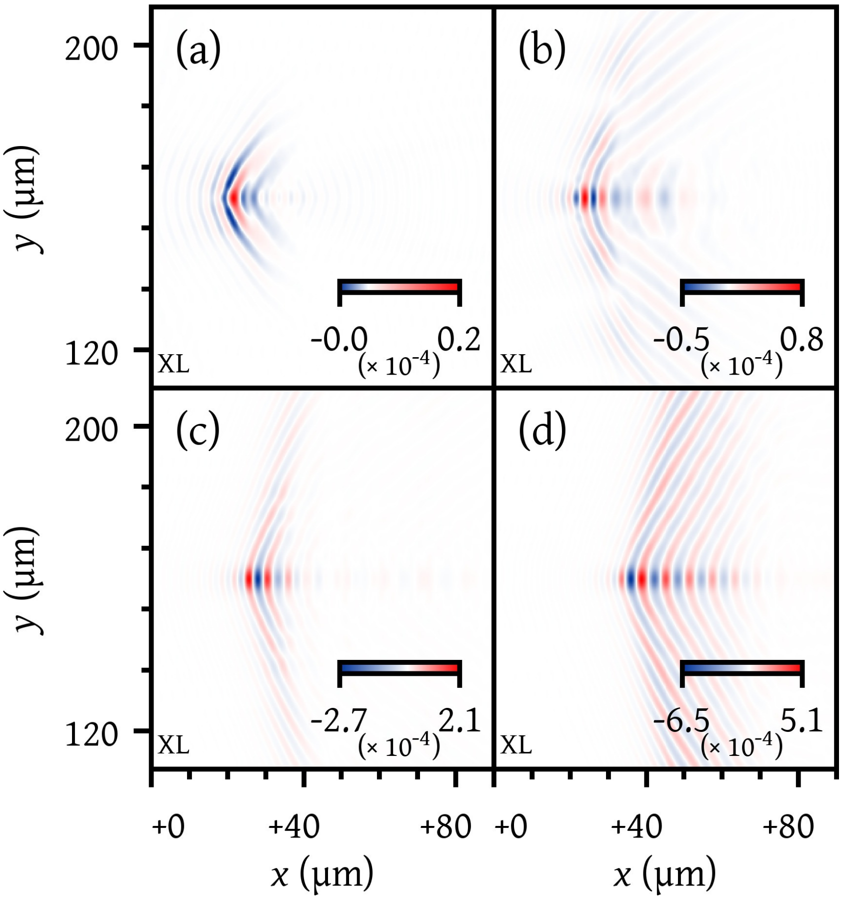


Figure 5.4: Low-frequency component (< 75 THz) of the $s$-polarized electric field. Simulation times and the leftmost coordinate of the moving window, $XL$, are the same as in Fig. 5.2. Modulation parameters are $r = 10$ and $p = 18.8$ μm.

THz wavelength aginst the modulation period $p$ is shown in Fig. 5.8. A linear relation regression line may also be drawn.

## 5.4 Gain

Figure 5.9 shows the gain coefficient $g_+$ for $\nu_x = 49$ THz in $I(k) \propto \exp(g_+ct)$. The gain is about $g_+ \sim 100\ \mathrm{cm}^{-1}$, proving that a very strong nonlinear interaction exists between the modes in the plasma channel. The gain is calculated by assuming the THz intensity can be represented by an exponent as $I(k) = A\exp(g_+ct)$. The gain $g$ that the THz wave is subjected to during its propagation from a point $x$ and to the other $x'$ can be evaluated by comparing

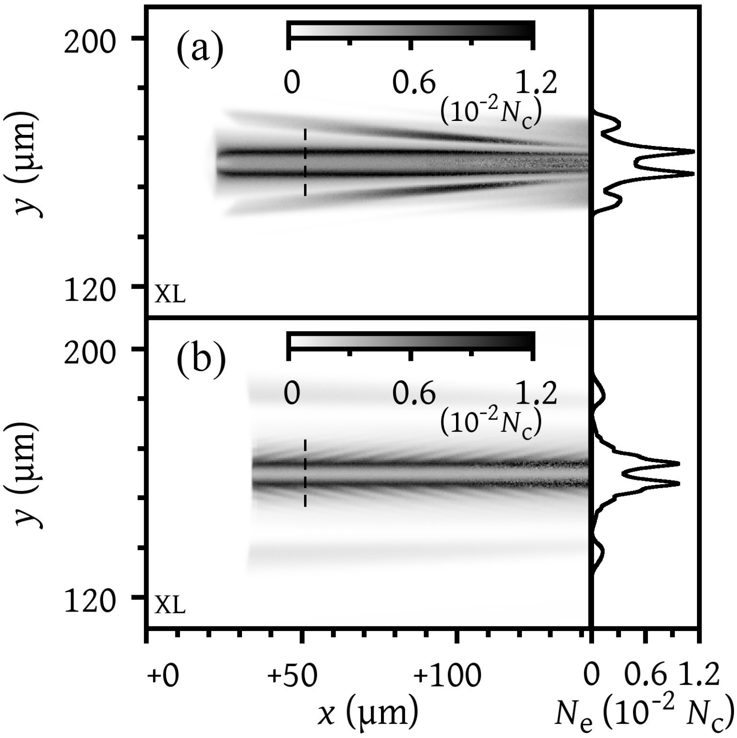


Figure 5.5: Electron density (normalized by $N_c = 1.74 \times 10^{21}\,\mathrm{cm}^{-3}$) produced by tunnel ionization of the incident laser field propagating from right to left, taken at (a) 0.7 and (b) 2.1 ps with $XL$ −210 and −630 μm, respectively. The corresponding transverse profiles along $XL + 50$ μm (the dashed line) are shown on the right. Modulation parameters are $r = 10$ and $p = 18.8$ μm.

the change in the intensity:

$$\begin{cases} I' = A\exp\left(gx'\right) \\ I = A\exp\left(gx\right) \end{cases} \tag{5.2}$$

Diving them

$$\frac{I'}{I} = \exp\left[g\left(x' - x\right)\right]$$

and arranging them yields the expression for the gain

$$g = \frac{\ln\left(I'/I\right)}{x' - x}$$

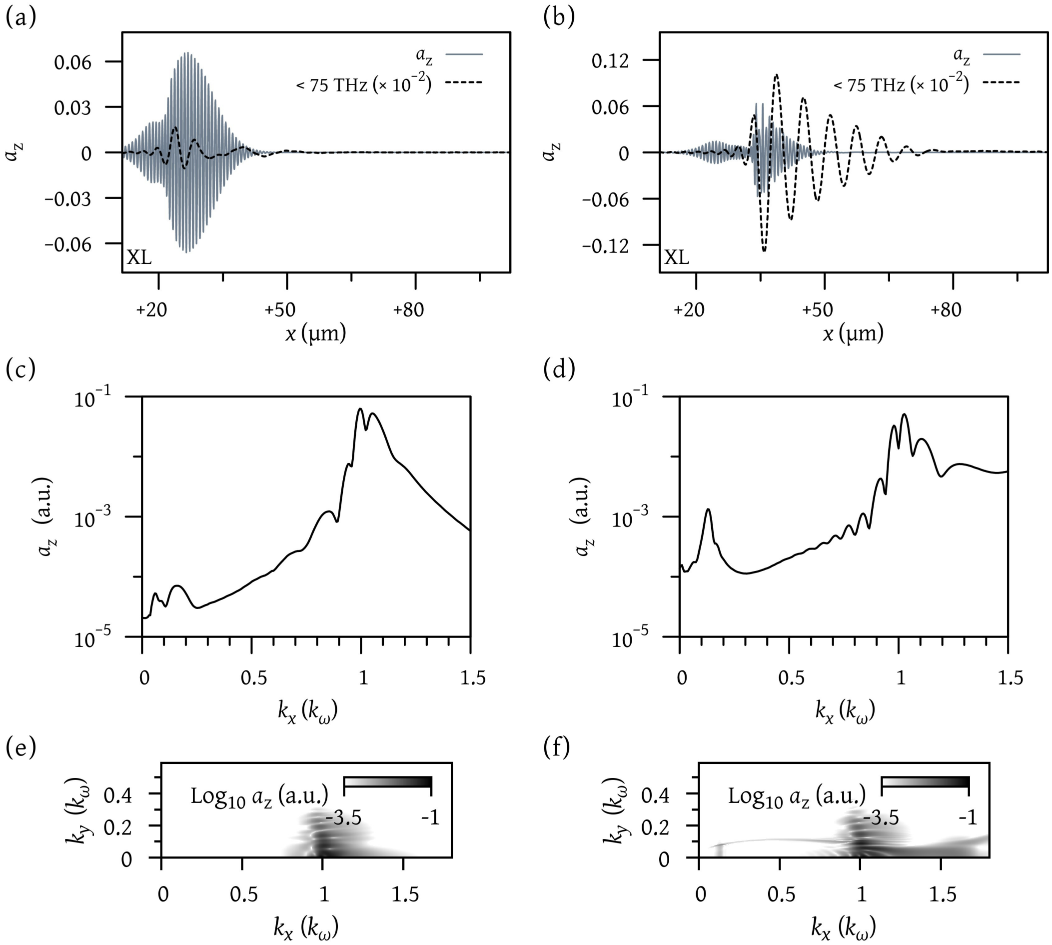


Figure 5.6: Time evolution of the electric field and its low frequency components, one-dimensional spectrum along the laser axis, and two-dimensional spectrum taken at (a), (c), (e) t = 0.7 ps, and (b), (d), (f) 2.1 ps with *XL* being −210 and −630 µm, respectively. Modulation parameters are $r = 10$ and $p = 18.8$ µm.

Here we assume that the THz wave propagated in the speed of light $c$, yielding the gain between certain period of time between $t'$ and $t$:

$$g = \frac{\ln (I'/I)}{c\,(t' - t)} \tag{5.3}$$

The origin of the gain is unclear. One possible mechanism for the enhancement of THz power, though, can be derived from the beat-wave mechanism described in Sec. 2.4 and ref. 21: Briefly, the field ionization of a gas target

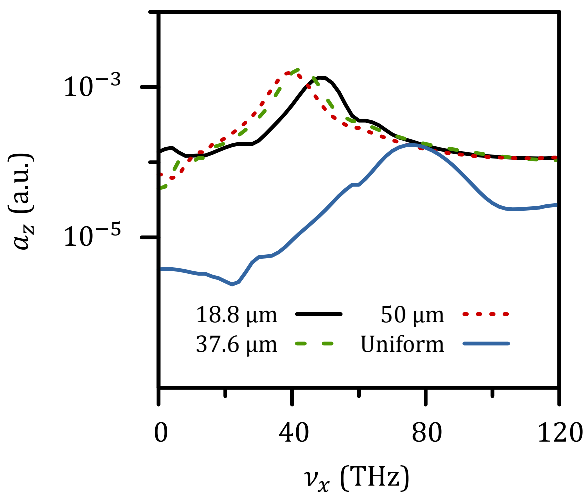


Figure 5.7: Dependence of the low-frequency portion of the spectrum (< 113 THz) on the modulation period $p$ at $t$ = 2.1 ps; for uniform gas, 0.7 ps.

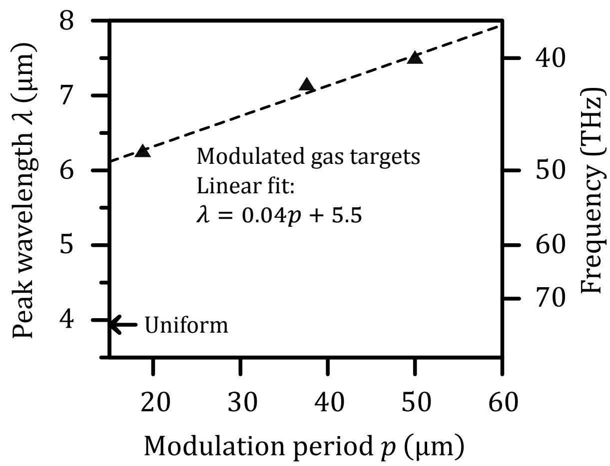


Figure 5.8: Peak THz wavelength for each modulation period $p$, obtained from the peaks in Fig. 5.7. Right axis shows the corresponding frequency for the wavelength on the left axis.

divides a laser pulse roughly into two parts: a frequency-upshifted $(\omega', k_0)$ part at the front of the pulse and a $k$-vector-downshifted part $(\omega_0, k')$ at the rear. These parts and an incident second harmonic $(2\omega_0, 2k_0)$ induce THz ra-

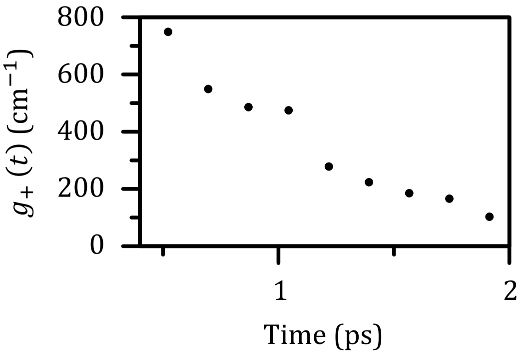


Figure 5.9: Temporal change in plasma gain coefficient for THz waves at 49 THz. Modulation parameters are $r = 10$ and $p = 18.8$ µm.

diation via four-wave mixing. Because the mixing of the front and rear parts of the laser pulses quickly vanishes owing to electron density steepening[21], the efficiency of the process is low. In a plasma waveguide, the mixing may last longer, leading to a higher laser-to-THz conversion efficiency. Longer mixing time can be explained via the paraxial equations for a parabolic channel and a radiation component $\omega_{\mathrm{R}}$:

$$i\omega_{\mathrm{R}}A' + 4c^2B + \bar{\omega}_{\mathrm{pl}}^2(t,x) = 0 \tag{5.4a}$$

$$-i\omega_{\mathrm{R}}B' - 4c^2B^2 + \bar{\omega}_{\mathrm{pl}}^2(t,x)\,\eta(t,x) = 0 \tag{5.4b}$$

where $A' = \partial A/\partial t \pm c\,\partial A/\partial x$, the plasma frequency $\omega_{\mathrm{pl}}$ has the following form: $\omega_{\mathrm{pl}}^2(t,x,r) = \bar{\omega}_{\mathrm{pl}}^2(t,x)\left[1+\eta(t,x)\,r^2\right] = 0, \eta = \nu/D^2$, $D$ the channel diameter, $\nu$ the density ramp, and the field is given by

$$\boldsymbol{E} = \boldsymbol{\varepsilon}\exp\left[i\omega_{\mathrm{R}}t - ik_Rx + A(t,x) - B(t,x)\,r^2\right]. \tag{5.5}$$

Without a longitudinal modulation and the instant plasma generation[21], i.e., $\omega_{\mathrm{pl}}(t<0) = 0$ and $\omega_{\mathrm{pl}}(t>0) = \omega_{\mathrm{pl}}^0$, the solution for the waist of the radiation with frequency $\omega_{\mathrm{R}}$ is:

$$B(t) = \mathrm{Re}\left\{B_0 + \frac{1 - B_0w_0^2}{w_0^2 + i4c^2t\left(1 - B_0w_0^2\right)/\omega_{\mathrm{R}}}\right\}, \tag{5.6}$$

with $B_0 = \bar{\omega}_{\mathrm{pl}}\sqrt{\nu}/2Dc$ and $w_0$ the laser pulse waist; all radiation components should have $w(t=0) = w_0$ initially. One can see that asymptotically the waist size does not depend on frequency. However, the retention time strongly depends on the frequency of a component, resulting in different transverse dynamics for the radiation components and a greatly intensified beat-wave.

Table 5.1: Parameters of the parabolic plasma density in transverse direction

| $r$ | $y_0$ (μm) | $n_0$ ($10^{18}\,\mathrm{cm}^{-3}$) | $\Delta n$ ($10^{19}\,\mathrm{cm}^{-3}$) |
|---|---|---|---|
| 3 | 159.96 | 16.9 | 6.18 |
| 10 | 159.93 | 6.19 | 12.6 |
| 30 | 159.91 | 2.59 | 14.3 |

## 5.5 Dependence on the gas density contrast

All simulation results presented so far are performed with the modulation amplitude $r = 10$. Simulations with different modulation amplitudes were also performed for $r = 3$ and 30. Table 5.1 shows parameters of the plasma density profiles fit into a parabolic form of

$$n(r) = n_0 + \Delta n \,(r - y_0)^2 / r_0^2 \tag{5.7}$$

where $r_0 = 10.6$ μm is the pulse waist. Increasing $\Delta n$ means steeper density gradient. Decreasing $n_0$ indicates higher density contrast.

For the lower contrast of $r = 3$, the mode existed only for a short time less than 2 ps as shown in Fig. 5.10. It may suggest the existence of critical gas contrast, similar to the critical channel depth $\Delta n_c$ that have been found for preformed plasma density channels[22]; given a parabolic plasma density as in Eq. (5.7), a Gaussian laser pulse with a pulse waist of $r_0$ can be guided if the modulation $\Delta n$ is larger than the critical channel depth

$$\Delta n_c = \frac{1}{\pi r_e r_0^2} \tag{5.8}$$

$$\simeq 1.13 \times 10^{20} / r_0^2 \,[\mathrm{cm}^{-3}/\mu\mathrm{m}^2] \tag{5.9}$$

where $r_e = e^2/mc^2$ is the classical electron radius. Note that for all modulation parameter $r$, $\Delta n > \Delta n_c$ is satisfied, indicating that the theory for preformed plasma does not directly apply to the present scheme.

For the higher contrast of $r = 30$, the mode was stable (Fig. 5.11), but its power was only 50 percent of that at $r = 10$ ($A = 9/11$), as shown in Fig. 5.12. This result suggests the existence of optimal value of intial gas contrast $r$.

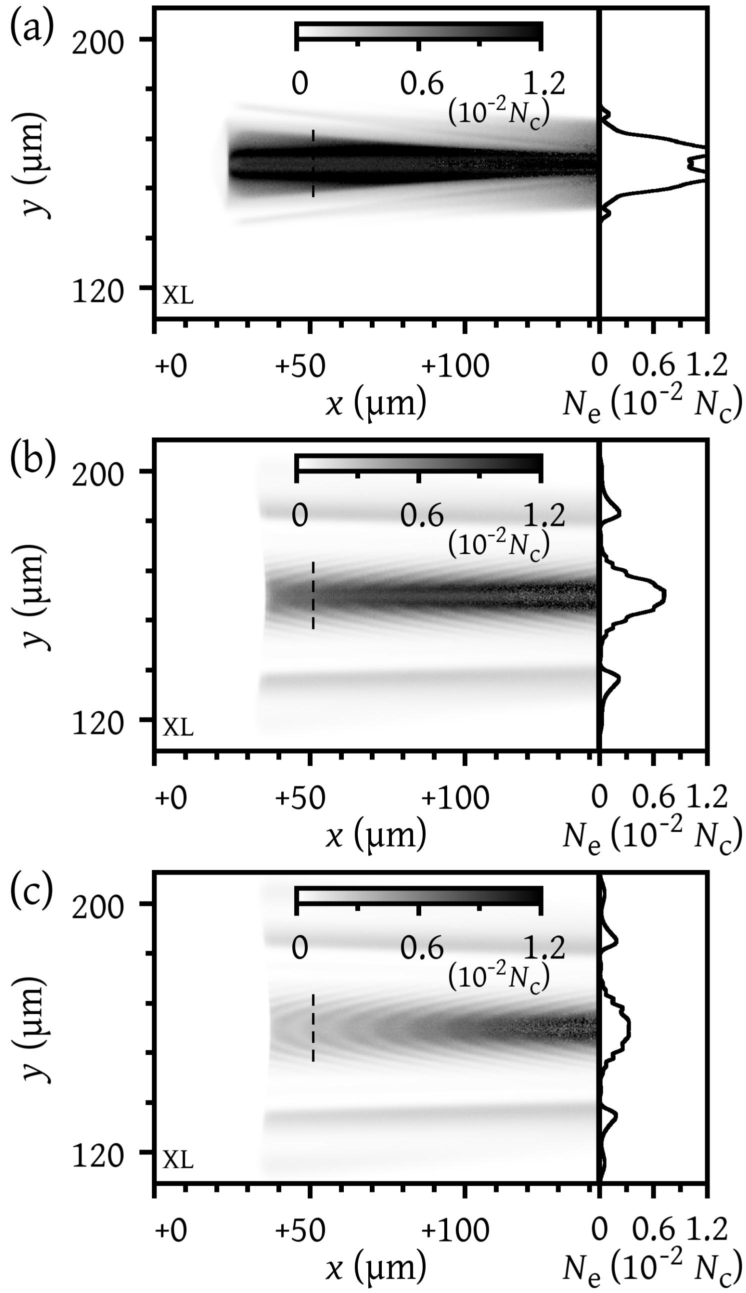


Figure 5.10: Electron density produced by tunnel ionization of the incident laser field propagating from right to left, taken at (a) 0.7, (b) 1.93, and (c) 2.1 ps with $XL$ −210, −578, and −630 µm, respectively. The corresponding transverse profiles along $XL + 50$ µm (the dashed line) are shown on the right. Modulation parameters are $r = 3$ and $p = 18.8$ µm.

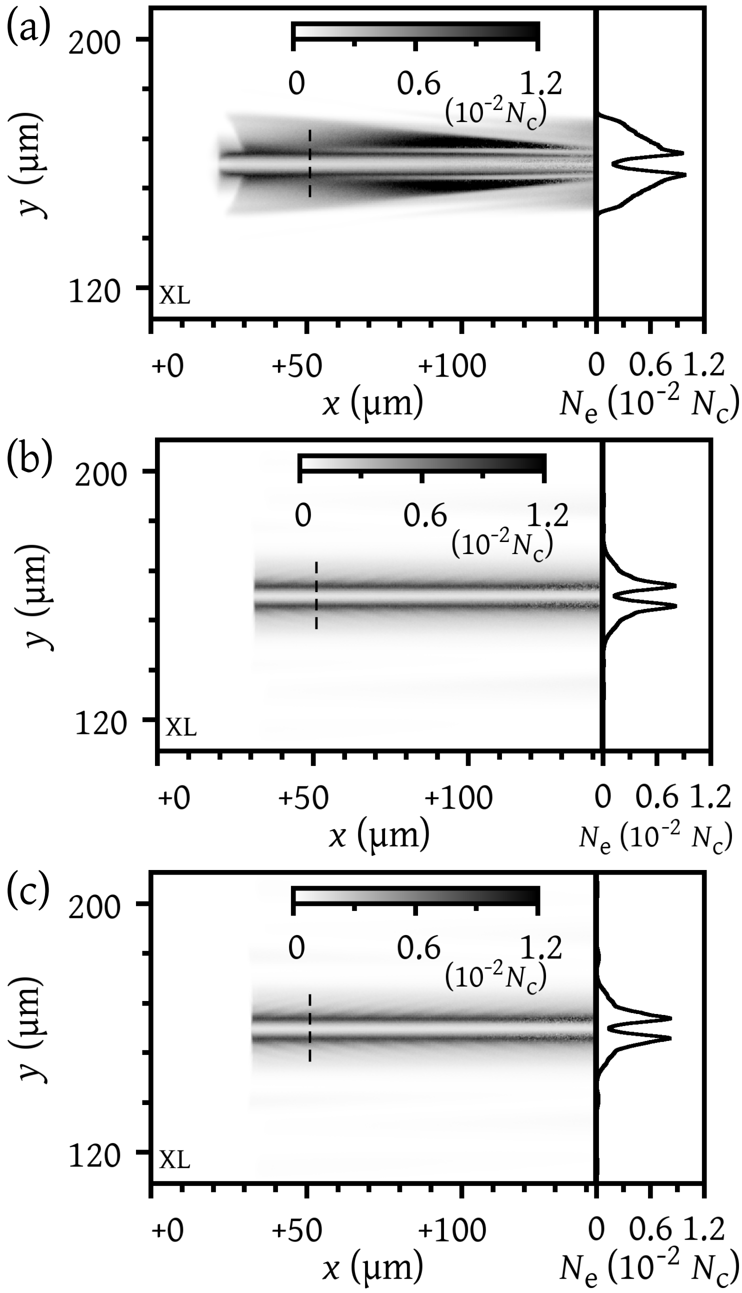


Figure 5.11: Electron density produced by tunnel ionization of the incident laser field propagating from right to left, taken at (a) 0.7, (b) 1.93, and (c) 2.1 ps with $XL$ −210, −578, and −630 µm, respectively. The corresponding transverse profiles along $XL + 50$ µm (the dashed line) are shown on the right. Modulation parameters are $r = 30$ and $p = 18.8$ µm.

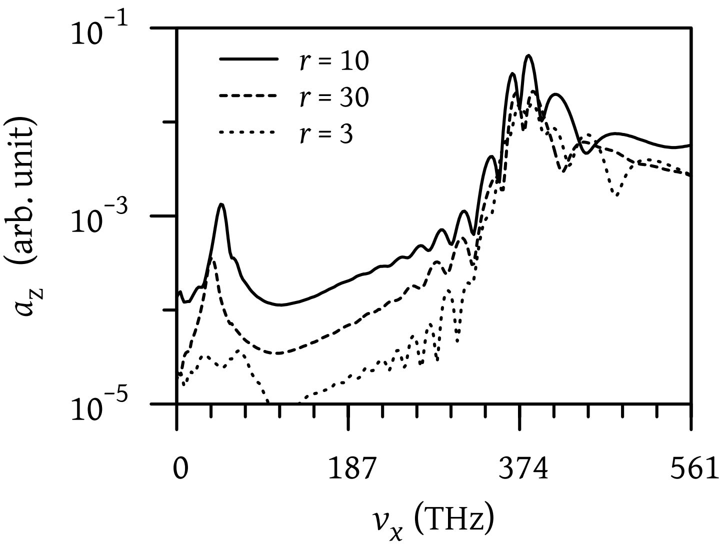


Figure 5.12: Spectrum at $t = 2.1$ ps for different initial gas density contrast $r$ (modulation period $p = 18.8$ μm)

## 5.6 Similarity to single-mode fiber

It is also noteworthy that the concave electron density profile along the transverse direction shown in Fig. 5.13 for $r = 10$ case has a refractive index profile that is similar to index-graded fiber in their structures. The refractive index $N$ of plasma is

$$N = \sqrt{1 - \frac{n_e}{n_c}} \tag{5.10}$$

where $n_e$ is the plasma electron density, and $n_c$ is the critical density of plasma. The graded-index fiber has a power-law index profile given by

$$N(r) = \begin{cases} n_1\sqrt{1 - 2\Delta\,(r/\alpha)^g} & \text{if } r \le \alpha, \\ n_2 & \text{if } r \ge \alpha. \end{cases} \tag{5.11}$$

where $n(r)$ is the transverse refractive index along the radius $r$, $n_1$ is the maximum refractive index of the core, $n_2$ is the refraction index of the cladding, $\Delta = (n_1^2 - n_2^2)/(2n_1^2)$, and $g$ is called the grade profile parameter[23]. Figure 5.14 shows the refractive index of plasma shown in Fig. 5.13 with a fit-curve to the power-law index profile with $n_1 = 0.8$, $n_2 = 0.2$, $\alpha = 3$ μm, and $g = 2$. Here, the lowering electron density near the peak, thus increasing refreactive

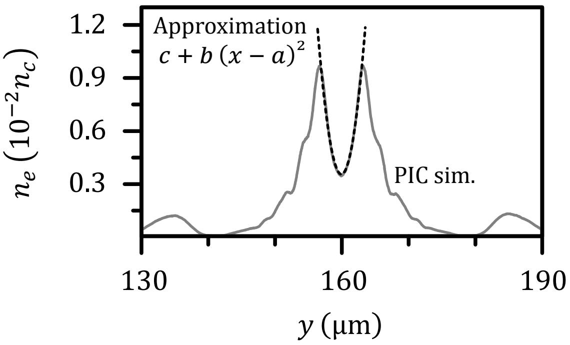


Figure 5.13: Transverse electron density profile at $x = XL + 50$ μm after 2.1 ps of simulation. The parameters for the approximation by a quadratic function are $a = 159.9$, $b = 0.065$, and $c = 0.356$. Modulation parameters are $r = 10$ and $p = 18.8$ μm.

index is ignored.

According to the theory of index-graded fiber, the fiber is single-mode (only transverse electromagnetic (TEM) mode exists) if the normalized frequency $V$ is less than 2.405, which is given by

$$V = \frac{\pi d}{\lambda}\sqrt{n_1^2 - n_2^2} \tag{5.12}$$

where $d$ is the core diameter, $\lambda$ is the wavelength, and $n_1$ and $n_2$ are the refractive index of the core and the cladding, respectively[24]. In our case of $r = 10$, with $n_1 = 0.8$, $n_2 = 0.2$, $d = 2\alpha = 6$ μm, light with wavelength longer than 6.07 μm is guided in the TEM mode.

Although the peak THz wavelengths observed in present simulations shown in Fig. 5.13 satisfy the criteria, more comprehensive model should be developed with which we can predict the resulting THz spectrum. One interesting fact is that the resulting peak THz intensity is different from that from the uniform target as shown in Fig. 5.15.

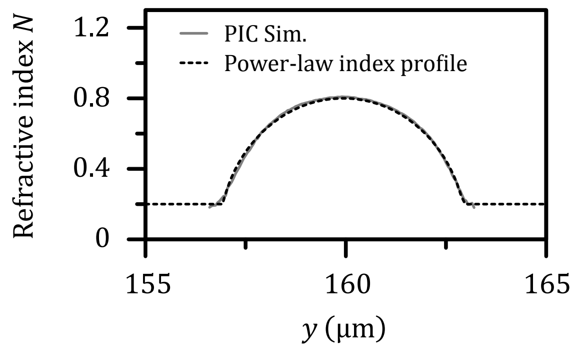


Figure 5.14: Nominal refractive index for the plasma profile shown in Fig. 5.13.

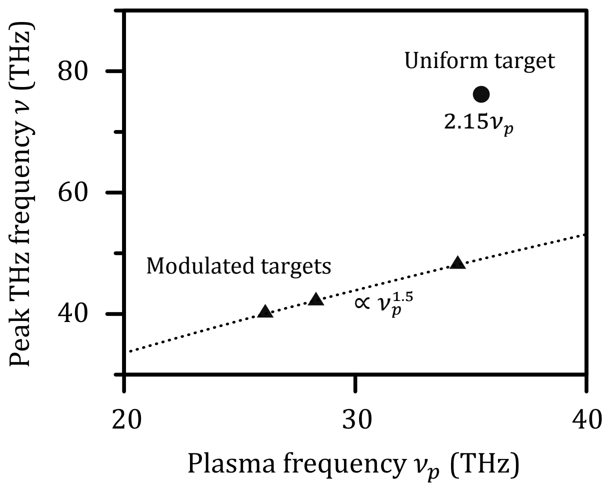


Figure 5.15: Peak THz frequency against the plasma frequency at the wall of the plasma waveguide.

## 5.7 Possibility of TW THz wave generation

We may estimate the required laser intensity to obtain the peak THz field of 0.3 GV/cm (which means 1 TW THz source) with the waveguide method. The goal field has the normalized electric field of $a_G = 5.83 \times 10^{-2}$ assuming the THz wavelength at 48 THz, which is the peak frequency in the present simulation.

The peak electric field of THz wave in present work is $a_{\mathrm{peakTHz}} = 0.12 \times 10^{-2}$ as shown in Fig. 5.6(b). The peak amplitude of the incident laser pulse of $10^{16}\,\mathrm{W/cm^2}$ is $a_{\mathrm{Laser}} = 6.83 \times 10^{-2}$. The ratio of THz field against the incident laser field is therefore 0.018.

Therefore, if we assume a linear relation, we need a laser with a peak field of 3.32 $\left(= a_G/a_{\mathrm{peakTHz}} \times a_{\mathrm{Laser}}\right)$, corresponding to a peak intensity of $2.3 \times 10^{19}\,\mathrm{W/cm^2}$ assuming the laser wavelength at 800 nm. Note that we need further research if the waveguide scheme would function as described in this work with such an relativistic laser intensity.

Still, we may prepare an array of plasma waveguide each of which generates THz wave. We then superimpose the THz light generated from each waveguide. If we stick to the laser intensity of $10^{16}\,\mathrm{W/cm^2}$, we need at least 49(= $a_G/a_{\mathrm{peakTHz}}$) waveguides. The lateral dimension of each waveguide would be about 50 µm. If we design the array so that the distance between two nearest waveguides is 1 mm, we have a two dimensional array of waveguides with 7 rows and 7 columns within a diameter of 8.5 mm (0.33”). The laser intensity to ionize those waveguides in this case is 49 times $10^{16}\,\mathrm{W/cm^2}$. Assuming a focused diameter of 20 µm and the pulse duration of 50 fs, the power of laser required is 2.5 TW. Since the waveguide diameter, i.e., modulation period, has a linear relation with the peak THz frequency, the power requirement would be proportional to the square of THz wavelength.

## 5.8 Conclusion

In conclusion, it is demonstrated that THz mode selection by plasma waveguide generated via optical field ionization of density-modulated air results in the generation of intense, coherent THz signals with quasi-monochromatic spectral distributions. A nonlinear interaction of the beat waves focused in the laser-induced plasma channel results in the formation of a strong THz radiation signal. The plasma channel serving as a waveguide forms a narrowband THz radiation with a strong gain.

Though those simulations are proof-of-principle simulations performed for relatively short-wavelength THz radiation, from the fact that a dependence of the THz radiation on the channel parameters, i.e., the contrast $A$ and period $p$, is clearly seen, we may anticipate that varying those parameters and the laser intensity may allow the tunable generation of monochromatic and coherent TW THz radiation within 1–100 THz.

## References


[1] I. Babushkin, W. Kuehn, C. Köhler, S. Skupin, L. Bergé, K. Reimann, M. Woerner, J. Herrmann, and T. Elsaesser, "Ultrafast Spatiotemporal Dynamics of Terahertz Generation by Ionizing Two-Color Femtosecond Pulses in Gases," Physical Review Letters **105**, 053903 (2010).

[2] M. Chen, A. Pukhov, X.-Y. Peng, and O. Willi, "Theoretical analysis and simulations of strong terahertz radiation from the interaction of ultrashort laser pulses with gases," Physical Review E **78**, 046406 (2008).

[3] H.-C. Wu, J. Meyer-ter Vehn, and Z.-M. Sheng, "Phase-sensitive terahertz emission from gas targets irradiated by few-cycle laser pulses," New Journal of Physics **10**, 043001 (2008).

[4] N. A. Zharova, V. A. Mironov, and D. A. Fadeev, "Anisotropic effects of terahertz emission from laser sparks in air," Physical Review E **82**, 056409 (2010).

[5] T. Bartel, P. Gaal, K. Reimann, M. Woerner, and T. Elsaesser, "Generation of single-cycle THz transients with high electric-field amplitudes." Optics Letters **30**, 2805 (2005).

[6] X. Xie, J. Dai, and X.-C. Zhang, "Coherent Control of THz Wave Generation in Ambient Air," Physical Review Letters **96**, 075005 (2006).

[7] K. Y. Kim, A. J. Taylor, J. H. Glownia, and G. Rodriguez, "Coherent control of terahertz supercontinuum generation in ultrafast laser–gas interactions," Nature Photonics **2**, 605 (2008).

[8] M. Kress, T. Löffler, S. Eden, M. Thomson, and H. G. Roskos, "Terahertz-pulse generation by photoionization of air with laser pulses composed of both fundamental and second-harmonic waves." Optics letters **29**, 1120 (2004).

[9] M. S. Sherwin, C. A. Schmuttenmaer, and P. H. Bucksbaum, eds., *Report of DOE-NSF-NIH Workshop on Opportunities in THz Science* (2004).

[10] I. Babushkin, S. Skupin, and J. Herrmann, "Generation of terahertz radiation from ionizing two-color laser pulses in Ar filled metallic hollow waveguides." Optics express **18**, 9658 (2010).

[11] D. Koyama, Y. Wada, K. Nakamura, M. Nishikawa, T. Nakagawa, and H. Kihara, "An ultrasonic air pump using an acoustic traveling wave along a small air gap." IEEE transactions on ultrasonics, ferroelectrics, and frequency control **57**, 253 (2010).

[12] A. X. Sengissen, T. J. Poinsot, J. F. Van Kampen, and J. B. Kok, "Response of a swirled non-premixed burner to fuel flow rate modulation," in *Complex Effects in Large Eddy Simulations* (Springer, 2007) pp. 337–351.

[13] C. Durfee and H. Milchberg, "Light pipe for high intensity laser pulses," Physical Review Letters **71**, 2409 (1993).

[14] T. Clark and H. Milchberg, "Time- and Space-Resolved Density Evolution of the Plasma Waveguide," Physical Review Letters **78**, 2373 (1997).

[15] T. Clark and H. Milchberg, "Optical mode structure of the plasma waveguide," Physical Review E **61**, 1954 (2000).

[16] Y. Mizuta, T. Hosokai, S. Masuda, A. Zhidkov, K. Makito, N. Nakanii, S. Kajino, A. Nishida, M. Kando, M. Mori, H. Kotaki, Y. Hayashi, S. V. Bulanov, and R. Kodama, "Splash plasma channels produced by picosecond laser pulses in argon gas for laser wakefield acceleration," Physical Review Special Topics - Accelerators and Beams **15**, 121301 (2012).

[17] D. Kaganovich, A. Ting, D. F. Gordon, R. F. Hubbard, T. G. Jones, A. Zigler, and P. Sprangle, "First demonstration of a staged all-optical laser wakefield acceleration," Physics of Plasmas **12**, 100702 (2005).

[18] T. Hosokai, K. Kinoshita, T. Ohkubo, A. Maekawa, M. Uesaka, A. Zhidkov, A. Yamazaki, H. Kotaki, M. Kando, K. Nakajima, S. Bulanov, P. Tomassini, A. Giulietti, and D. Giulietti, "Observation of strong correlation between quasimonoenergetic electron beam generation by laser wakefield and laser guiding inside a preplasma cavity," Physical Review E **73**, 036407 (2006).

[19] J. D. Anderson, "Modern Compressible Flow: With Historical Perspective," (McGraw Hill, New York, 1989) 3rd ed., Chap. 5, pp. 147–183.

[20] A. Zhidkov, J. Koga, T. Esirkepov, T. Hosokai, M. Uesaka, and T. Tajima, "Optical-field-ionization effects on the propagation of an ultraintense laser pulse in high- Z gas jets," Physical Review E **69**, 066408 (2004).

[21] J. Shin, A. Zhidkov, Z. Jin, T. Hosokai, and R. Kodama, "Non-linear plasma effects on laser-induced terahertz emission from the atmosphere," Physics of Plasmas **19**, 023117 (2012).

[22] E. Esarey, P. Sprangle, J. Krall, and A. Ting, "Self-focusing and guiding of short laser pulses in ionizing gases and plasmas," IEEE Journal of Quantum Electronics **33**, 1879 (1997).

[23] B. E. A. Saleh and M. C. Teich, *Fundamentals of Photonics*, 2nd ed. (Wiley-Interscience, 2007).

[24] H. Dutton, *Understanding Optical Communications* (IBM Redbooks, 1998).

# Chapter 6

# Conclusion and Prospects

This dissertation described the models, simulations, and experimental results regarding the generation of intense THz wave using the laser-plasma interaction. In addition to clarifying the radiation mechanism of THz wave from plasma (Chp. 2 and Chp. 3) at high laser intensity that has not been studied to date, the goal of intense THz wave source is pursued in two different ways, namely, amplification (Chp. 4) and waveguiding (Chp. 5). Both the amplification and waveguiding scheme need further experimental studies to confirm the validity of the claims and to realize the TW THz radiation source. I hope this dissertation can sereve as a reference point for the on-going efforts toward the TW THz electromagnetic source. Major achievements and suggestions for future works can be summarized as following:

In Chp. 2, theories for several THz generation mechanism using laser plasma interaction were introduced or developed. Notably, phase matching condition for four-wave mixing assuming finite $k$-vector of THz wave (Sec. 2.2) are newly developed, although it is desirable that it be verified by experiments or simulations. The beat-wave model for THz generation is developed for the laser intensity around $10^{16}\,\mathrm{W/cm^2}$ for the first time. It takes into account the generation of steep plasma density ramp by laser pulse and the frequency upshift of the incident laser, which has been ignored in the photocurrent model.

In Chp. 3, the THz generation process at laser intensity as high as $10^{16}\,\mathrm{W/cm^2}$ has been studied using multidimensional particle-in-cell simulations including optical field ionization. Surprisingly, precedent particle-in-cell simulations were performed for only lower laser intensities around $10^{14}\,\mathrm{W/cm^2}$. Regarding the scaling of THz power, we found that up to the laser intensity $I \sim 10^{15}\,\mathrm{W/cm^2}$, the power growth is faster than linear, while beyond that intensity, the growth is slower than linear (Sec. 3.3.3). Also, because the PIC simulation has two-dimensional spatial space, we could see that higher laser intensity results in denser plasma, and more diffraction effect on THz wave, resulting in larger divergent radiation angle, as is described in the conclusion (Sec. 3.4).

In Chp. 4, the possibility of THz amplification has been suggested by comparing experimental results with a one-dimensional model with and without accounting for amplification of THz wave. Plasma density measurement method described in Sec. 4.4.1 allowed the measurement of electric density around $(1\text{–}100)\times10^{16}\,\mathrm{cm}^{-3}$, which I believe the first measurement of its kind in the literature of THz source using laser-plasma interaction. This informative measurement method helped attribute such an enhancement to the formation of an asymmetric plasma profile in which the plasma density increases steeply in the head and decreases gradually in the tail.

The measurement can still be improved in two ways, namely, time-resolved plasma density measurement and temporal THz pulse diagnostics, to resolve the time evolution of the plasma filaments and the generated THz radiation as the plasma filament is being generated.

In Chp. 5, a novel scheme of narrowband intense THz wave source using plasma waveguide is demonstrated in a proof-of-principle manner with a set of PIC simulations. In a plasma waveguide, the mixing of waves involved in the beat-wave generation may last longer, leading to a higher laser-to-THz conversion efficiency. Optimal set of the initial modulation parameters, i.e., the contrast $r$ and period $p$ is found by simulation that yields THz field amplitude stronger by about two order compared to uniform gas target. The energy of the long wavelength quasi-monochromatic radiation is approximately 0.1 percent of the laser pulse energy. As described in the conclusion (Sec. 5.8), the new method may reduce the requirement on the laser power to realize one TW THz source by one order, i.e., to 10 TW.

The tunability of the scheme depending linearly on the modulation period $p$ is also demonstrated. I anticipate that further research varying those parameters and the laser intensity may allow the tunable generation of monochromatic and coherent THz radiation within 1–100 THz.

In conclusion, the research results in this dissertation, i.e., development of THz generation theory applicable at high laser intensity, experimental indication of THz amplification, and demonstration of plasma waveguide by particle-in-cell code, would open a new possibility for the development of TW THz electromagnetic source using laser-plasma interaction, expediting advancements in research and application of HEDP.

# Appendix A

# Single-shot Temporal Profile Diagnostics of Terahertz Wave

## A.1 Introduction

Measurement of THz time profile is important for evaluation of the characteristics of the generated THz wave and its applications. Since THz wave has a rather long pulse duration (typically around several picoseconds) with a long wavelength (1 THz corresponds to 300 μm), the electric field, not just electric intensity can be measured by Terahertz time-domain spectroscopy (TTDS) technique. Traditional TTDS uses a multi-shot scanning method to obtain the temporal waveform of THz wave, which limits its applications in high power laser systems and THz source experiments due to the low repetition rates and/or shot-to-shot fluctuations.

Therefore, single-shot TTDS is of interests to many researches such as intense THz generations, ultrafast relativistic electron beam diagnostics, etc[1–3]. Most of the schemes for single-shot detection of THz fields exploit the spectral encoding with a chirped probe pulse, which requires a rather stable output spectrum of the probe laser. For those widely used short pulse chirped pulse amplification (CPA) laser systems, spectral shaping methods, like a birefringent filter or an acousto-optic programmable gain control filter, is often used to obtain a broadband spectrum so that the pulse can be compressed to tens of femtosecond duration, close to the limit of Fourier transform. These spectral shaping components meanwhile increase the instability of laser spectrum, making the spectral encoding TTDS more difficult. In such a case, a direct spatial encoding single-shot TTDS scheme using an echelon pair[4] is a more practical choice because the spatial beam profile tends to be more stable than the spectrum.

Here, important aspects of the electro-optical (EO) modulation method is summarized and the specific setup used for the measurement of THz time profile is described in detail.

## A.2 Electro-optical modulation

EO modulation method utilizes the Pockels effect in EO crystals. Electric field of THz wave induces birefringence in the crystal and the polarization of the probe beam that are time-synchronized with the THz wave is rotated according to the THz field amplitude ($E_{\mathrm{THz}}$), not intensity ($I_{\mathrm{THz}}$).

The suitable orientation of the <110>-cut ZnTe for THz wave detection is theoretically derived in ref. 5. Instead of repeating the work, important points for experiment is recapitulated here.

Figure A.1 shows the laboratory coordinate. Note that the plane of paper coincides with the <110> plane on which the THz beam and the probe beam normally incident. Both beams are assumed linearly polarized along the plane. The angle between the $z$ axis and the THz electric field is $\theta$ and the angle between the major ellipse axis $y''$ and the $y'$ axis is $\varphi$.

In ref. 5, it is found that the refractive index of the crystal for the light linearly polarzed along the $y''$ and $z''$ axes are, respectively,

$$n_{y''} = n_0 + \frac{n_0^3 r_{41} E_{\mathrm{THz}}}{4}\left(\cos\theta - \sqrt{1+3\sin^2\theta}\right) \tag{A.1}$$

$$n_{z''} = n_0 + \frac{n_0^3 r_{41} E_{\mathrm{THz}}}{4}\left(\cos\theta + \sqrt{1+3\sin^2\theta}\right), \tag{A.2}$$

and the different in the refractive index is

$$\Delta n = \left(n_{z''} - n_{y''}\right) = \frac{n_0^3 r_{41} E_{\mathrm{THz}}\sqrt{1+3\sin^2\theta}}{2}. \tag{A.3}$$

The phase retardation $\Gamma = (2\pi d/\lambda)\,\Delta n$ is proportional to the detection signal amplitude and it is maximum when the angle $\theta$ between the THz field and the $z$ axis is $\pm 90°$, i.e., parallel to the $y''$ axis (<$\pm 1, \mp 1, 0$>) direction of the crystal.

The ellipse orientation is decided by

$$2\tan\theta = -\tan 2\varphi \tag{A.4}$$

It implies that for the maximum phase retardation with $\theta = \pm 90°$, the angle $\varphi$ is $\pm 45°$, which means the polarization of the probe beam should be

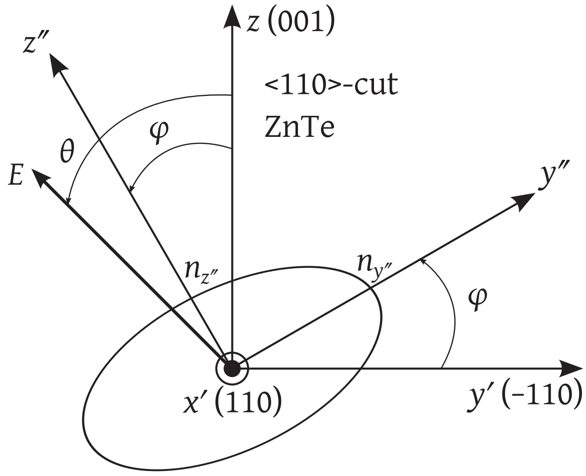


Figure A.1: The laboratory frame and the principal-axes frame

either paralle to $y'$ or $z$ axis for optimal THz detection by EO sampling.

## A.3 Design of the echelon pair

The two reflective echelons made of aluminum with a minimum surface flatness at $\lambda/5$ for 800 nm wavelength is manufactured by *Nidec Sankyo corporation, Nagano, Japan*. The reflective surfaces have 20 steps. The height of each step is 400 μm for echelon 1, and 20 μm for echelon 2. As shown in Fig. A. 2, 400 ($20 \times 20$) beamlets can be produced with a total beam dimension of 20 mm × 20 mm. The time interval between two beamlets is $\sim$ 94.3 fs and the total time window stretches to $\sim$ 37.7 ps.

## A.4 Experimental demonstration

A preliminary experiment was performed at the P-cube laser system of the Graduate School of Engineering, Osaka University. The experimental setup is shown in Fig. A.3. A 10 mJ, 800 nm, 60 fs laser beam is set up as a typical pump-probe electro-optic (EO) sampling system. The pump beam is focused into ambient air by a lens with the focal length of 200 mm. A type-I $\beta$-$BaB_2O_4$ (BBO) crystal is placed after the focal lens to generate a second harmonic ($2\omega$) laser pulse from the incident fundamental one ($\omega$). A polymer filter is used to transmit THz wave from the two-color laser generated plasma channel. THz wave is collected by an off-axis parabola (OAP), while blocking the residual $\omega$ and $2\omega$ pulses.

The probe arm after passing the reflective echelon pair is sent through a half-wave plate and a polarizer to change the beam polarization parallel to the THz wave. The beam is then collinearly focused onto a 1mm thick <110> ZnTe crystal with the synchronized THz pulse. The THz electric field is encoded to the different position of the beamlets, which is detected by a 16-bit CCD camera after passing another polarizer with a cross polarization. The two lenses (lens 1 and lens 2) are set as an image-relay to reproduce the image of the echelon pair to the camera while keeping the collinear focus with the OAP on the ZnTe.

A typical CCD image of the beamlets is shown in Fig. A.4(a). Note that the shape of the beamlets is square when imaged properly, which is difficult to be separated from each other for data acquisition. By shiftting the CCD slightly off the image plane of the image relay, the beamlets' shape becomes circular with a clearer boundary between each other. The relative intensity of each signal remains similar to the square case.

Figure A.4(b) shows a typical signal image after subtracting the image taken without THz wave from the one with the THz wave. The intensity modulation by the THz field is clearly seen. The intensities for each beamlet are integrated and read out column-by-column in the order of time sequence. The single-shot THz waveform is then obtained with a best signal-to-noise ratio of about 16, as shown in Fig. A.5. The measured waveform shifts as we adjust the delay between the pump and probe beams, which agrees well with the designed time interval.

Figure A.6 shows the corresponding THz spectrum obtained by the Fourier transform of the temporal waveform. Multiple absorption peaks that agree well to those attributed to the water vapor in the ambient air[6] are observed as marked by number. The descriptions for each numbered peaks between 0.2 THz to 2.4 THz are given in Table A.1.

Table A.1: Rotational transitions in water vapor from 0.2 to 2.4 THz (excerpted from ref. 7)

| Number | Frequency (THz) | Low state | High Stage | Type of transition |
|---|---|---|---|---|
| 1 | 0.557 | 101 | 110 | Ortho |
| 2 | 0.753 | 202 | 211 | Para |
| 3 | 1.098 | 303 | 312 | Ortho |
| 4 | 1.164 | 312 | 321 | Ortho |
| 5 | 1.226 | 211 | 220 | Para |
| 6 | 1.412 | 514 | 523 | Ortho |
| 7 | 1.671 | 101 | 212 | Ortho |
| 8 | 1.718 | 212 | 303 | Ortho |
| 9 | 1.798 | 725 | 734 | Ortho |
| 10 | 1.869 | 523 | 532 | Ortho |
| 11 | 2.076 | 322 | 412 | Para |
| 12 | 2.264 | 414 | 423 | Ortho |
| 13 | 2.346 | 716 | 725 | Ortho |

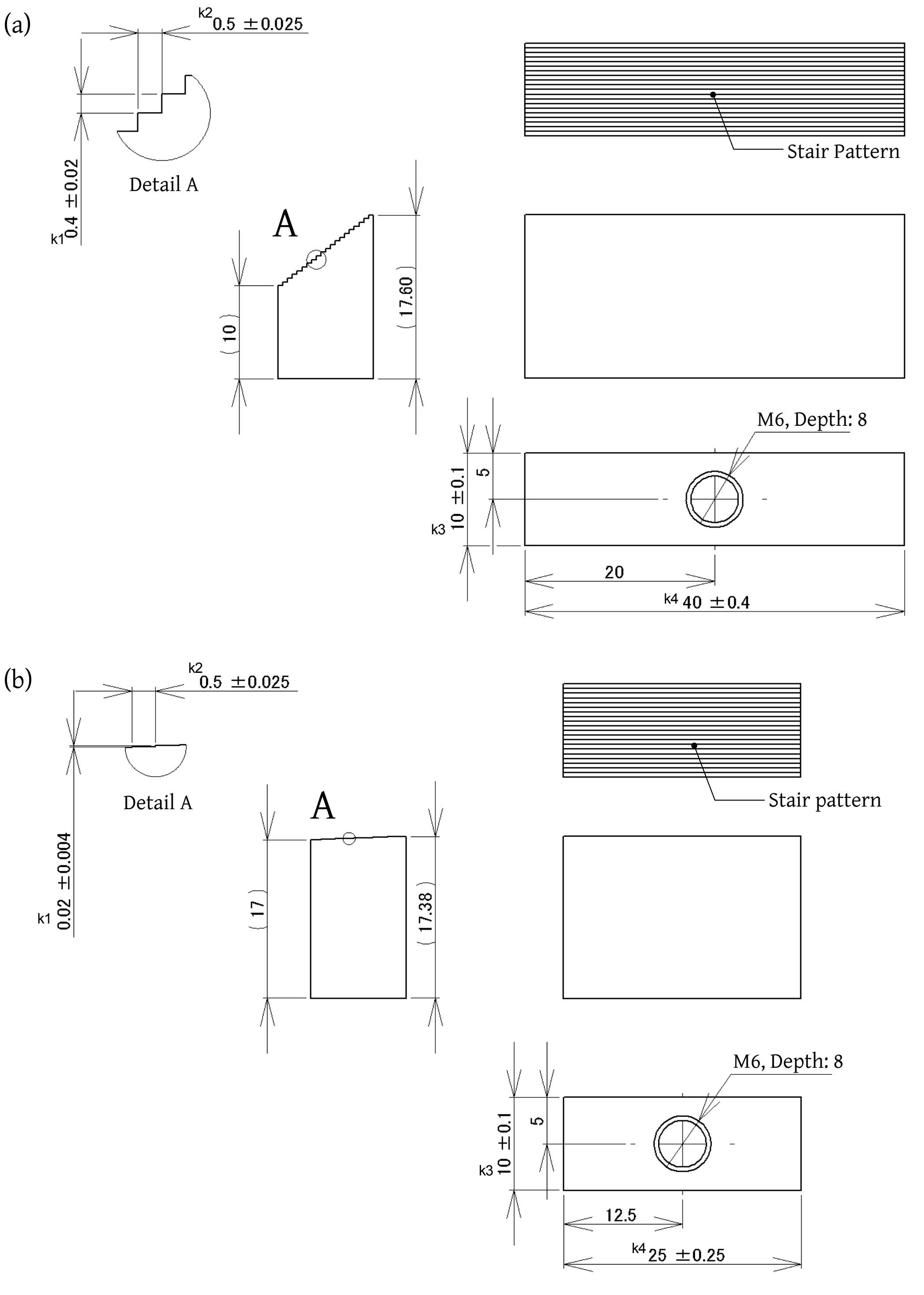


Figure A.2: Design of the echelon pair. (a) Echelon 1, (b) Echelon 2. CAD work done by Akio Okumoto at *Nidec Sankyo corporation*.

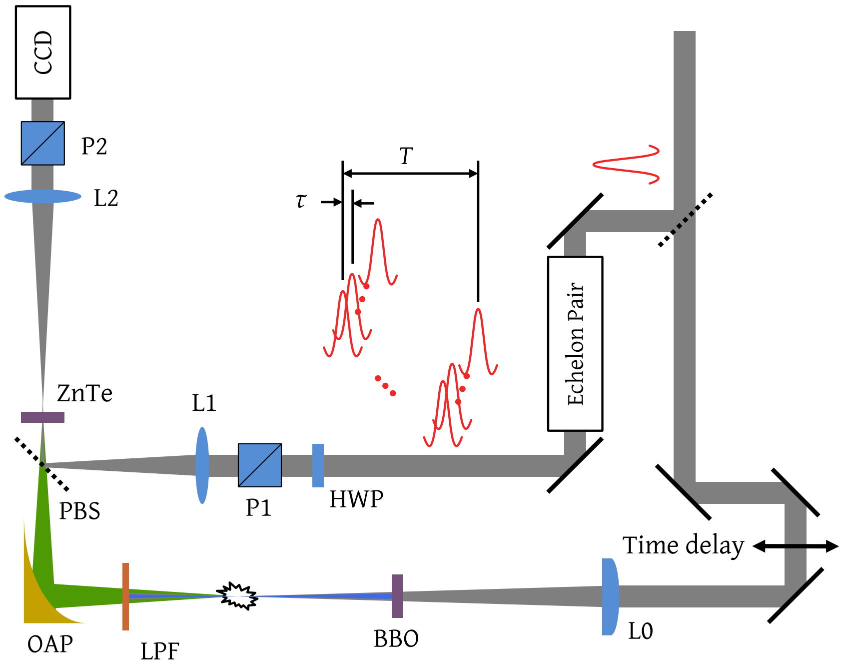


Figure A.3: Experimental setup for single-shot TTDS of two-color laser generated THz wave in the air.

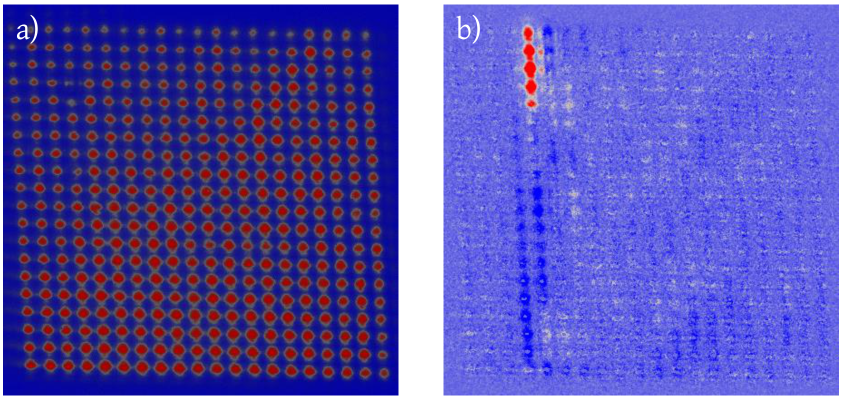


Figure A.4: (a) Typical beamlets image without the cross polarizer P2. (b) Beamlets image obtained by comparing the difference of with and without the presence of THz field.

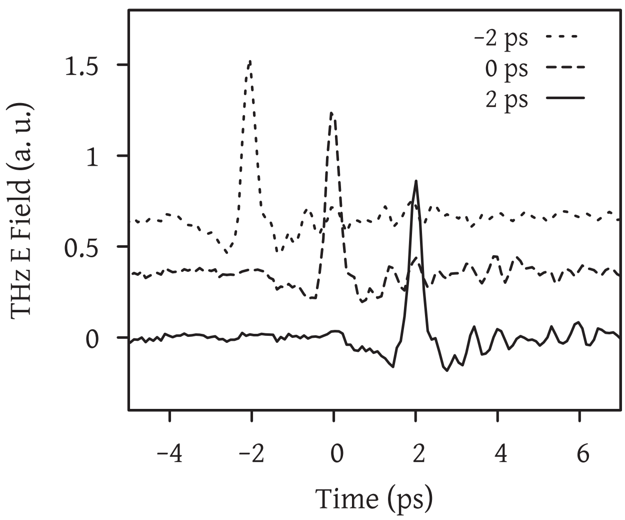


Figure A.5: THz time profile taken with different probe beam delay relative to the THz wave.

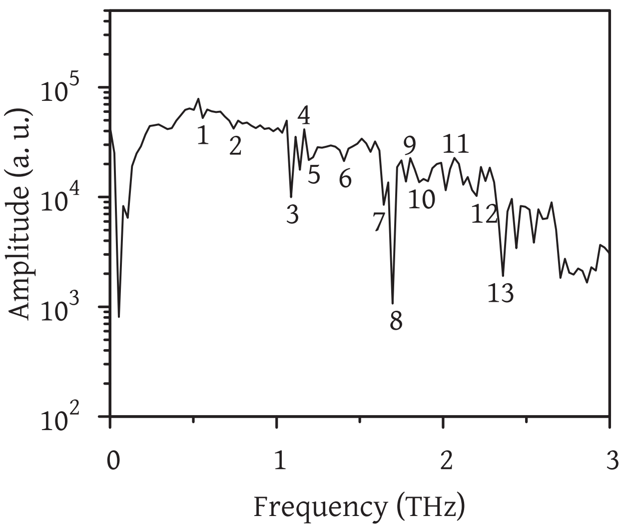


Figure A.6: The spectrum of the THz profile shown in Fig. A.4. The numbered peaks give the absorption lines from the water vapor in the air.

# References

[1] I. Wilke, a. MacLeod, W. Gillespie, G. Berden, G. Knippels, and a. van der Meer, "Single-Shot Electron-Beam Bunch Length Measurements," Physical Review Letters **88**, 124801 (2002).

[2] G. Berden, S. Jamison, A. MacLeod, W. Gillespie, B. Redlich, and A. van der Meer, "Electro-Optic Technique with Improved Time Resolution for Real-Time, Nondestructive, Single-Shot Measurements of Femtosecond Electron Bunch Profiles," Physical Review Letters **93**, 114802 (2004).

[3] J. van Tilborg, C. B. Schroeder, C. Tóth, C. G. R. Geddes, E. Esarey, and W. P. Leemans, "Single-shot spatiotemporal measurements of high-field terahertz pulses." Optics Letters **32**, 313 (2007).

[4] K.-Y. Kim, J. H. Glownia, A. J. Taylor, and G. Rodriguez, "Terahertz emission from ultrafast ionizing air in symmetry-broken laser fields." Optics Express **15**, 4577 (2007).

[5] Q. Chen, M. Tani, Z. Jiang, and X.-C. Zhang, "Electro-optic transceivers for terahertz-wave applications," Journal of the Optical Society of America B **18**, 823 (2001).

[6] X. Xin, H. Altan, a. Saint, D. Matten, and R. R. Alfano, "Terahertz absorption spectrum of para and ortho water vapors at different humidities at room temperature," Journal of Applied Physics **100**, 094905 (2006).

[7] J.-M. Flaud, C. Camy-Peyret, and R. A. Toth, *International Tables of Selected Constants* (Pergamon, Oxford, 1987).

# Appendix B

# Probe-Beam-Free Detection of Terahertz Detection Method*

## B.1 Introduction

Advancement of the measurement method for temporal profile of terahertz (THz) wave[1,2] is one of the reasons that have heightened the interest in THz technology from a broad range of engineering and research areas for security, biomedical imaging, material physics and etc[3,4]. Those *coherent* methods, electro-optical sampling or photoconductive switching, measure coherent portion of THz radiation, providing phase information of THz waves. However, they are difficult to setup, because they require a femtosecond probe beam and we need to align both the probe beam and the THz wave precisely so that they are synchronized and spatially overlapped at the detecting component. On the contrary, incoherent detectors, such as bolometer and Golay cell, do not require a probe beam, but provide only THz power from all heat (incoherent) sources in addition to the coherent sources. For that reason, the incoherent detectors have lower signal-to-noise. Still, they are convenient to use.

With recent research efforts pursuing strong THz radiation sources, MW THz pulse with an electric field higher than 100 kV/cm can be obtained with a table-top fs laser system by several methods such as two-color laser scheme[5] and tilted-pulse-front scheme[6]. Such a strong THz field can directly drive the electrons in various materials such as nitrogen gas plasma[7] and quantum well semiconductor[8], and the effects have been observed through luminescence

*At the time of writing, March 2014, this work has been submitted to and is under review as "Probe beam-free detection of terahertz wave by electroluminescence induced by intense THz pulse," by *J. Shin*, Z. Jin, Y. Nosaka, T. Nakazawa, and R. Kodama, Journal of Physics: Conference Series.

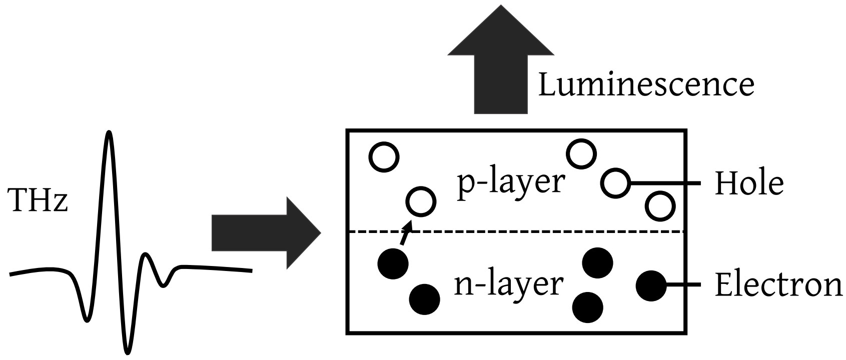


Figure B.1: Electroluminescence driven by THz field.

phenomena.

In this chapter, a direct THz electric field detection method by measuring the electroluminescence (EL) induced by intense THz pulse inside common light emitting diode (LED), as illustrated in the Fig. B.1, is demonstrated. The scheme has the advantage of both the coherent and incoherent method; it can be classified under coherent method, but does not require a probe beam to operate. Because it makes use of the conventional LED technology, it may be useful for realizing a low-cost, probe-beam-free THz detection and imaging system.

## B.2 Response of LED to nanosecond pulses

The response of commercially available LEDs for electric signals shorter than $\sim$ ns are not well investigated. Since the THz pulse from two-color scheme usually has a single-cycle waveform with a duration of ps level, it is necessary to investigate the LED's response to a short voltage pulse. A digital pulse generator *DG535* (*Stanford Research Systems, Inc.*) is used to apply drive pulses with various time durations from $\mu$s to 5 ns to the LED chip. The emission of the LED is collected and measured by a 16 bit CCD camera. Figure B.2 shows the response of the LED. If the pulse duration is longer than 200 ns the response is linear regardless of the support bias. With shorter drive pulses, the emission intensity drops non-linearly and reaches to the noise level as the pulse duration becomes shorter than 25 ns which is comparable to the typical rise and fall time (15 ns) of this LED.

The pulse duration limit, however, can be overcome by applying a supporting DC bias, as indicated in the inset of Fig. B.2. The effect of the pulse voltage is investigated by comparing the difference between the emission intensity with and without the drive pulse. The pulse response gets more close to linear

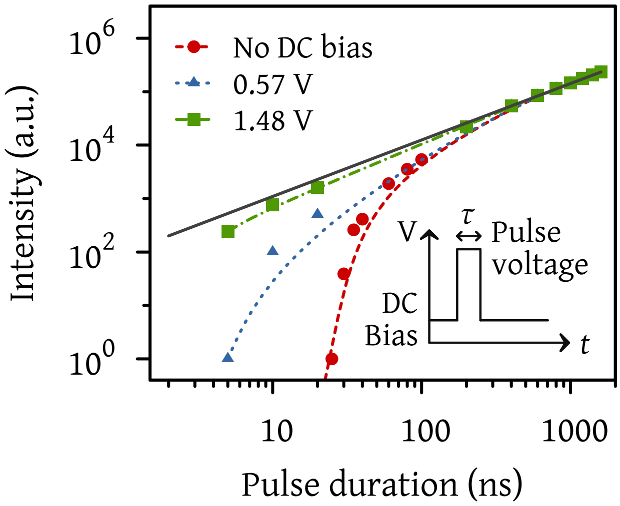


Figure B.2: Pulse response of the LED. The black solid line shows a linear relation between the emission intensity and pulse duration. The red circles, blue triangles, and green squares show the measured results with an supporting DC bias of 0 V, 0.57 V and 1.48 V, respectively.

decrease (black solid line) with the support of the bias.

It is noted that 5 ns, which is the limit of our pulse generator, is still much longer than the THz pulse duration. However, this measurement suggests that the EL induced by short THz pulses can be detected with a sufficient supporting bias.

## B.3 Experiments

Figure B.3 shows the setup of experiments performed using the P-cube laser facility at the Graduate School of Engineering, Osaka University. It was adjusted to deliver 30 mJ of energy in ~100 fs long pulse with its spectrum centered on 800 nm. It was negatively chirped for optimal generation of THz wave. The laser was focused into ambient air by an $f/20$ lens. A 100-$\mu$m thick $\beta$-barium borate (BBO) crystal behind the focal lens generated the second harmonic ($2\omega$) pulse by the type-I second harmonic generation from the fundamental laser pulse ($\omega$). A polymer filter was put to allow transmit only the THz wave generated from the plasma channel, while blocking the residual $\omega$ and $2\omega$ pulses. The THz pulse was then focused by an off-axis parabola (OAP) onto the LED chip at an incident angle of 45 degree. A GaAlAs LED manufactured by *Toshiba* (Model No. *TLN1108*) was used in our experiments, which emits

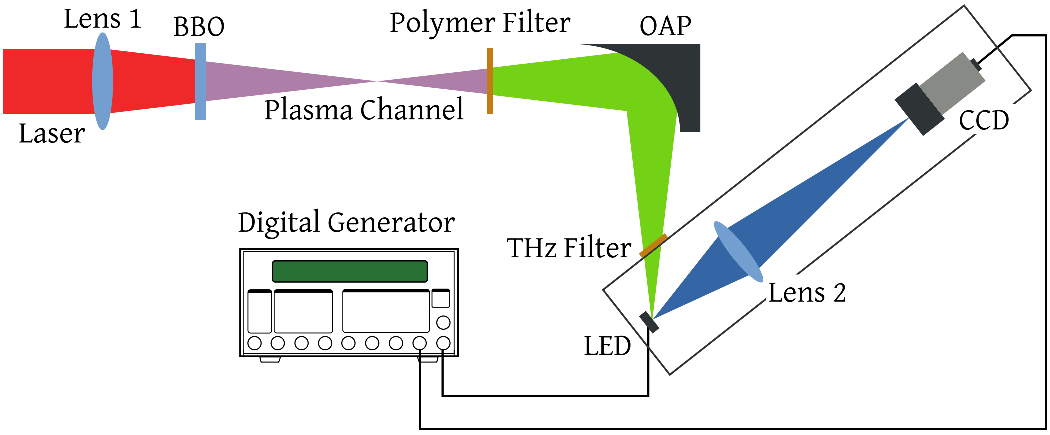


Figure B.3: Experimental setup for probe-beam free THz detection

near-infrared light with its central wavelength at 870 nm. The emitted luminescence is collected to a gated intensified CCD camera. To reduce the noise, the CCD gate was opened 5 ns before the arrival of the THz wave and closed after 50 ns. The entire LED emission measurement system is carefully enclosed and sealed in a black box with a long-pass THz filter window to ensure that no scattering light from the laser and plasma channel can arrive at the camera. The function generator *DG535* provided the supporting DC bias for the LED and the synchronized trigger signal for the CCD gate.

The generated THz wave has a single-cycle profile with a period of 1 ps, as shown in Fig. A.5 on page 102, which is measured by a single-shot THz time-domain spectroscopy using a pair of reflective echelon[9]. The maximum THz energy of about 5 μJ was measured with our calibrated Golay Cell, corresponding to an electric field of ~ 0.77 MV/cm at the focal spot.

Figure B.4 shows the typical LED emission enhancement patterns with different supporting DC bias voltages of 3.78 V, 5.61 V and 5.81 V, with insets showing the CCD images of the LED chip after subtracting the image without incident THz pulse as the background. When the bias is lower than 3.78 V, the EL induced by THz field is too weak so that the counts on CCD are close to the noise level.

Figure B.5 shows that different peak amplitude of the incident THz pulse changes the amount of EL enhancement proportionally. It is also clear that the EL enhancement becomes larger with higher bias voltages, which is consistent with the measurements using ns pulses as shown in Sec. B.2.

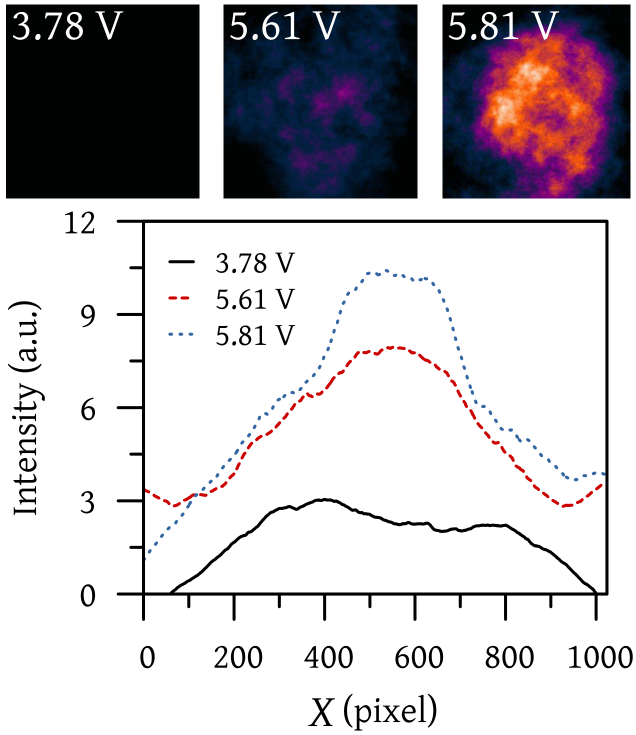


Figure B.4: Intensity profiles of the EL induced by 0.77 MV/cm THz pulses accompanied by supporting DC biases. The upper insets show the CCD images of the enhanced emission pattern from LED chip.

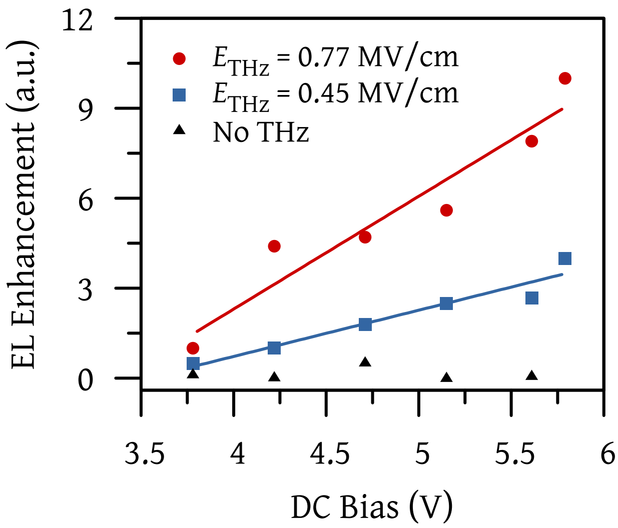


Figure B.5: Enhancement of EL against the given external DC bias.

## B.4 Conclusion

It is demonstrated that a direct THz electric field detection is possible by measuring the EL induced by THz pulses inside commercially available LED. This method is coherent with its signal sensitive to the electric field of the THz wave, but has an advantage over other coherent methods that it does not require a probe beam. Because the results rely upon the well-established LED technology, it may be useful for realizing a low-cost, probe-beam-free THz imaging system.

## References

[1] X.-C. Zhang, Y. Jin, and X. F. Ma, "Coherent measurement of THz optical rectification from electro-optic crystals," Applied Physics Letters **61**, 2764 (1992).

[2] D. H. Auston, K. P. Cheung, and P. R. Smith, "Picosecond photoconducting Hertzian dipoles," Applied Physics Letters **45**, 284 (1984).

[3] M. Tonouchi, "Cutting-edge terahertz technology," Nature Photonics **1**, 97 (2007).

[4] B. Ferguson and X.-C. Zhang, "Materials for terahertz science and technology." Nature materials **1**, 26 (2002).

[5] K. Y. Kim, A. J. Taylor, J. H. Glownia, and G. Rodriguez, "Coherent control of terahertz supercontinuum generation in ultrafast laser–gas interactions," Nature Photonics **2**, 605 (2008).

[6] J. Hebling, K.-L. Yeh, M. C. Hoffmann, B. Bartal, and K. A. Nelson, "Generation of high-power terahertz pulses by tilted-pulse-front excitation and their application possibilities," Journal of the Optical Society of America B **25**, B6 (2008).

[7] J. Liu, J. Dai, S. L. Chin, and X.-C. Zhang, "Broadband terahertz wave remote sensing using coherent manipulation of fluorescence from asymmetrically ionized gases," Nature Photonics **4**, 627 (2010).

[8] H. Hirori, K. Shinokita, M. Shirai, S. Tani, Y. Kadoya, and K. Tanaka, "Extraordinary carrier multiplication gated by a picosecond electric field pulse." Nature communications **2**, 594 (2011).

[9] K. Y. Kim, B. Yellampalle, A. J. Taylor, G. Rodriguez, and J. H. Glownia, "Single-shot terahertz pulse characterization via two-dimensional electro-optic imaging with dual echelons." Optics letters **32**, 1968 (2007).

# Publications and Presentations

## List of Journals (peer reviewed)

1. J. Shin, A. Zhidkov, Z. Jin, T. Hosokai, and R. Kodama, “Non-linear plasma effects on laser-induced terahertz emission from the atmosphere,” Physics of Plasmas **19**, 023117 (February 2012).

2. J. Shin, Z. Jin, T. Hosokai, and R. Kodama, “Exponential enhancement of terahertz power from asymmetric plasma profile pumped by two-color laser femtosecond pulses,” JPS Conference Proceedings **1**, 015091 (March 2014).

3. J. Shin, A. Zhidkov, Z. Jin, T. Hosokai, and R. Kodama, “Mode-selective terahertz emission from rippled air irradiated by femtosecond laser pulses,” Applied Physics Express **7**, 046202 (March 2014).

## List of international poster presentations

1. J. Shin, A. Zhidkov, Z. Jin, T. Hosokai, R. Kodama, “Tunable Quasi-monochromatic Terahertz Radiation from Rippled Air Irradiated by Femtosecond Laser Pulses”, International Conference on HIGH ENERGY DENSITY SCIENCES 2014 (HEDS2014) (April 2014)

2. J. Shin, A. Zhidkov, Z. Jin, T. Hosokai, R. Kodama, “Quasi-monochromatic terahertz emission from rippled air irradiated by femtosecond laser pulses”, HEDS in Asia 2014 (January 2014)

3. J. Shin, Z. Jin, T. Hosokai, R. Kodama, “Terahertz radiation enhancement correlated with asymmetric plasma filament generated by femtosecond laser pulses,” International Conference on HIGH ENERGY DENSITY SCIENCES 2013 (HEDS2013) (April 2013)

4. J. Shin, Z. Jin, T. Hosokai, R. Kodama, "Exponential enhancement of terahertz emission by increasing length of plasma filament pumped by femtosecond laser pulses," The International Conference on Infrared, Millimeter, and Terahertz Waves 2012 (IRMMW-THz 2012) (September 2012)

5. J. Shin, Zhidkov, A., Z. Jin, T. Hosokai, and R. Kodama, "Power scaling of THz radiation from air plasma generated by two-color laser," International Conference on HIGH ENERGY DENSITY SCIENCES 2012 (HEDS2012) (April 2012)

6. J. Shin, Zhidkov, A., Z. Jin, T. Hosokai, and R. Kodama, "Dependency of Power of THz Radiation from Air Plasma Generated by Two-color," International Symposium on Terahertz Nanoscience (TeraNano2011) (November 2011)

7. J. Shin, Zhidkov, A., Z. Jin, T. Hosokai, and R. Kodama, "Characteristics of THz radiation from air plasma generated by two-color laser," Plasma Conference 2011 (PLASMA2011) (November 2011)

8. J. Shin, Z. Jin, T. Hosokai, R. Kodama, "Dependence of terahertz radiation from plasma on the coupling of multi-filaments generated by two-color laser pulses," 12th Symposium on Advanced Photon Research (May 2011)